Integration of Parent-Child Unmanned Air Vehicle Focusing on Control System Development

by

Sanghyuk Park

Submitted to the Department of Aeronautics and Astronautics
in partial fulfillment of the requirements for the degree of

Master of Science in Aeronautics and Astronautics

at the

MASSACHUSETTS INSTITUTE OF TECHNOLOGY

February 2001

Author ....
Department of Aeronautics and Astronautics
January 28, 2001

Certified by ....
John J. Deyst
Professor of Aeronautics and Astronautics
Thesis Supervisor

Certified by ....
James D. Paduano
Principal Research Engineer of Aeronautics and Astronautics
Thesis Supervisor

Accepted by ....
Wallace E. Vander Velde
Chairman, Committee on Graduate Students

Integration of Parent-Child Unmanned Air Vehicle Focusing on Control System Development

by

Sanghyuk Park

Submitted to the Department of Aeronautics and Astronautics
on January 28, 2001, in partial fulfillment of the
requirements for the degree of
Master of Science in Aeronautics and Astronautics

Abstract

As a part of PCUAV(Parent Child Unmanned Air Vehicle) project, the author participared in three areas. First, a study on the vehicle integration concept between a larger and two smaller UAVs are described. Various integration concepts were considered and compared from the point of view of performance and stability. The reintegration between the larger and the smaller UAVs are tried in the project. The procedure of the modeling, controller design and simulation for the reintegration is described next. A vision based positioning was developed for the three-axis position sensor for the reintegration. The procedure and the lessons learned during this development are also presented.

Thesis Supervisor: John J. Deyst
Title: Professor of Aeronautics and Astronautics

Thesis Supervisor: James D. Paduano
Title: Principal Research Engineer of Aeronautics and Astronautics

Acknowledgments

The work described in this thesis is a result of a team work. Here I would like to thank people who have worked with me in the project and, otherwise have supported me in my two years in MIT.

I would like to thank my advisor Professor John J. Deyst for his cordial concern and constant motivation and for giving me the opportunity to work on this exciting team project.

To Professor James Paduano, I express my gratitude for your priceless, constant advice and guidance.

To Professor Charles W. Boppe and Mark Drela, I appreciate your insights and supports throughout the project especially when we were designing our airplanes.

I am grateful to the Charles Starks Draper Laboratory and its engineers, especially Dr. Brent Appleby and Mr Richard Martorana, for their support and interest in the project.

I would like to thank the students who have been in the project. Anand Karasi, Alankar Chhabra and Tarek Nochahrli who were in the first year of the project, helped me in getting accustomed to the team project. I appreciate the friendship from Alexander Omelchenko who has been with me for the two years in the project. I would like to thank Alexis Stanke for her cordial concern. I would like to thank Raffi Babikian for his exceptional freindship. Simon Evans and Antony Evans, I miss the days when I was working with you. I would like to thank Thomas Jones for sharing ideas and having lots of fun. I would like to thank Damien Jourdan, Sarah Saleh, Carmen Carreras, Richard Poutrel, Jason Kepler, and Scott Kimbrel. They joined in the third year of the project, and we had lots of fun together. Finally, I would like to thank Francois Urbain who has been working closely with me in the project. Without these friends, I would never been able to enjoy working in the project.

Jinwook Lee, Junmo Kim, Seonah Lee, and Taehong Park were also very supportive friends during my two years in MIT.

Last but not least, my special thanks to my family back in Korea for their constant

concern and support.

Contents

List of Figures

List of Tables

Chapter 1

Introduction

1.1 Background and Motivations

Recently, the usefulness of micro-air vehicles (MAVs) has been realized and many organizations are working on the development of these small palm-sized vehicles. Small aerial vehicles have many attractive features - close surveillance capability and low detectability, for example. But they also have very limited time aloft and short range. These limitations can be mitigated by combining them with a larger unmanned aerial vehicle (UAV), if this larger vehicle plays the role of a carrier and at the same time coordinates the smaller vehicle's operations.

A team was assembled at MIT based on the need for such a system, and a two-year-project, funded by the Charles Draper Laboratory, was initiated in September, 1998. The Draper Laboratory has expertise in the areas of guidance, navigation and control systems, and the current sponsored work is organized around the following program areas: Navy Strategic Programs, Space and Missiles, Ocean Systems and Special Operations, Tactical Systems, and Applied Information and Automation Systems.

The project was named Parent Child Unmanned Aerial Vehicle (PCUAV) to describe the combination of the large and small vehicles. The objective of the project was to design, develop, and test prototypes of this system-of-systems that coordinates cooperative, unmanned vehicles having interfaces with recovery and communications systems on the ground.

During the first year of the project, it was found that the communication range of most MAVs is limited to about one kilometer due to the limited power capability of small vehicles. But many mission scenarios that the team identified require that the MAVs fly below 100 meters and the parent vehicle flies above 2 kilometers. So it was decided to introduce two mid-sized UAVs for the communication relay from the MAVs to the parent vehicle. This mid-sized UAV was named 'mini' by the team.

One typical potential concept of the PCUAV system is shown in Figure 1-1, where the mini vehicles play the role of communication relays between the parent vehicle and the MAVs or Micro sensors. The system enables the ground station to know what is happening over the mountain without using a satellite communication link.

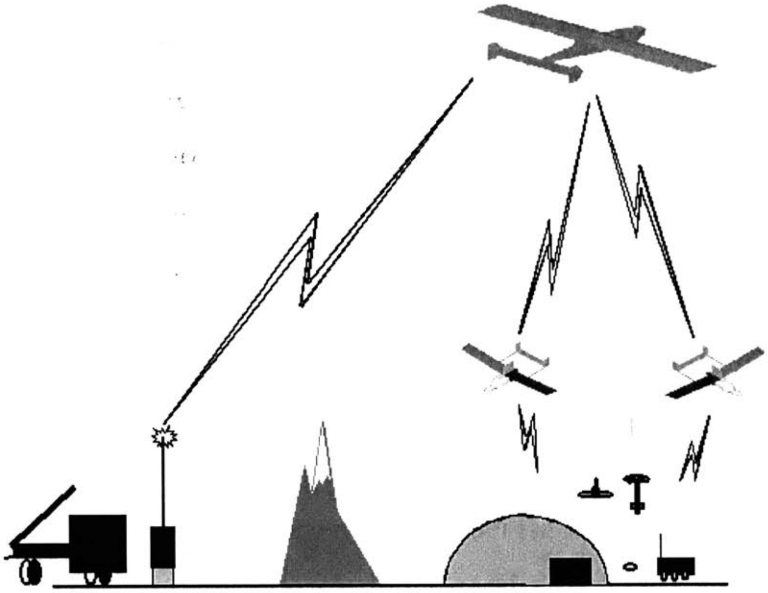

Figure 1-1: PCUAV concept

Two options were considered for sending the mini vehicles from the ground station to the mission site. One was to send the minis independent of the parent. The other option was to have the parent carry the two mini vehicles to the mission site and deploy them. The team chose the second option based mainly on its superior range and endurance. Various concepts for the integration of the parent and the two minis were then considered. The study of the vehicle integration concept, which was performed in the first year, is detailed in chapter 2.

It was pointed out that sustained presence of the mini vehicle would be a valuable feature of this type of system. This could be efficiently achieved by reintegrating the mini vehicle with the parent for refueling and recovery of the mini vehicle. As a part of the second year effort, rendezvous between two vehicles became a major focus of the project. The control system development for this task is detailed in chapters 3 and 4.

1.2 Thesis Overview

The objectives of this thesis are to summarize the concept development for the vehicle integration and the control system development for the mid-air rendezvous between the parent and mini UAVs, and to state the lessons learned in the process.

Specifically, chapter 2 describes conceptual design of the parent and mini vehicles, and the various integration concepts that the team considered. For the downselection of the final integration concept, performance of each concept was estimated, and the stability and controllability properties before and after the deployment of the mini vehicle were investigated.

Chapter 3 describes the concept generation for the reintegration between the parent and the mini vehicles, and then it details the control system development for the mid-air rendezvous.

Chapter 4 describes the development process for the vision based positioning system, which was used as a position sensor for the reintegration of the two vehicles.

Chapter 2

Vehicle Integration Concept Study

The purpose of this chapter is to describe the parent-mini vehicle integration concepts, to compare them, and to downselect to the configuration that will be developed further.

2.1 Parent-Mini Vehicle Integration Concepts

A number of configurations for the parent and mini vehicles were generated, and integration configurations involving various combinations of parent and mini were studied. For the comparison and downselection, the team performed analysis on each integration concept to obtain aerodynamics, stability, and performance properties. Each vehicle - parent and mini - was designed at the conceptual level. In other words, the configurations, sizes and weights of parent and mini vehicles were determined in the analysis. This process was primarily done by using the Athena Vortex Lattice program (AVL). This program is briefly described in Section 2.2.

2.1.1 Parent and Mini Vehicle Design

The overall procedure followed in developing the various parent-mini vehicle integration concepts was as follows: The design of the parent and mini vehicles started with a mission profile with a range of 100 km and a certain period of loiter time. From that, fuel weight and total vehicle weight at take-off were estimated. Next, range for the wing loading and span of both the parent and mini vehicles were selected. Then, a number of potential parent and mini vehicle configurations were designed. The following is the detailed description of the vehicle design procedure.

Mission profile

The two mission profiles used are shown in Fig 2-1. They have the same fuel weight and vehicle weight, as explained below. For both cases the range is 100 km. The difference lies in whether the minis fly home by themselves or they are reintegrated with the parent. First, option 1, where the minis fly back by themselves, was considered. A mini loiter time was chosen to be 40 minutes, because the envisioned endurance of micro aerial vehicles is approximately 20 minutes, and since the parent vehicle is capable of carrying four MAV's and two minis, each mini should at least have an endurance of approximately 40 minutes. Next, option 2, in which the reintegration is included, was considered. If the mini is reintegrated with the parent such that it can use what would otherwise be cruise-back fuel at the mission site, it was estimated that the mini's loiter time is increased to two and a half hours. In summary, in the

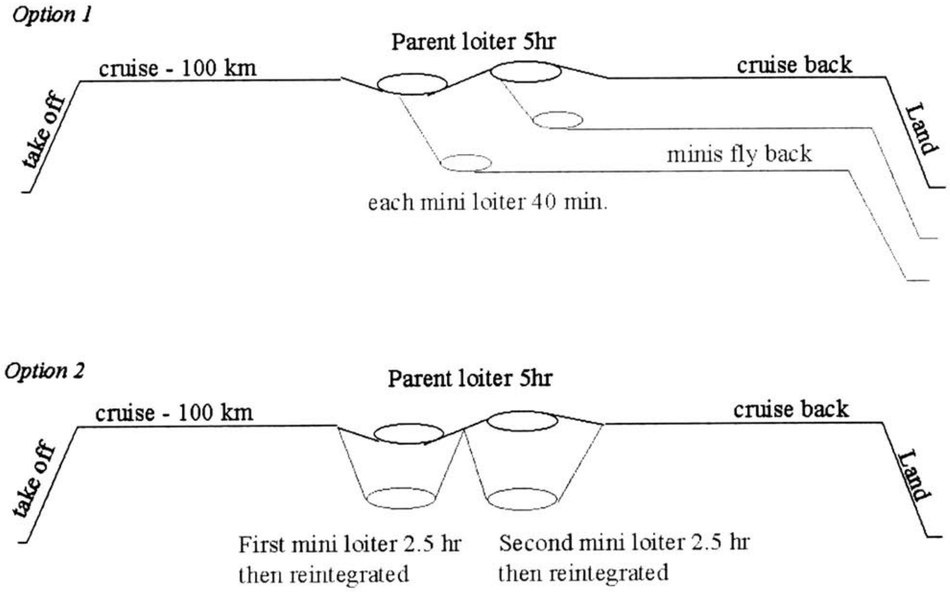

Figure 2-1: Mission profile

case of option 2, the parent flies 100 km, loiters for 5 hours while each mini loiters for two and a half hours, reintegrates, then flies back. In option 1, the parent flies 100 km, loiters for 5 hours, and returns. In the mean time, the minis are deployed, loiter for 40 minutes, then fly back by themselves.

Weight estimation

Based on the chosen mission profile, vehicle weights were estimated. The team carried out the takeoff weight buildup method, in which the takeoff gross weight is assumed to be composed of the empty weight, payload weight, and fuel.

$$W_{TO} = W_{payload} + W_{empty} + W_{fuel}$$

The empty weight includes structure, avionics and engine. The payload weight includes two minis and four micros. The following is the procedure for weight estimation. First, the payload weight is fixed. Next, assuming a takeoff weight, fuel weight is computed by flying the vehicle through the mission profile. In this step, the Breguet range and endurance equations are used. Then, the empty weight is obtained simply from the equation above. On the other hand, the ratio of empty weight to takeoff weight is compared with the trend of other UAVs, which is shown in Fig 2-2. The approximated equation for this trend is

$$W_{empty} = 10^{\frac{\log_{10} W_{TO} - A}{B}},$$

where A=0.1482, B=1.0228. The iteration continues until the ratio falls near the empirical correlation. Table 2.1 shows the weight fraction of the mini and parent vehicles. The total weight of each mini is 1.5 kg and the takeoff weight of the parent is 17.7 kg. It should be noted that these numbers are slightly different from those of the vehicles which were further modified in the detailed design level in the second year of the project.

Selection of wing loading and wing span

The 1.5 kg total weight of the mini vehicle indicates that it is in the class of RC aircraft. Since the main role of the mini is to loiter at the mission site, it is desirable

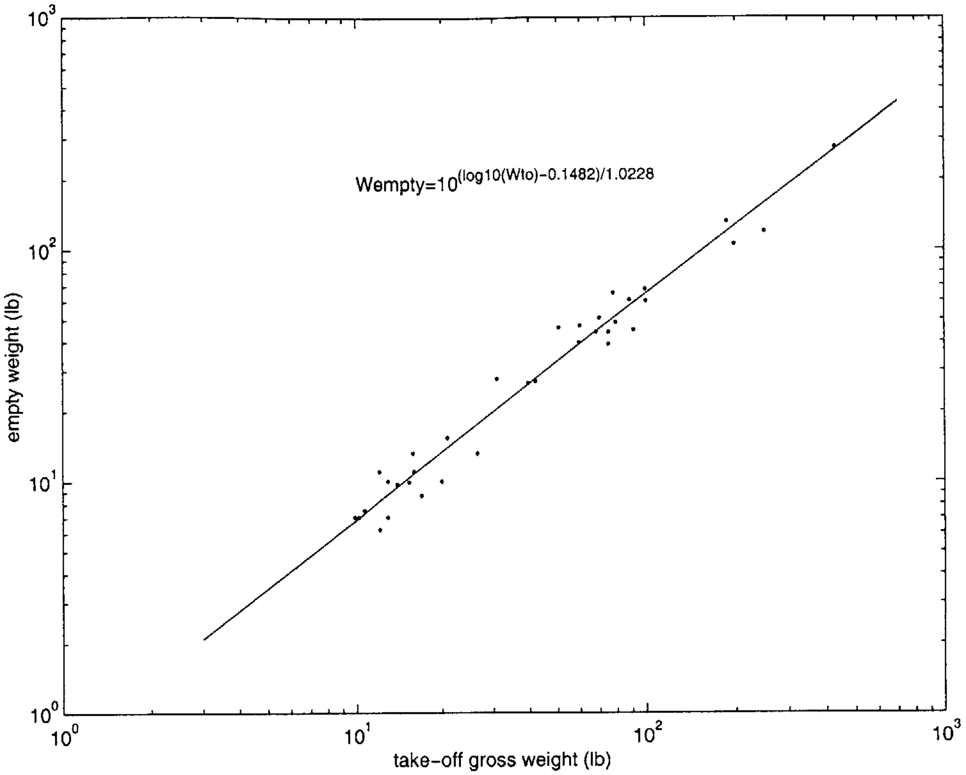

Figure 2-2: Empty weight fraction trend for UAV's

for the mini to have relatively low wing loading, so its wing loading was limited to around 20 oz/ft^2. The parent vehicle, because it must deploy and reintegrate the mini, should have similar wing loading. If the parent wing loading is much higher, the mini vehicles would have difficulty during reintegration to keep up with the parent, which would have to fly fast if it were designed with high wing loading. Thus the wing loading of the parent vehicle with the mini's integrated was chosen around 30 oz/ft^2. The span of the parent vehicle, to achieve ease of use and two-man portability, was restricted to a maximum of 4 meters.

Parent vehicles

Three parent vehicles were designed by the first year of the project (Figure 2-3). Two main planforms - conventional and all-wing configuration - were studied. These parent vehicles all have about three meter wingspans. The size of the fuselage was determined primarily based on the volume of the payloads. Figure 2-3 (b),(d), and (f)

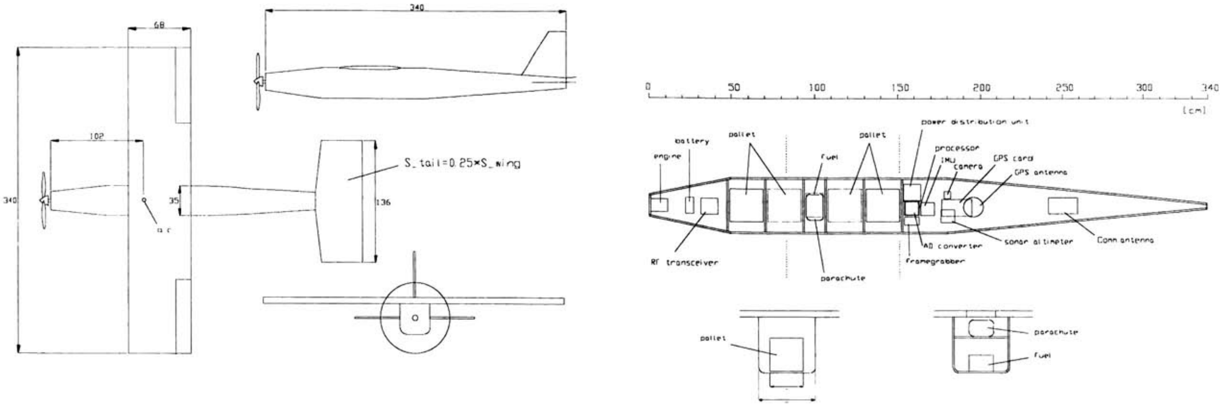

(a) Parent 1

(b) Internal Layout of Parent 1

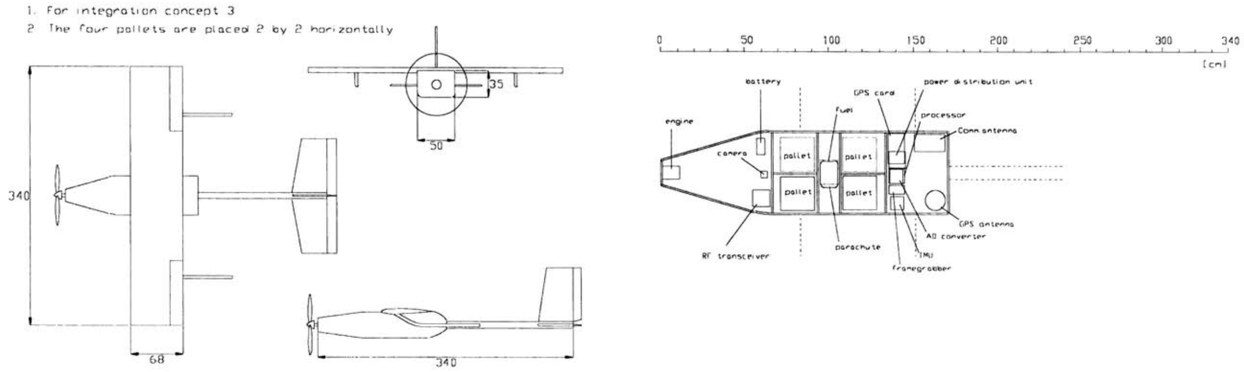

(c) Parent 2

(d) Internal Layout of Parent 2

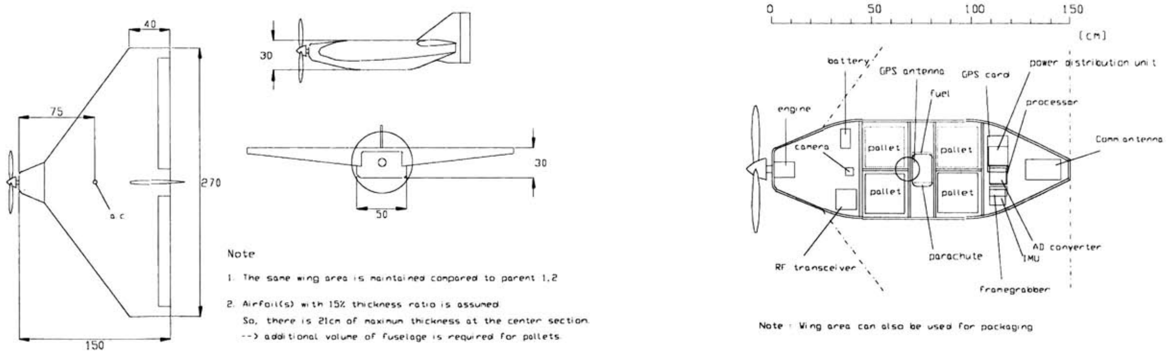

(e) Parent 3

(f) Internal Layout of Parent 3

Figure 2-3: Parent Vehicles

Mini Vehicle

Avioncis & Battery	Structure	Engine	fuel	Total
800 g	400 g	200 g	100 g	1.5 kg

Parent Vehicle

Payload		Empty weight			Fuel	W_{TO}
2 Minis	4 Micros	Structure	Avionics	Engine		
3.0 kg	1.6 kg	6.3 kg	3.4 kg	2.0 kg	1.4 kg	17.7 kg

Table 2.1: Weight Fractions

show the internal layouts of the parent vehicles. The location of each component was determined by considering center of gravity, engine vibration, and connections among the components. For example, the four pallets to contain micro vehicles or sensors are placed near the desirable center of gravity (c.g.) so that after their deployment the c.g. stays within an acceptable range. The same reasoning applies to the selection of the fuel tank location. Many electric components are located away from the engine. It is expected that there will be some changes and additions of the electric components during the avionics design. Thus, the main purpose of the internal layout at this stage of the conceptual design was to ensure a sufficient volume of fuselage, with some margin, while the center of gravity is assured to be placed near the aerodynamic center of the wing. The descriptions of the three parent vehicles are as follows:

parent 1 This conventional-shaped vehicle has a wingspan of 3.4 meters with aspect ratio of 5. Its fuselage contains the four pallets arranged in a line. The horizontal tail can be placed on top of the vertical tail, which forms a T-tail, depending on the integration concepts. The team first gave attention to this conventional shape because it has a long moment arm for tail surfaces, so it is generally regarded as more reliable than an all-wing configuration when severe changes of c.g. and/or neutral point shifts occur due to deployment of minis and micros. The study of the shift of c.g. and neutral point is described in Section 2.2.2.

parent 2 This vehicle has a wider fuselage than parent 1, so it contains the pallets in a 2 by 2 horizontal array, which reduces the effect of the c.g. change caused by the pallet deployment compared to the parent vehicle 1.

parent 3 This all-wing configuration has a wingspan of 2.7 meters with aspect ratio of 3. But the same wing area is maintained compared to parent 1 or 2. Airfoils with 10-15 % thickness ratio are assumed. However, this thickness is not enough to contain pallets. Thus additional volume of the fuselage is required for the packaging. The pallets are placed 2 by 2 around the cg location, where fuel tank is also positioned. The volume of the wing can also be used for packaging. A reflected airfoil was used for the all-wing parent vehicle.

Mini vehicles

Three different mini vehicles were designed (Figure 2-4). The design procedure of the individual Mini vehicles is similar to that of the parent vehicles. The mini vehicles have about one meter wing span and an estimated weight of 1.5 kilograms.

2.1.2 Vehicle Integration Concepts

The mini-parent vehicle integration is one of the unique features in the PCUAV system. Some of the criteria that were emphasized in the selection of the integration concepts include the following:

- Stability and control surface capabilities should be considered. The parent vehicle will deploy two mini vehicles and four micros. This will cause the center of gravity to shift significantly. Furthermore, depending on the parent-mini integration concept, it may also change some aerodynamic properties, which will change the stability characteristics, such as the neutral stability point. Thus, minis should be placed in such a way that the deployment of the vehicles does not move the center of gravity beyond the acceptable c.g. range.

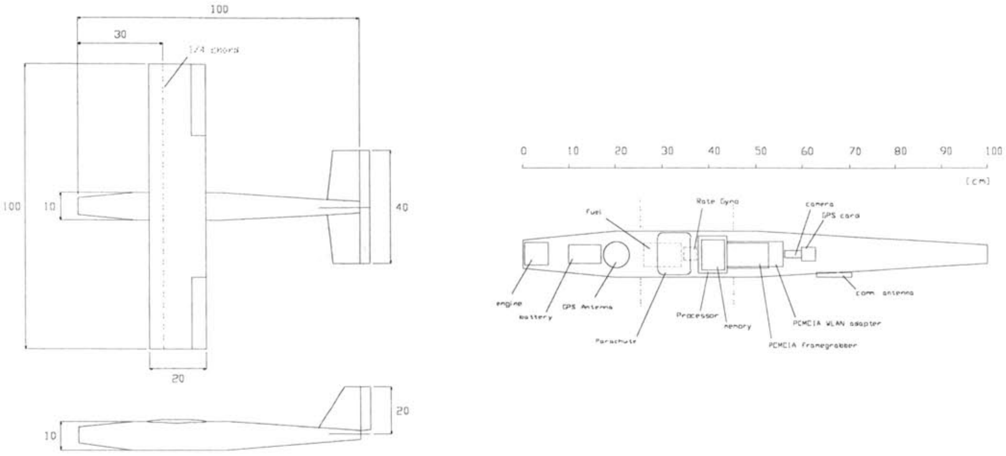

(a) Mini 1 (b) Internal Layout of Mini 1

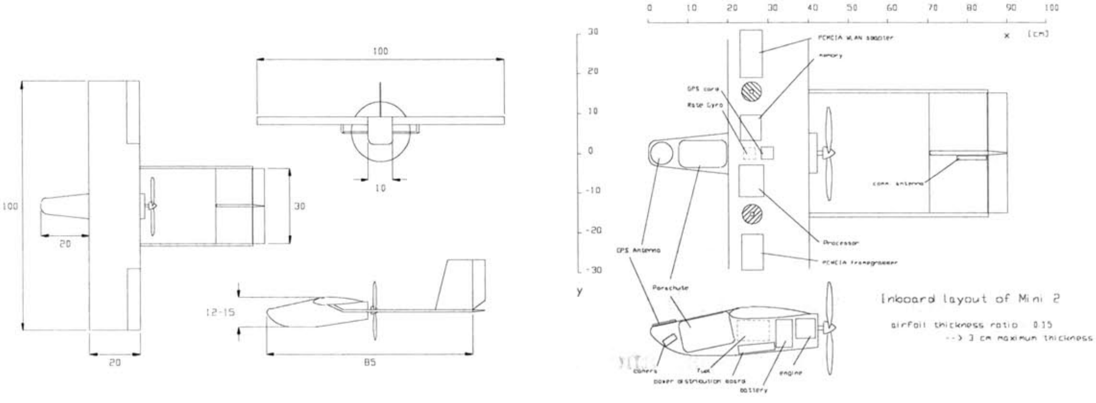

(c) Mini 2 (d) Internal Layout of Mini 2

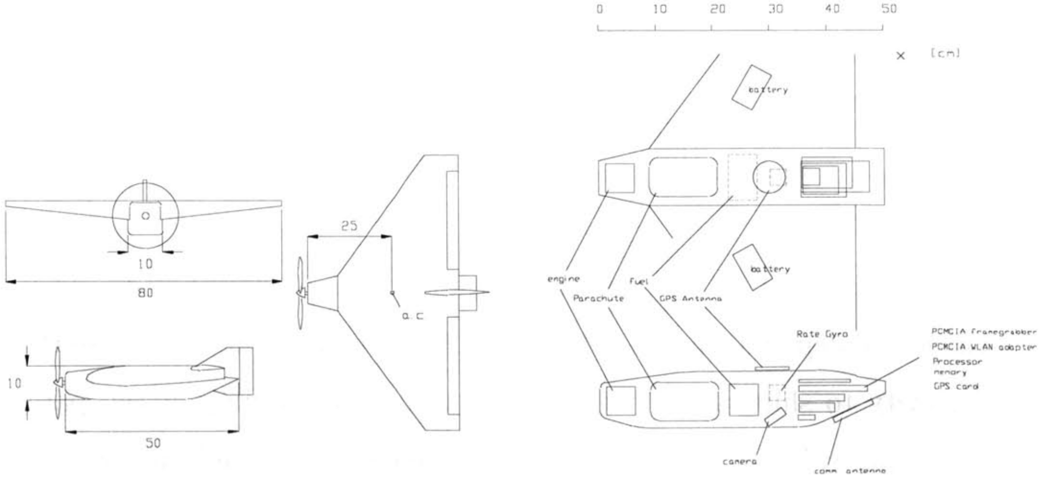

(e) Mini 3 (f) Internal Layout of Mini 3

Figure 2-4: Mini Vehicles

- Since the addition of the minis to the parent vehicle implies increased total weight, it is desirable for the mini wings to generate lift in the integrated configuration.

- Reliable deployment is one of the most important requirements. Therefore, the deployment mechanism should be simple, the locations should favor regions of stable air flow, and the clearance to obstacles such as the tail or propeller should be large for safe deployment.

- The integration of the mini vehicles to the parent should be done in a way that the total wetted area increases as little as possible, since skin friction is a major contributor to total drag.

- Mid-air rendezvous is another feature of the PCUAV system. Thus, the vehicle integration should be compatible with this requirement.

Figure 2-5 shows all the parent-mini integration concepts generated by the first year team. Detailed analyses are described in the next sections. However, some of the features for each concept are as follows:

Concepts 1 and 1b in Figure 2-5 show a configuration where the upper surface of the Mini's wing is attached to the lower surface of the parent's wing in such a way to reduce the wetted area. The disadvantages include difficulties in selecting the parent's airfoil and in manufacturing the two surfaces, since they should match very accurately in flight. The T-tail is considered appropriate for the parent vehicle in order to provide more clearance for the deployment of minis.

Concept 2 is the integration where only the mini's fuselage is attached under the parent's wing. In this case the biplane effect is expected, where the additional wing provided by the mini is not very helpful in generating lift due some cancellation of the vortices generated by the two lifting surfaces.

Concept 3 was generated to avoid the biplane effect, but is expected to have large drag due to the increased wetted area.

Concepts 4, 4b, and 6, which place the minis on top of the parent's fuselage, were considered for safe deployment and less complexity. It was found in the analysis that

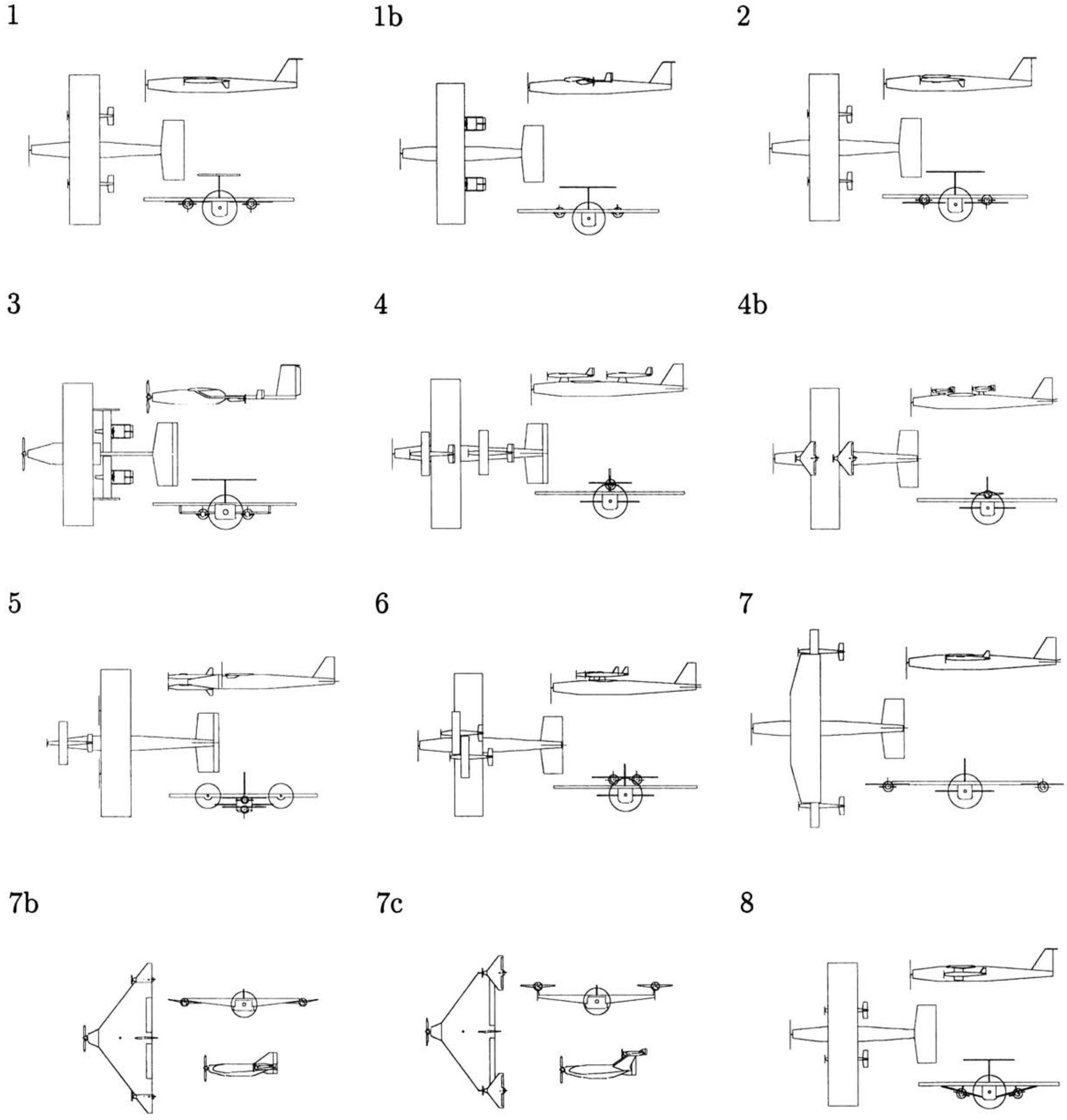

1

1b

2

3

4

4b

5

6

7

7b

7c

8

Figure 2-5: Vehicle Integration Concepts (first year) the rear-placed mini generates almost no lift due to the downwash generated by the front-placed mini.

In concept 5, which places the minis at the front of the parent vehicle, the mini is assumed to be deployed forward with respect to the parent. Therefore, this concept provides good conditions for the mini deployment since it does not expose the minis to the downwash turbulence generated by the parent vehicle and, as long as the mini can fly faster than the parent, clearance for the mini deployment is insured. The disadvantages include the large wetted area and the large tail surface required for the parent vehicle. The latter is because as long as the mini's wing is fixed, it will destabilize the longitudinal mode, which will therefore require large tail area to ensure longitudinal stability.

In Concepts 7, 7b, and 7c, the minis are attached at the wing tip of the parent's wing, resulting in increased aspect ratio. It will be shown later in the analysis that the aerodynamic characteristics and thus performance are improved by placing the minis in this way. In particular, concept 7b uses all-wing configuration airplanes for the parent and minis, which has less wetted area. The resultant reduced skin friction drag improves the cruise range and maximum speed.

2.2 Integration Concepts Analysis

The integration concepts were compared in terms of static performance parameters such as maximum speed, range, endurance and rate of climb. The analysis for the static performance is described in Section 2.2.1.

It should be noted that the parent vehicle will experience a shift of the center of gravity due to the deployment of the minis and possibly a change of the neutral stability point - the aerodynamic center of the vehicle - depending on the integration concept. So it is important that the c.g. lie in an acceptable range before and after the deployment. Section 2.2.2 deals with this problem.

This analysis was based on the aerodynamic data obtained from the Athena Vortex Lattice (AVL) code. This program employs the vortex lattice method [5], and is available on Athena (MIT computer network). Basically, this code takes the vehicle's geometric information and flight condition, such as angle of attack and flight speed, and computes lift, induced drag, lift loading distribution, stability derivatives, etc. It can also find the trim flight conditions for given control surface deflections. In this analysis, the effect of the fuselage was not considered. The airfoils assumed in this study are (1) the e374 low Reynolds number airfoil for the conventional aircrafts (parent 1,2, and mini 1,2) and (2) MH 61 for the tailless aircrafts (Parent 3 and Mini 3) [8]. Figure 2-6 shows examples of the geometric input to AVL.

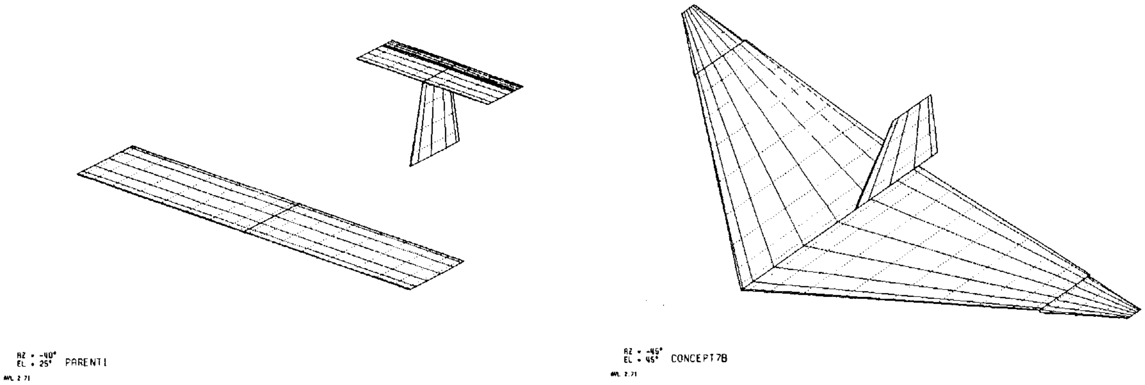

(a) Parent 1 (b) Concept 7b

Figure 2-6: Examples of AVL models

2.2.1 Performance comparison of the integration concepts

First, for each concept, the relations between C_L and C_D were obtained. Based on these relations the speed vs. power curves were obtained. Then the performance features for the integration concepts were derived from those relations.

The analysis shows that the integration concept 7b (Figure 2-7), where the minis are attached at the wing tip of the tailless parent has many good features in terms of static performance. The two major reasons for this result are considered to be (1) the relatively low surface area due to the use of tailless planform and (2) the increased aspect ratio resulting from the integration.

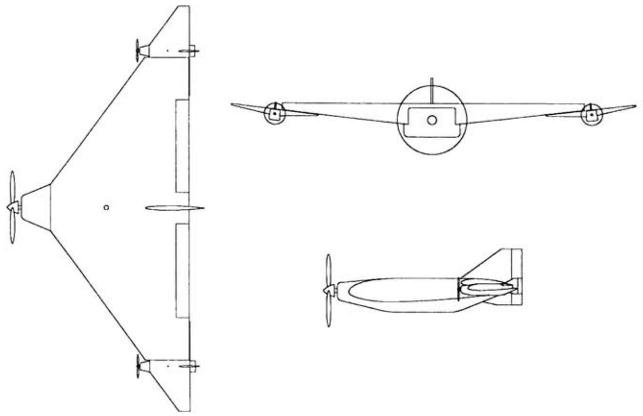

Figure 2-7: Integration Concept 7b

C_L vs. C_D relations

Using the Athena Vortex Lattice program, the relations between angle of attack and the lift and drag coefficients were obtained.

For the low-speed airplanes, the drag can be considered mostly to be the sum of the skin friction drag and the induced drag. Since the vortex lattice method calculates only the induced drag, the skin friction drag (C_{D_0})values were estimated by a simple approximate equation:

$$C_{D_0} = C_{fe} \frac{S_{wet}}{S_{ref}}$$

where $C_{fe} = 0.0055$ (for light Aircraft - single engine), S_{wet} is the vehicle's wetted area, and S_{ref} is the reference area [6]. The sum of the skin friction drag and the induced drag from the AVL program gives C_D as a function of angle of attack. C_L vs. angle of attack is directly calculated from AVL. Using these, C_L vs. C_D can then be derived.

Figure 2-8 shows the drag polars for the integration concepts. In the graph there are two main branches: one is for the integration concepts where the conventional parent vehicles are used and the other is for the concepts where all-wing parent is used. Because of the lower wetted area in the all-wing cases (7b, 7c), the drag polars start at smaller drag values.

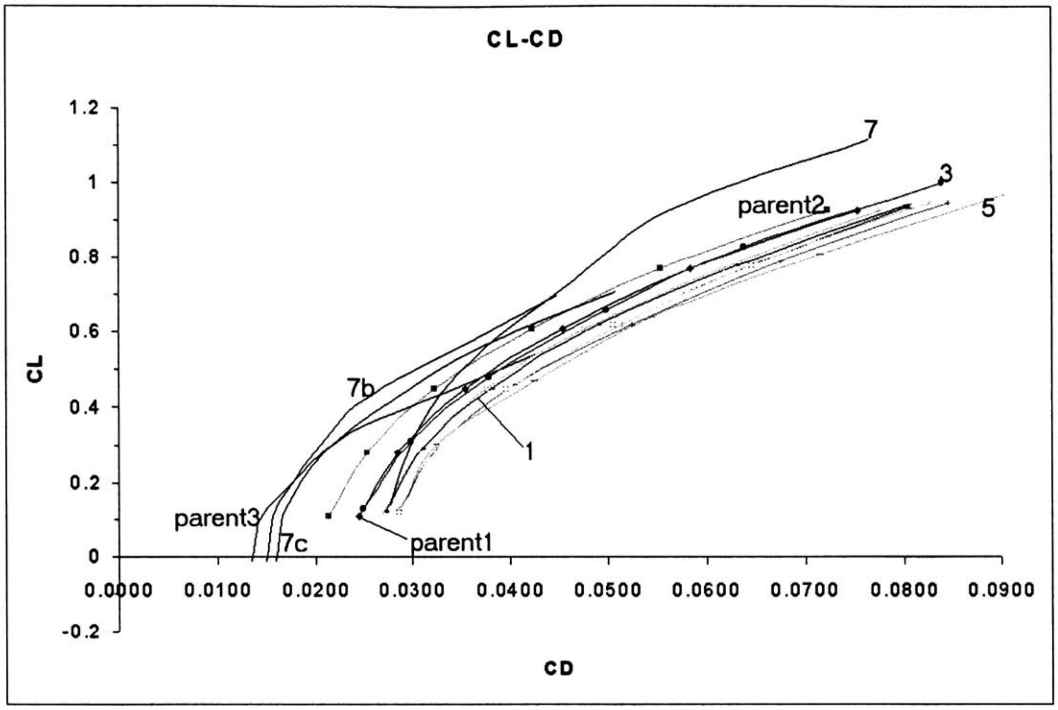

Figure 2-8: Drag polars for integration concepts

Speed vs. Power relations

To obtain performance characteristics, we need a relation between flight speed and power required during level unaccelerated flight. This relation is obtained through several steps. First, a reasonable range of the flight speeds is specified and the required lift coefficients(C_L) are computed using the equation

$$C_L = \frac{W}{\frac{1}{2}\rho V^2 S}$$

Next, the value of C_D is found from the $C_L - C_D$ relation. Then, the thrust required is obtained by the approximate equation derived from one of the level unaccelerated flight conditions

$$T = W\frac{C_D}{C_L}$$

Finally, the power required($HP_{required}$) is calculated by the relation

$$HP_{required} = \frac{TV}{746\eta_p}$$

where η_p is the propeller efficient. Figure 2-9 shows the results of the above process for the integration concepts. There are two main branches in the graph: the upper

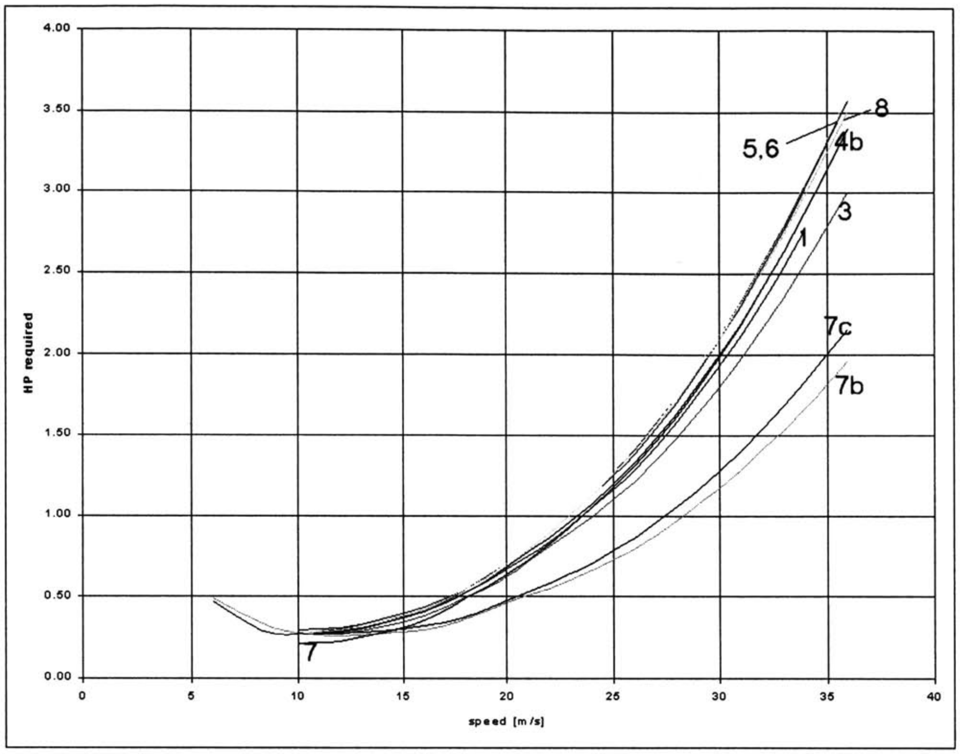

Figure 2-9: Flight speed - Power required

one is for the concepts in which the conventional parent vehicles are used, while the lower one is for the concepts with all-wing configuration as a parent vehicle. The main reason for this difference is considered to be the lower wetted area in concepts 7b and 7c.

Static Performance - Maximum speed, Range and Endurance

With the speed-power relations, some of the static performance parameters can be obtained. This can be explained using Figure 2-10 (concept 1) as an example. If a straight line is drawn from the origin, tangent to the power required curve, the contact point corresponds to the optimal cruise condition for a propeller aircraft, which maximizes the lift-drag ratio. If a horizontal line is drawn, again tangent to the curve, the contact point is for the optimal loiter condition which minimizes the fuel consumption. Regarding the maximum speed, if it is assumed that the 2HP engine is used, the actual practical power available from the engine is about 80%,

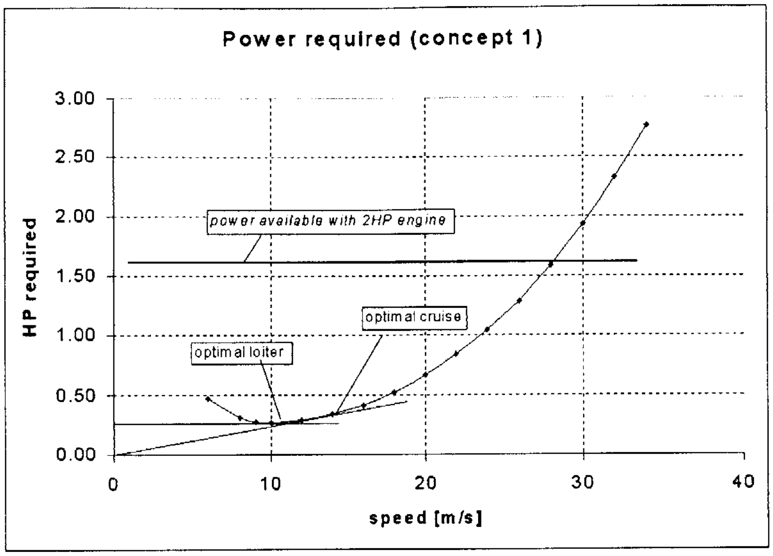

Figure 2-10: Performance characteristics in $V - HP_{required}$

which is 1.6 hp. The horizontal line at 1.6 hp shows this available power. In a more realistic analysis, the line for the available power would be slightly speed dependent. The intersection of the power available and the power required corresponds to the maximum flight speed condition. Additionally, the maximum difference between the power available and the power required is proportional to the maximum climb rate.

Figure 2-11 shows the results of the procedure. Regarding the maximum speed, it turns out that concepts 7b and 7c can fly faster than the other configurations. The primary reason is lower drag due to the use of the tailless planform. To compare the range capabilities, it was assumed that 0.5 lb. of fuel is used and the weight change of the vehicle during the cruise is not significant. The result shows that concepts 7 and 7b can fly further than the other concepts, due to the increased aspect ratio resulting from the integration. The endurance capabilities are obtained from the optimal loiter conditions. It turns out that concept 7, which is a conventional parent with minis at the wing tips, has better loitering capability than the others.

From the point of view of static performance, concept 7b turns out to be the most efficient choice. Again, this is because this configuration has two major advantages, which are lower wetted area due to the use of the tailless vehicles and the increased aspect ratio because of the way the minis are integrated. Another conclusion is

Max. Speed (assumption : 1.6 HP is available)

	Speed [m/s]	[mi/h]	CL	CD	CL/CD
concept 1	28.0	63	0.14	0.0267	5.2
concept 2	27.0	61	0.15	0.0295	5.1
concept 3	28.5	64	0.13	0.0249	5.2
concept 4	27.0	61	0.15	0.0295	5.1
concept 4b	27.5	62	0.14	0.0276	5.1
concept 5	27.0	61	0.15	0.0286	5.2
concept 6	27.0	61	0.15	0.0292	5.1
concept 7	27.5	62	0.14	0.0273	5.1
concept 7b	33.5	75	0.09	0.0151	6.0
concept 7c	32.5	73	0.10	0.0166	6.0
concept 8	27.0	61	0.15	0.0297	5.1

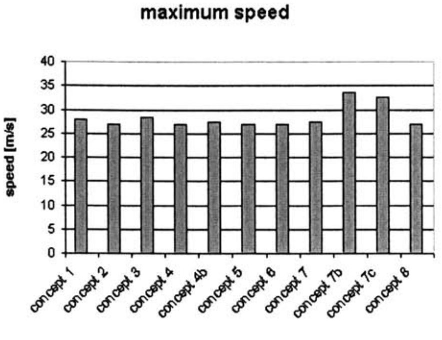

(a) Maximum Speed of Integration Concepts

Cruise

	[m/s]	[mi/h]	CL	CD	CL/CD	HP	a.o.a	[km] Max. range
concept 1	14.0	32	0.57	0.046	12.4	0.34	5.5	106
concept 2	13.5	30	0.62	0.052	11.9	0.34	6.0	102
concept 3	13.0	29	0.65	0.051	12.7	0.30	6.0	111
concept 4	14.0	32	0.57	0.048	11.9	0.36	5.5	100
concept 4b	13.5	30	0.62	0.05	12.4	0.33	6.0	105
concept 5	13.5	30	0.62	0.055	11.3	0.35	6.0	99
concept 6	13.5	30	0.62	0.051	12.2	0.34	6.0	102
concept 7	12.0	27	0.77	0.048	16.0	0.23	6.0	134
concept 7b	16.5	37	0.39	0.024	16.3	0.31	5.5	137
concept 7c	15.0	34	0.47	0.032	14.7	0.31	7.0	124
concept 8	13.0	29	0.67	0.056	12.0	0.33	6.5	101

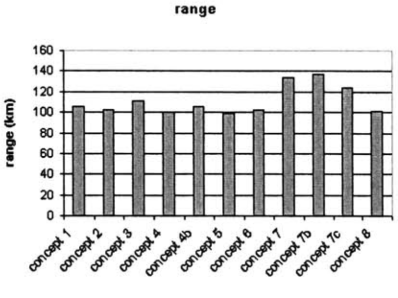

Note: elevator deflection required for concept 7b = -3 degree if cg is at 68
>> allowable

assumption : 1. Fuel 0.5 lb, 2. Weight change is negligible

(b) Cruise Performance of Integration Concepts

Loiter

	[m/s]	[mi/h]	CL	CD	CL/CD	HP	a.o.a	[hr] Max. endurance
concept 1	10.0	23	1.11	0.100	11.1	0.27	11	0.53
concept 2	10.0	23	1.11	0.100	11.1	0.27	11	0.53
concept 3	11.0	25	0.94	0.080	11.8	0.26	9	0.55
concept 4	10.0	23	1.11	0.100	11.1	0.27	11	0.53
concept 4b	10.0	23	1.11	0.100	11.1	0.27	11	0.53
concept 5	10.0	23	1.11	0.110	10.1	0.30	11	0.48
concept 6	10.0	23	1.11	0.100	11.1	0.27	11	0.53
concept 7	10.0	23	1.11	0.076	14.6	0.21	10	0.68
concept 7b	13.0	29	0.64	0.045	14.2	0.26	9	0.55
concept 7c	12.0	27	0.74	0.058	12.8	0.28	10	0.51
concept 8	10.0	23	1.11	0.100	11.1	0.27	11	0.53

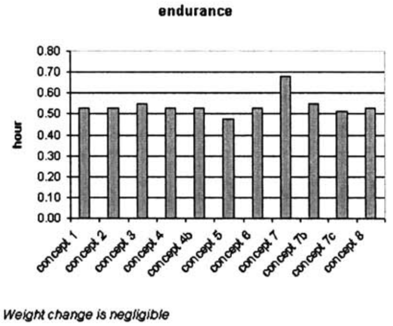

Note: elevator deflection required for concept 7b = -5.5 degree, if cg is at 68
>> allowable

assumption : 1. Fuel 0.1 lb, 2. Weight change is negligible
3. Straght level flight

(c) Loiter Performance of Integration Concepts

Figure 2-11: Static Performance of Integration Concepts that all the other configurations have roughly the same performance so that other considerations would dictate which one is chosen. These considerations are considered in the next section.

2.2.2 Stability and Controllability of the Parent Vehicle

As mentioned earlier, deployment of the minis and micros involves center of gravity changes and shifts of the neutral point (NP) depending on the integration concepts. Thus a study of the movement of the c.g. and neutral point is essential. It should be ensured that the c.g. is located in front of the neutral point for static stability, but not too far in front, or elevator deflection required to trim the aircraft will be large, increasing drag and reducing maneuverability. These two conditions should be guaranteed throughout the flight, before and after deployment of the minis.

Two kinds of comparison were performed. The first is the comparison between the conventional parent vehicle (parent 1,2) and the tailless parent (parent 3). It was found that the conventional planform has a larger stable center of gravity range than the tailless parent. Concern about the small c.g. range of the tailless shape led to a second analysis, which was done for the integration concept 7b. Since this concept involves not only a c.g. change but also a shift of the neutral point, the comparison was performed for the two possible configurations in this concept, that is before and after mini-deployment.

Backward limit of C.G.

The backward limit of the c.g. is the neutral point so as to ensure the vehicle's longitudinal static stability. The location of the neutral point from any reference position is obtained by the relation:

$$\frac{NP}{\bar{c}} = \frac{X_{ac}}{\bar{c}} - \frac{C_{M_\alpha}}{C_{L_\alpha}}$$

where $\bar{c}$ is the mean aerodynamic chord, C_{M_α} and C_{L_α}, the coefficients of moment and lift due to angle of attack , are obtained from AVL, and X_{ac} is the location of the aerodynamic center of the wing. Choosing the reference position at the leading edge of the mean aerodynamic chord, $X_{ac}/\bar{c}$ is ~0.25 for subsonic flight. The table below shows the backward limits of the parent vehicles 1, 2, and 3, and the integration concept 7b. The numbers for $NP - X_{ac}$ represent the backward limit from the reference position, which is chosen to be at 1/4 of the mean aerodynamic chord.

	Parent 1,(2)	Parent 3	Integration 7b
$\bar{c}$ [m]	0.68	0.99	0.99
C_{M_α}	-1.81	-0.094	-0.458
C_{L_α}	4.71	3.26	4.05
Backward limit from $1/4\bar{c}$	26 cm ($0.38\bar{c}$)	3 cm ($0.03\bar{c}$)	11 cm ($0.11\bar{c}$)

The table shows that the all-wing configurations have shorter backward limit from the reference point than the conventional frame. Integration concept 7b has a larger backward limit than parent 3. That is because the location where the mini is integrated is far behind the c.g. of parent 3, and the mini's wings are exposed, and play a similar role as tail.

Forward limit of C.G.

The forward c.g. limit is related to the capability of the elevator to trim the aircraft. In general, as the c.g. moves forward, larger elevator up-deflection is required to trim the vehicle. Control surfaces such as elevator, ailerons, and rudder, can be modeled in the Athena vortex lattice program by adding a strip of surface at the trailing edge of the wing. This is shown in Figure 2-6 (a).

The way the forward limit was computed is the following. During trimmed normal flight such as cruise or loiter, C_L should be reasonably high (e.g. more than 0.3 or 0.4), otherwise the aircraft must fly too fast, resulting in an inefficient aircraft. The elevator up-deflection to trim the vehicle should not be too large (e.g. less than 5 degrees). Figure 2-12 shows the relations between C_L and elevator deflection for trimmed flight of parent 1(or 2), 3, and integration 7b. For each vehicle type, the relations are drawn for various locations of the center of gravity. The distances of the

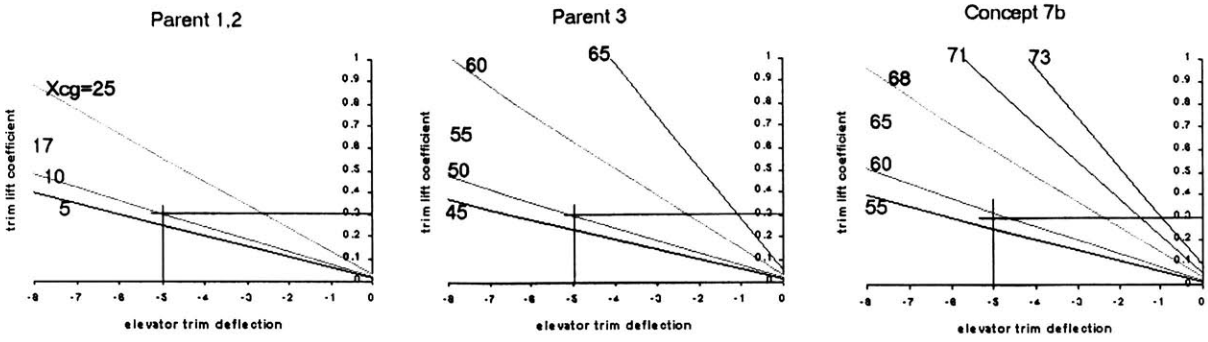

17-10 = 7 cm from a.c.

65-50 = 15 cm from a.c.

65-60 = 5 cm from a.c.

Figure 2-12: Trim lift coefficients vs. elevator trim deflection

c.g. labeled on each line of the graphs are taken from the leading edge of the root chord. The locations of the aerodynamic center (a.c.) are reference points to compute the forward limits in this analysis. They are 17 cm (from the leading edge of the root chord) in the case of parent 1,2 and 65 cm in the case of parent 3 and concept 7b respectively. Thus, in order to get a forward limit from the 1/4 $\bar{c}$, if we impose the requirement that (1) C_L be > 0.3 and (2) elevator deflection be < 5 degrees, the line corresponding to this condition, for example, in the case of the parent 1 is the one with c.g. at 10 cm. Therefore, the forward limit is 7 cm forward from the reference position(1/4 $\bar{c}$).

If the above calculations on the forward and backward limits are combined together, the allowable c.g. ranges are obtained as shown in Figure 2-13 for the parent vehicle 1(or2) and 3. The backward limit is fixed as the neutral point. In the case of the forward limit, several conditions on the lift coefficients can be specified, which results in several forward limits corresponding to the C_L requirements. Here, 0.3, 0.4, and 0.5 of C_L are specified. The result indicates that the tailless configuration (parent 3) has less freedom of the c.g. location than the conventional shape (parent 1,2). But both are consistent with micro deployment, which will cause up to about 3 cm of c.g. change. If the mini deployment simply changes the c.g. position without causing a shift of the neutral point, the c.g. shift should not exceed those ranges in the Figure 2-13.

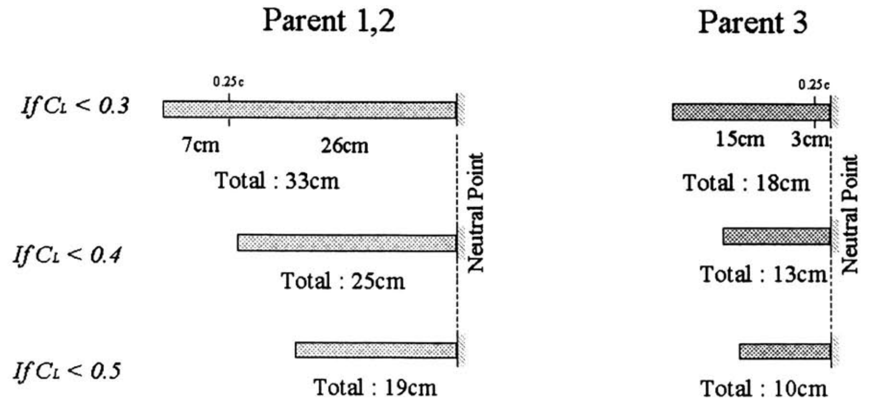

Figure 2-13: Allowable c.g. ranges for parent vehicles (Note: $\bar{c}$=68 cm for parent 1,2, $\bar{c}$=99 cm for parent 3)

Figure 2-14 shows the allowable ranges of c.g. for integration concept 7b before and after mini deployment. The c.g. change from the mini deployments is 13 cm in

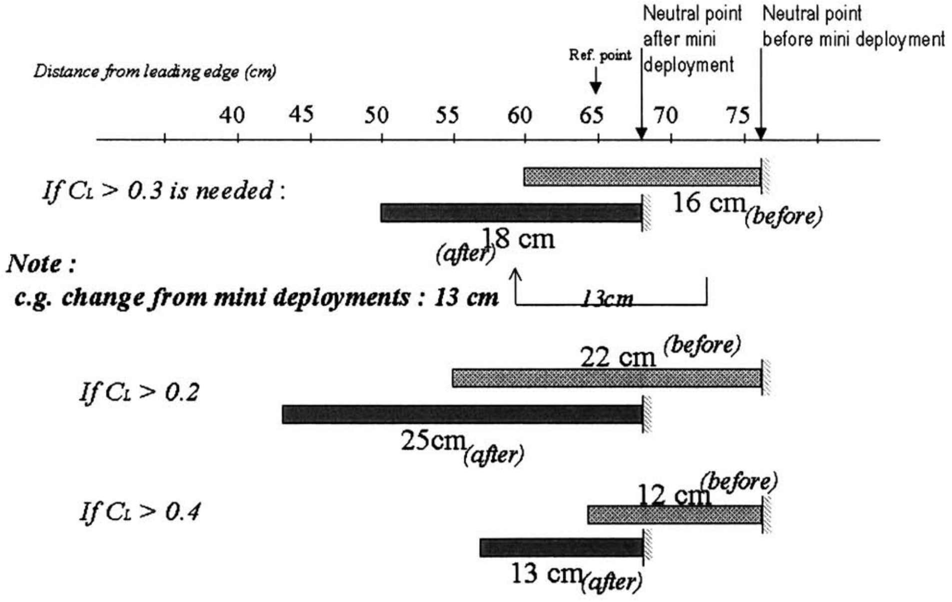

Figure 2-14: Shift of allowable c.g. range for concept 7b (Note: $\bar{c}$=99 cm)

this integration concept. Thus, this graph indicates that the longitudinal c.g. position can be placed within the allowable ranges both before and after the mini deployment. But this may not be practical because of the low static stability.

Effect of asymmetry caused by deployment of a single mini

In the second year of the project, six integration concepts were compared for the final selection. Two configurations among them are shown in Figure 2-15. These are variants of concept 7b with higher aspect ratio. The second concept in the Figure 2-15 has tail surfaces to improve the stability properties. The performance data and the analysis of the c.g. ranges for concept B are attached in Appendix A.

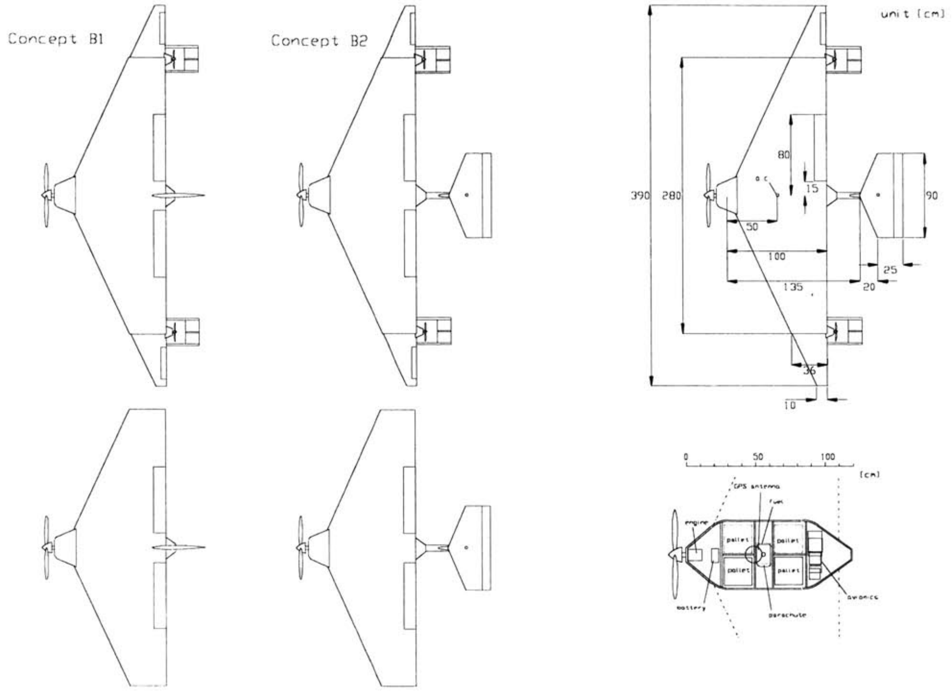

Figure 2-15: Integration concepts B

One of the concerns for concepts with the minis attached near the wing tips of the parent was the asymmetric condition which results from the deployment of a single mini. This effect is considered for concept B2 in the following. Four main changes during this situation are:

- shift of center of gravity
- asymmetric lift
- asymmetric drag

- asymmetric thrust by the potential use of the mini's propeller

The deployment of the mini is assumed to take place during the optimal cruise conditions of the integrated phase, which are

$$V = 16\ m/s,\ \alpha = 7.6^o,\ C_L = 0.63,\ \delta_e = -3^o$$

When the left mini is deployed first, the c.g. shift is estimated to be 13 centimeters to the right and 3 centimeters forward. The following are the changes of force and moment coefficients right after a single mini is deployed.

$$\begin{array}{cccc} C_L: & 0.63 & \longrightarrow & 0.54 \\ C_Y: & 0.000 & \longrightarrow & 0.002 \\ C_{D_{ind}}: & 0.0175 & \longrightarrow & 0.0172 \\ C_m: & 0.000 & \longrightarrow & 0.0291 \\ C_n: & 0.000 & \longrightarrow & 0.0001 \\ C_l: & 0.000 & \longrightarrow & \text{-}0.0292 \end{array}$$

These numbers are computed from AVL, where the same reference position, reference area, and lengths were used.

$$S = 2.15\ m^2,\ \bar{c} = 0.67\ m,\ b = 3.9\ m$$

$$reference\ position\ :\ (x, y, z) = (0.56, 0, 0)_{from\ the\ leading\ edge\ at\ root\ chord}$$

First, pitching moment is considered.

$$\begin{aligned} M_{about\ the\ reference\ position} &= M_{due\ to\ c.g.\ shift} + M_{aerodynamic} \\ &= -(W_{parent} + W_{mini}) \cdot (longitudinal\ c.g.\ shift) + \frac{1}{2}\rho V^2 S\bar{c}C_m \\ &= -4.76 + 5.36 \\ &= 0.6\ [N \cdot m] \end{aligned}$$

This shows that the two effects almost cancel each other.

Second, regarding the roll motion, the total roll moment about the reference point can be considered as:

$$\begin{aligned}
L_{about\ the\ reference\ position} &= L_{due\ to\ c.g.\ shift} + L_{aerodynamic} \\
&= (W_{parent} + W_{mini}) \cdot (lateral\ c.g.\ shift) + \frac{1}{2}\rho V^2 SbC_l \\
&= 20.6 - 31.3 \\
&= -10.7\ [N \cdot m]
\end{aligned}$$

This value is fairly large, and must be balanced by the ailerons. The rolling moment generated by ailerons can be estimated using wing strip theory by the relation

$$L_{aileron} = 2\bar{q}C_{L_\alpha}\tau\delta_a \int_{y_1}^{y_2} c(y)ydy$$

where τ is a function of the control surface chord ratio(c_f/c), $C_{L_\alpha} = 3.8$, and $y_1 = 0.15$ and $y_2 = 0.80$ determines the spanwise portion of the wing that has an aileron (see Figure 2-15). Equating $10.7\ [N \cdot m] = L_{aileron}$ gives

$$\tau\delta_a = 0.048$$

This leads to the following required control surface chord for a wing with $c = 77cm$.

δ_a	τ	c_f/c	$c_{f_{required}}$
5^o	0.55	0.35	> 27 cm
7^o	0.39	0.23	> 17 cm
10^o	0.27	0.15	> 12 cm

In the case of the yaw motion, the total moment about the reference point is composed of $N_{mini's\ drag}$, and $N_{mini's\ thrust}$. The value of the first term can be obtained as:

$$\begin{aligned}
N_{mini's\ drag} &= N_{due\ to\ induced\ drag} + N_{due\ to\ friction\ drag} \\
&= \frac{1}{2}\rho V^2 S_{ref} bC_{n_{ind}} + \frac{1}{2}\rho V^2 S_{mini}C_{D0} \cdot (moment\ arm) \\
&= 0.1 + 0.7 \\
&= 0.8\ [N \cdot m]
\end{aligned}$$

This value is small enough to be balanced by either the rudder deflection or the mini vehicle's engine throttle setting. To see the power required for the mini's engine,

$$\begin{aligned}
0.8\ [N \cdot m] &= T_{mini} \cdot (moment\ arm) \\
&= \frac{746\eta_p Hp}{V} \cdot (moment\ arm) \\
&\quad where,\ \eta_p : 0.7,\ V : 16m/s,\ moment\ arm : 1.4m. \\
\longrightarrow Hp &= 0.024,
\end{aligned}$$

which is within the operational range. It should be mentioned, however, that the static analysis described above does not guarantee dynamic stability.

2.3 Downselection of Integration Concept

The integration concepts were further studied and compared in the second year of the project for the final selection of the parent-mini integration. The team chose configuration shown in Figure 2-16 as a final integration concept for further development.

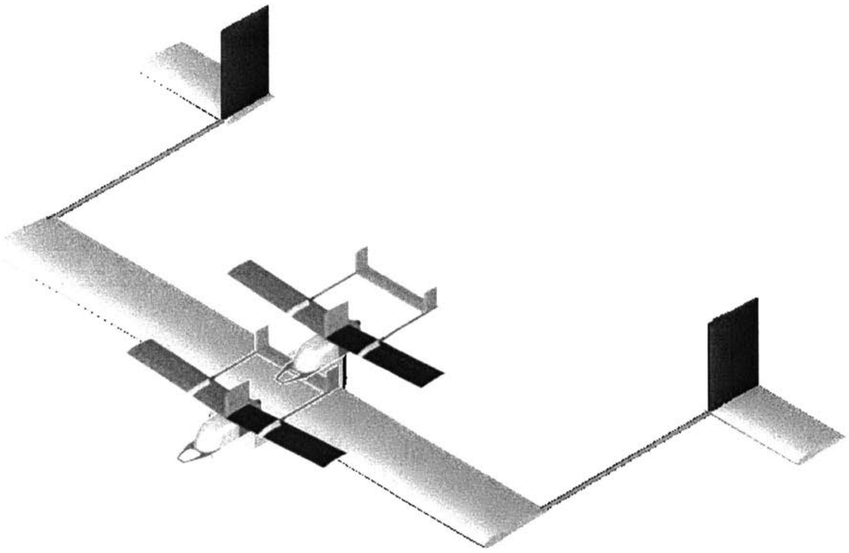

Figure 2-16: Parent-Mini Integration Concept for Further Development

The primary reason for this selection was the use of outboard horizontal stabilizer (OHS) configuration as a parent vehicle. The horizontal tails of the OHS aircraft are placed outboard of the main wing, so the vortex generated from the main wing gives upwash effect to the horizontal tail, which provides more efficiency and stability. In addition this tail location obviously provides clear room for reintegration with the mini vehicle.

Chapter 3

Reintegration Control System Development

3.1 Concept Development

The procedure for reintegration of the mini vehicle with the parent was divided into three phases, each with a corresponding control system. Figure 3-1 shows the phases: initially, the two vehicles are flying independently far away from each other. A series of waypoints are generated for both vehicles to follow in order to achieve a configuration where the two vehicles are flying parallel with each other, several meters apart as in the second picture in Figure 3-1. This segment of the procedure was named phase 1 of the reintegration. Phase 2 begins in this configuration, and ends when actual physical contact is made between the mini vehicle and an extra structure deployed by the parent vehicle, as shown in the third configuration in Figure 3-1. It was determined that this extra structure is required to make safe physical contact away from the main body of the parent vehicle, and to avoid turbulent air flow generated by the parent vehicle. The final step is to retrieve the mini vehicle onto the parent by folding the extra structure, which is phase 3.

Phase 1 of the reintegration can be achieved using conventional waypoint navigation with GPS. Therefore, the team's effort was first focused on phase 2 of reintegration, which is to make physical contact between the mini vehicle and a grabbing

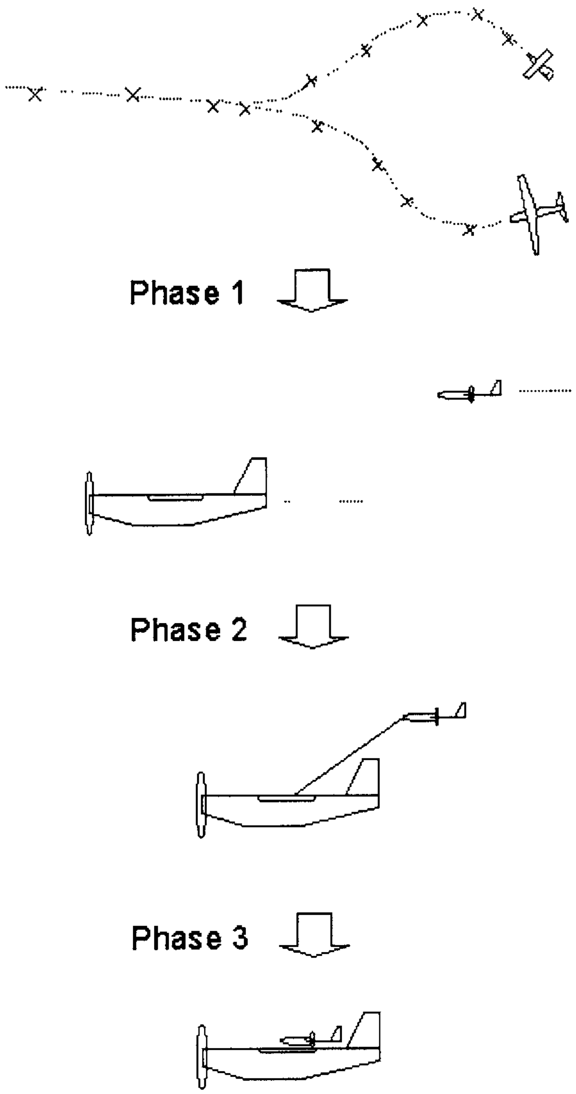

Figure 3-1: Reintegration Phases

mechanism on the parent vehicle. So the initial condition assumed in this problem consists of the mini vehicle approximately 10 meters behind the parent vehicle, with the assumption that differential GPS between the parent and mini would be used during phase 1 in the objective PCUAV system.

Sensor selection

In order to make physical contact in the air between a mini vehicle and a grabbing mechanism, an accurate sensor with error less than a few centimeters is required.

Various options for the position sensors were compared and the team decided to use a vision-based system. As is shown in Figure 3-2 (a), it requires a combination of two CCD cameras on the mini vehicle and a light source with distinctive color as a target on the parent. The target coordinates are obtained by comparing the target's pixel positions in the two CCD camera images. The exact same concept can be applied to an infrared system, in which two infrared cameras and a heat source are used instead of the optical sensor and a light source. The team decided to pursue the optical option. The development of the vision system is detailed in Chapter 4.

Control issues

Two options for control were compared. The first option is to give primary control responsibility to the parent. In other words, the controller would be implemented on the parent vehicle to catch the mini or the extra structure would be made maneuverable to catch the mini vehicle. But since the parent vehicle has more inertia than the mini, and making the extra structure maneuverable is a more complex problem both from the control viewpoint and mechanically, it was decided to give the maneuver responsibility to the mini vehicle. In other words the mini vehicle is controlled to actively follow and track a contact device on the parent vehicle. A contact mechanism, which is a combination of a grabber on the parent vehicle and a nose ring on the mini vehicle was devised, as shown in Figure 3-2. Also, as shown in Figure 3-2 (b), the mini vehicle has an unconventional control surface on top of the center of the fuselage to generate direct translational side force. The motivation is to minimize the attitude change when the vehicle tries to follow the target. Otherwise, the side position correction using conventional control surfaces would involve yaw and roll. The same idea is applied to vertical movement. The mini vehicle has large trailing edge flaperons to generate direct lift, which minimizes the pitch attitude change during altitude corrections.

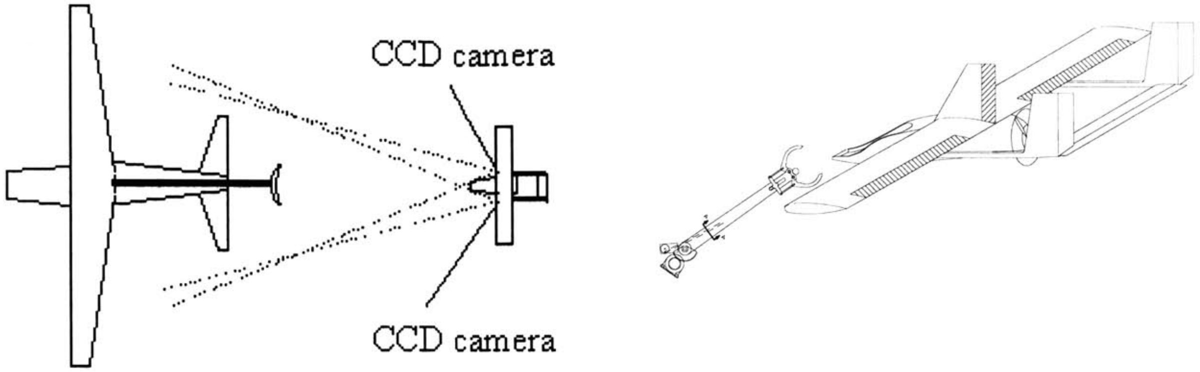

(a) Vision based positioning (b) grabber and direct force generators in mini

Figure 3-2: Features in control system for reintegration phase 2

3.2 Testbed Aircraft

Another vehicle was built for testing avionics and other aspects of the project such as a wireless networking. This vehicle was named the testbed aircraft. It is shown in Figure 3-3. The total weight of the testbed with all avionics is 5.5 kg. It uses an IC engine of size 0.60 cu. in. It is a modified version of the Hobbico Superstar 60 R/C airplane. Its fuselage section was enlarged from the original frame to accommodate an extensive avionics suite.

A position-hold control system was developed for this vehicle. The following sections describe the control system development for both the mini and the testbed aircraft.

3.3 Approach to Control System Development

First, the flight condition for reintegration was selected by comparing the speed ranges of the parent and the mini vehicle. This was done based on the power v.s. speed relation curves for the two vehicles. The process of getting these curves is described in Chapter 2. Using the Vortex lattice method, the following flight condition was

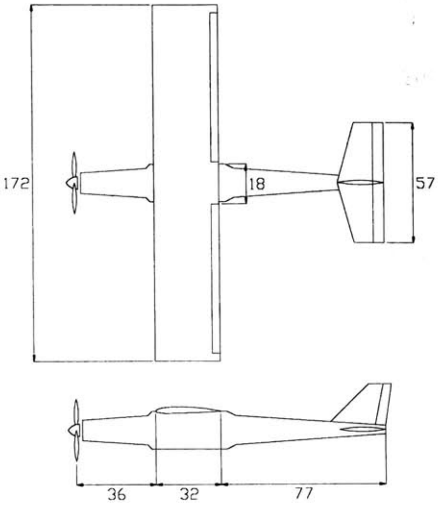

Figure 3-3: Geometry of Testbed Aircraft, unit[cm]

initially envisioned for the mini during reintegration.

$$V = 15.0\ m/s,\ \alpha = 5.4^o,\ C_L = 0.54,\ C_D = 0.043,\ T = 1.1[N]$$

For the testbed airplane, a 20 m/s flight speed was chosen, which is larger than that of the mini's because of the heavier weight. The flight condition for position hold tests using the testbed vehicle is

$$V = 20.0\ m/s,\ \alpha = 3.8^o,\ C_L = 0.37,\ C_D = 0.029,\ T = 3.9[N]$$

The two vehicles were modeled using 6 degree-of-freedom rigid body equations of motion [2]. Aerodynamic forces and moments were estimated around the proposed reintegration flight condition using AVL and wind tunnel data. A simulator was constructed in the Matlab Simulink environment. Then, the trim condition for reintegration was again derived using the model. A linear model was extracted around the flight condition. Then, a controller was designed and verified using the simulation.

The following sections describe the detail of the procedure for modeling, controller design, and simulation.

3.4 Modeling and Simulator Construction

This section enumerates the equations and formulas required for the simulator construction. Throughout this chapter, the notations δ_f and δ_s are used for the deflection angles for the flaperon and the sideways control surface. In the actual implementation for the deflection of the left flap and the right flap, δ_f and δ_a are superimposed. It should be noted that the procedure for control system development was done in parallel with the mini vehicle development. Thus, some of the numbers in this section could be different from those for the ultimate mini vehicle.

3.4.1 Geometric and Inertial Properties

The geometric and inertial data for the objective mini vehicle are:

mass : $m = 1.5\ kg$
wing area : $S = 0.264\ m^2$
wing span : $b = 1.4\ m$
mean aerodynamic chord : $\bar{c} = 0.176\ m$

$$\begin{array}{lll} J_x = 0.0592\ kgm^2 & J_y = 0.0455\ kgm^2 & J_z = 0.0991\ kgm^2 \\ J_{xz} = 0.00609\ kgm^2 & J_{xy} = 0\ kgm^2 & J_{yz} = 0\ kgm^2 \end{array}$$

The testbed aircraft has the following geometric and inertial properties:

mass : $m = 5.5\ kg$
wing area : $S = 0.55\ m^2$
wing span : $b = 1.72\ m$
mean aerodynamic chord : $\bar{c} = 0.32\ m$

$$\begin{array}{lll} J_x = 0.221\ kgm^2 & J_y = 0.462\ kgm^2 & J_z = 0.621\ kgm^2 \\ J_{xz} = 0.0086\ kgm^2 & J_{xy} = 0\ kgm^2 & J_{yz} = 0\ kgm^2 \end{array}$$

The moment of inertia of the testbed was estimated based on the pendulum setup shown in Figure 3-4 for each axis, with the corresponding relation

$$J_i = \frac{mgd^2T^2}{4l\pi^2}$$

where T is the measured period.

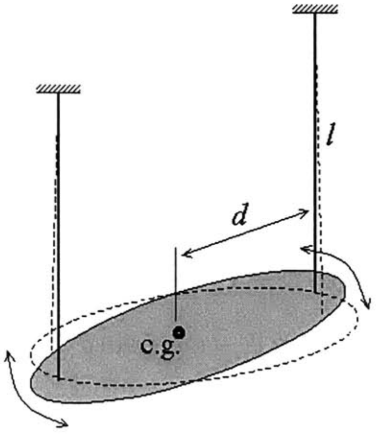

Figure 3-4: Pendulum setup for estimation of moment of inertia

3.4.2 Equations of Motion

The following standard, rigid body, 6-DOF equations of motion were used[2].

Force and Moment Equations :

$$\begin{aligned}
\dot{V}_T &= \frac{U\dot{U} + V\dot{V} + W\dot{W}}{V_T} \\
\dot{\beta} &= \frac{\dot{V}V_T - V\dot{V}_T}{V_T^2 \cos\beta} \\
\dot{\alpha} &= \frac{U\dot{W} - W\dot{U}}{U^2 + W^2} \\
\dot{P} &= (c_1 R + c_2 P)Q + c_3 \bar{L} + c_4 N \\
\dot{Q} &= c_5 PR - c_6(P^2 - R^2) + c_7 M \\
\dot{R} &= (c_8 P - c_2 R)Q + c_4 \bar{L} + c_9 N
\end{aligned}$$

where

$$\begin{aligned}
\dot{U} &= RV - QW - g\sin\theta + \frac{1}{m}(F_x + T_x) \\
\dot{V} &= PW - RU + g\cos\theta\sin\phi + \frac{1}{m}F_y \\
\dot{W} &= QU - PV + g\cos\theta\cos\phi + \frac{1}{m}(F_z + T_z)
\end{aligned}$$

Kinematic Equations :

$$
\begin{aligned}
\dot{\phi} &= P + \tan\theta(Q\sin\phi + R\cos\phi) \\
\dot{\theta} &= Q\cos\theta - R\sin\phi \\
\dot{\psi} &= \frac{Q\sin\phi + R\cos\phi}{\cos\theta}
\end{aligned}
$$

Navigation Equations :

$$
\begin{aligned}
\dot{p}_N &= U\cos\theta\cos\psi + V(-\cos\phi\sin\psi + \sin\phi\sin\theta\cos\psi) \\
&\quad + W(\sin\phi\sin\psi + \cos\phi\sin\theta\cos\psi) \\
\dot{p}_E &= U\cos\theta\sin\psi + V(\cos\phi\cos\psi + \sin\phi\sin\theta\sin\psi) \\
&\quad + W(-\sin\phi\cos\psi + \cos\phi\sin\theta\sin\psi) \\
\dot{h} &= U\sin\theta - V\sin\phi\cos\theta - W\cos\phi\cos\theta
\end{aligned}
$$

where the forces and moments with respect to the body axis are computed from those with respect to the stability axis by the relations:

$$
\begin{Bmatrix} F_x \\ F_y \\ F_z \end{Bmatrix} = \begin{bmatrix} \cos\alpha & 0 & -\sin\alpha \\ 0 & 1 & 0 \\ \sin\alpha & 0 & \cos\alpha \end{bmatrix} \begin{Bmatrix} F_{x_s} \\ F_{y_s} \\ F_{z_s} \end{Bmatrix}, \quad \begin{Bmatrix} \bar{L} \\ M \\ N \end{Bmatrix} = \begin{bmatrix} \cos\alpha & 0 & -\sin\alpha \\ 0 & 1 & 0 \\ \sin\alpha & 0 & \cos\alpha \end{bmatrix} \begin{Bmatrix} \bar{L}_s \\ M_s \\ N_s \end{Bmatrix}
$$

where

$$
\begin{aligned}
F_{x_s} &= C_{x_s}\bar{q}S & \qquad \bar{L}_s &= C_{l_s}\bar{q}Sb \\
F_{y_s} &= C_{y_s}\bar{q}S & \qquad M_s &= C_{m_s}\bar{q}S\bar{c} \\
F_{z_s} &= C_{z_s}\bar{q}S & \qquad N_s &= C_{n_s}\bar{q}Sb
\end{aligned}
$$

and where the aerodynamic coefficients about the stability axes were obtained either from the AVL method or from wind tunnel tests. These coefficients are described in the following sections.

The constants c_1 through c_9 are determined by the inertial properties of the vehicle by the relations:

$$
\begin{aligned}
&\Gamma = J_x J_z - J_{xz}^2, & &c_1 = \tfrac{(J_y - J_z)J_z - J_{xz}^2}{\Gamma} \\
&c_2 = \tfrac{(J_x - J_y + J_z)}{\Gamma}, & &c_3 = \tfrac{J_z}{\Gamma} \\
&c_4 = \tfrac{J_{xz}}{\Gamma}, & &c_5 = \tfrac{J_z - J_x}{J_y} \\
&c_6 = \tfrac{J_{xz}}{J_y}, & &c_7 = \tfrac{1}{J_y} \\
&c_8 = \tfrac{J_x(J_x - J_y) + J_{xz}^2}{\Gamma}, & &c_9 = \tfrac{J_x}{\Gamma}
\end{aligned}
$$

Finally, the coordinates of the nose position are found by

$$\begin{aligned}
X_{nose} &= p_N + l_x \cos\psi \cos\theta + l_z \cos\psi \sin\theta \\
Y_{nose} &= p_E + l_x \sin\psi \cos\theta + l_z \sin\psi \sin\theta \\
H_{nose} &= h + l_x \sin\theta - l_z \cos\theta
\end{aligned}$$

where l_x and l_z are distances in x and y directions from the c.g. to the nose ring position.

3.4.3 Aerodynamic Forces and Moments

The coefficients of aerodynamic forces and moments with respect to the stability axis were estimated by linearly summing up all the contributions.

$$\begin{aligned}
C_{x_s} &= -C_D \\
C_{y_s} &= C_{y_\beta}\beta + C_{y_p}\tfrac{P_s b}{2V_T} + C_{y_r}\tfrac{R_s b}{2V_T} + C_{y_{\delta_r}}\delta_r + C_{y_{\delta_s}}\delta_s \\
C_{z_s} &= -C_L \\
C_{l_s} &= C_{l_\beta}\beta + C_{l_p}\tfrac{P_s b}{2V_T} + C_{l_r}\tfrac{R_s b}{2V_T} + C_{l_{\delta_a}}\delta_a + C_{l_{\delta_s}}\delta_s \\
C_{m_s} &= C_{m_0} + C_{m_\alpha}\alpha + C_{m_q}\tfrac{Q_s \bar{c}}{2V_T} + C_{m_{\delta_e}}\delta_e + C_L(X_{cg} - X_{ref}) + C_{m_{\delta_f}}\delta f \\
C_{n_s} &= C_{n_\beta}\beta + C_{n_p}\tfrac{P_s b}{2V_T} + C_{n_{\delta_r}}\delta_r + C_{n_{\delta_a}}\delta_a + C_{n_{\delta_s}}\delta_s
\end{aligned}$$

where

$$\begin{aligned}
P_s &= P\cos\alpha + R\sin\alpha \\
Q_s &= Q \\
R_s &= -P\sin\alpha + R\cos\alpha
\end{aligned}$$

and

$$\begin{aligned}
C_L &= C_{L_0} + C_{L_\alpha}\alpha + C_{L_q}\tfrac{Q_s \bar{c}}{2V_T} + C_{L_{\delta_e}}\delta_e + C_{L_{\delta_f}}\delta_f \\
C_D &= C_D(\alpha, \delta_f)
\end{aligned}$$

where the effect of α and δ_f on C_D were separately computed with second order polynomial approximations obtained in AVL and added together. It should be noted that the effect of the flaperon(δ_f) and sideways control surface(δ_s) deflections are also added into the equations.

The coefficients required to compute the aerodynamic forces and moments were obtained in AVL as linearizations around the proposed reintegration flight condition.

The control derivatives were also estimated in AVL by deflecting control surfaces in the AVL model. Static derivatives and control derivatives were also obtained from the wind tunnel data. These aerodynamic coefficients are summarized in Table 3.1 for Mini vehicle and in Table 3.2 for the testbed aircraft.

C_{Lo}	C_{Mo}	C_{L_α}	C_{M_α}	C_{y_β}	C_{l_β}	C_{n_β}	C_{y_p}	C_{l_p}
0.0278	0.008	5.45	−1.10	−0.645	−0.0279	0.0576	0.0232	−0.541
		5.96	−1.17	−0.885	−0.0755	0.0870		

C_{n_p}	C_{L_q}	C_{M_q}	C_{y_r}	C_{l_r}	C_{n_r}	$C_{M_{\delta_e}}$	$C_{L_{\delta_e}}$	$C_{y_{\delta_r}}$
−0.0396	9.98	−12.9	0.236	0.146	−0.064	−1.65	0.745	0.183
						−1.2	0.20	0.206

$C_{n_{\delta_r}}$	$C_{L_{\delta_f}}$	$C_{M_{\delta_f}}$	$C_{y_{\delta_s}}$	$C_{n_{\delta_s}}$	$C_{l_{\delta_a}}$	$C_{n_{\delta_a}}$	$C_{l_{\delta_s}}$
−0.063	2.06	−0.183	0.183	0.000	−0.458	0.0057	−0.0057
−0.061	1.73	−0.120	0.110	0.000	−0.231	0.000	−0.003

Table 3.1: Aerodynamic Characteristics of Mini (reference : 5cm from L.E.)
(Note: *The numbers in the upper row represent the AVL results, and the bottom is for the wind tunnel data.*)

It should be noted that C_{l_β} using wind tunnel data is greater than that in the AVL model. This is because of the high wing effect. The fuselage section was not modeled in an AVL. Another point is that the control surface effectiveness is in general oversized in the AVL model. That is mainly because the airfoil thickness is not considered in AVL. Also, because of the effect of the wake behind the fuselage, the coefficients for the elevator deflection are significantly less in the wind tunnel data than in AVL methods, where the fuselage is not modeled. The effectiveness of the sideways control surface is also smaller in the wind tunnel than in the AVL model, which is again likely to be due to the fuselage effect.

In the controller design for the Mini in Section 3.6, the wind tunnel data was used. For the testbed vehicle, controller design, the control surface capabilities were

C_{Lo}	C_{Mo}	$C_{L\alpha}$	$C_{M\alpha}$	$C_{y\beta}$	C_{l_β}	C_{n_β}	C_{y_p}	C_{l_p}
0.0991	0.0270	4.54	−1.11	−0.211	−0.0074	0.0959	−0.0399	−0.430
C_{n_p}	C_{L_q}	C_{M_q}	C_{y_r}	C_{l_r}	C_{n_r}	$C_{M_{\delta_e}}$	$C_{L_{\delta_e}}$	$C_{y_{\delta_r}}$
−0.0419	8.272	−11.1	0.258	0.126	−0.125	−1.16	0.401	0.118
$C_{n_{\delta_r}}$	$C_{L_{\delta_f}}$	$C_{M_{\delta_f}}$	$C_{l_{\delta_a}}$	$C_{n_{\delta_a}}$				
−0.063	1.48	−0.300	−0.301	0.052				

Table 3.2: Aerodynamic Characteristics of Testbed Aircraft (reference: 1/4 $\bar{c}$)
(Note: *The numbers represent AVL results.*)

adjusted based on the comparison of the wind tunnel and AVL results for the Mini vehicle.

3.4.4 Actuator Modeling

This section describes analyses and tests of the major actuation devices, namely control surface servos and the engine/propeller combination. Because it is slender and can be mounted inside the airfoils, a Volz "Wing-Star" servo motor was chosen for the control surface actuation in the mini vehicle. The following table summarizes the specifications for the servo motor, as provided by Volz.

Weight	19g
Volume	30 × 49 × 10 (mm)
Voltage	4.8/6.0 [V]
Torque	1.8 kg-cm (42 oz.in=0.18 N-m)
Speed	270 deg/sec (4.76 rad/sec)
Range	2 × 45 degree

A Frequency response test was done. The reference signal produced by a function generator and the output of the servo motor measured by a potentiometer were compared on an oscilloscope. The RC servo motor is actuated by a series of pulses as an input. The pulse is sent to the servo every 10 ms. The pulse width is typically between 0.5~2.0 ms, the interval of which determines the desired deflection angle of the servo motor. The conversion of the sinusoidal signal from the function generator into pulses was implemented using a Borland C program with PC interface.

The magnitude of the load on the servo motor during flight was estimated assuming that the control surface is a flat plate. Then the torque exerted on the servo motor was obtained as a function of control surface deflection angle, airspeed, and the ratio of deflection angles between the servo and the control surface. The torque required on the servo motor to sustain 5 degrees of deflection on the flaperon was estimated to be 0.02 N·m (=200 g·cm), when the deflection ratio of the control surface and the servo motor set to 1/2. Experiments with several loading conditions showed that the response of the servo motor doesn't change significantly up to the load condition of 350 g·cm.

Figure 3-5 shows the frequency response of the servo motor. Several choices of the reference deflection angles were tried. The *'s and +'s are for $\pm 45^o$ and $\pm 20^o$ deflection inputs respectively. The solid line is for the 1st order lag with a time constant of 1/15 second. The result indicates that the cutoff frequency that the magnitude begins to fall depends on the range of deflection in the reference input. This is because there is a slew rate limitation in the servo motor. If the input frequency is such that it requires faster speed than this limit, then this is the point where the phase delay and magnitude decrease begin to take place. This frequency can also be estimated if the speed limitation is known. For the frequency range less than this frequency, the output angle is an undistorted sinusoid, which can be expressed as:

$$\delta = A \sin \omega t \qquad \text{so} \qquad \dot{\delta} = A\omega \cos \omega t$$

Since the maximum of $\dot{\delta}$ is limited, the critical frequency where the servo begins to reach its maximum speed is

$$\omega_{cr} = \frac{\dot{\delta}_{limit}}{A}$$

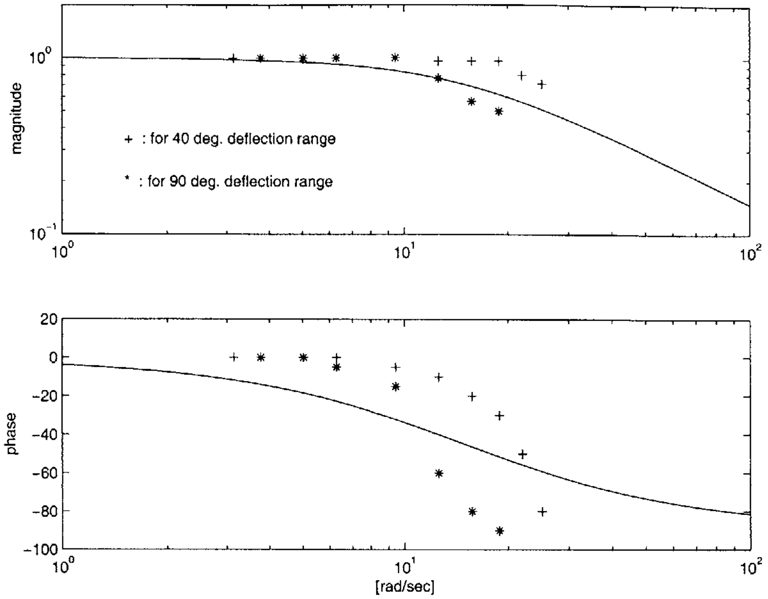

Figure 3-5: Frequency response of servo motor

where A is the amplitude of deflection. The speed limitation measured in this experiment is 330 degree/sec. When A is 45^o and 20^o, ω_{cr}=7.4 rad/sec(1.2Hz) and 16.5 rad/sec(2.6Hz) respectively.

Based on the experiment, the controller was designed using a first order filter with a cutoff frequency of 15 rad/sec. Simulations were performed with an actuator model with the slew rate limit quoted above. The controller design and simulation are described in the following sections.

The engine/propeller system is also used as an actuator for controlling motions in aircraft X direction. The engine thrust was modeled by the simple static relation

$$T = \frac{power \times \eta_p}{V_T}$$

for the mini vehicle where η_p is the propeller efficiency and the power setting is the input variable, assuming that during the reintegration there is no rapid change of the throttle setting and the thrust time constant is also much lower than that of the engine controller for the forward position hold.

For the testbed airplane, a 0.60 cu. in. internal combustion engine and 12-6 propeller were used. The thrust is estimated by

$$T = T_{static} + K \cdot V_T$$

where the equation

$$T_{static} = -5.815\ pow^3 + 7.412\ pow^2 + 1.17\ pow + 0.416\ [kg]$$

was obtained from the static thrust tests, and where *pow* is the power setting between 0.0~1.0. and

$$K = K_o \frac{T_{static}}{(T_{static})_{max}}$$

where $(T_{static})_{max} = 3.1\ [kg]$ and $K_o = -0.0671\ [kg \cdot sec/m]$

3.4.5 Gust Modeling

Air turbulence velocities(U_g, V_g, W_g) in the x,y,z directions, respectively, can cause the aerodynamic forces and moments. Here, the changes of total velocity, angle of attack, and sideslip angle were considered in the model with the following relations [7]:

$$V_T = \sqrt{(U - U_g)^2 + (V - V_g)^2 + (W - W_g)^2}$$
$$\alpha_A = \alpha + \alpha_g$$
$$\beta_A = \beta + \beta_g$$

where

$$\alpha_g = -\frac{W_g}{U_1}, \quad \beta_g = \frac{V_g}{U_1}$$

and U_1 is the steady state velocity component in the x direction. These expressions for V_T, α_A, β_A are used for the computation of the aerodynamic forces and moments, as described in Section 3.4.3. Because these quantities are induced by relative wind rather than the motion of the vehicle, they shouldn't be applied directly to the inertial terms in the differential equations described in Section 3.4.2.

For the computation of the gust velocities, U_g, V_g, W_g, the Dryden gust model was used, where the power spectra are given as:

$$\begin{aligned}
\Phi_{u_g}(\omega) &= \sigma_u^2 \tfrac{2L_u}{\pi} \tfrac{1}{1+(L_u\omega)^2} \\
\Phi_{v_g}(\omega) &= \sigma_v^2 \tfrac{L_v}{\pi} \tfrac{1}{1+3(L_v\omega)^2} \\
\Phi_{w_g}(\omega) &= \sigma_w^2 \tfrac{L_w}{\pi} \tfrac{1}{1+3(L_w\omega)^2}
\end{aligned}$$

where

$$\sigma_u^2 = \frac{L_u}{L_w}\sigma_w^2, \sigma_v^2 = \frac{L_v}{L_w}\sigma_w^2$$

and

$$L_u = 145h^{1/3}, L_v = 145h^{1/3}, L_w = h$$

where h is the altitude in [ft] and σ^2 is a function of altitude given in [7].

Finally, corresponding shaping filters were found from the power spectra to generate the gust velocities for the simulation from white noise sequences created in a digital computer.

3.5 Trim Analysis and Linearization

The non-linear 6-DOF model was built based on the equations described in the previous sections using the Matlab simulink environment. A steady state trimmed flight condition was then found from the non-linear model using the Matlab optimization toolbox function 'fminsearch'. The Steady-state translation flight condition, which is the reintegration condition for the mini vehicle, can be imposed in the model by the relations:

$V_T = 15\ m/s$: as proposed from the power-speed curves

$\theta = \alpha$: specified for level-flight with γ=0.

$\phi = 0, P = 0, Q = 0, R = 0$: steady-state level

$\delta_f = 0, \delta_s = 0$: flaperon and sideway control surface are not used to trim the aircraft for the steady-state level flight.

The function

$$cost = \dot{V_T}^2 + 100(\dot{\alpha}^2 + \dot{\beta}^2) + 10(\dot{P}^2 + \dot{Q}^2 + \dot{R}^2)$$

was chosen as cost to be minimized in the 'fminsearch', while 100 and 10 are multiplied as weighting factors for faster numerical results. The following trim conditions were found from the algorithm

$$V_T = 15\ m/s,\ \alpha = 5.74^o,\ \delta_e = -3.55^o,\ power = 24.8\ [W],\ \beta, \delta_r, \delta_a \approx 0$$

for the Mini and

$$V_T = 20\ m/s,\ \alpha = 3.9^o,\ \delta_e = -4.84^o,\ power\ setting = 0.21,\ \beta, \delta_r, \delta_a \approx 0$$

for the testbed.

A linear model was then numerically extracted around the trim condition. The Matlab function 'linmod' was used for this, where the nonlinear simulink model and the steady state conditions are imposed for this function. The output of the function, in state space form, showed that the longitudinal and lateral modes are decoupled. The corresponding transfer functions were then obtained. Some of the numerically derived transfer functions for the elevator input were checked by comparing these with analytical approximations. Table 3.3 and 3.4 summarize the longitudinal and lateral mode properties for Mini and the testbed aircraft.

	eigenvalues	descriptions
longitudinal	-9.49±11.83i	short period : ω_{n_s}=15.2 rad/s(=2.42 Hz), ζ_s=0.63
	-0.0728±0.748i	phugoid : ω_{n_p}=0.75 rad/s(=0.12 Hz), ζ_p=0.0968
lateral	-20.5	roll mode
	-1.37±6.78i	dutch roll : ω_{n_d}=6.92 rad/s(=1.1 Hz), ζ_d=0.20)
	0.0946	spiral

Table 3.3: Mode Characteristics : Mini

3.6 Controller Design for the Mini

It was postulated that the proper way to achieve phase 2 of the reintegration task is to make the mini vehicle approach the parent along a straight line rather slowly, while

	eigenvalues	descriptions
longitudinal	-6.95±9.65i	short period : ω_{n_s}=11.9 rad/s(=1.89 Hz), ζ_s=0.58
	-0.0329±0.590i	phugoid : ω_{n_p}=0.59 rad/s(=0.093 Hz), ζ_p=0.056
lateral	-19.3	roll mode
	-1.264±6.02i	dutch roll : ω_{n_d}=6.14 rad/s(=0.978 Hz), ζ_d=0.21)
	0.108	spiral

Table 3.4: Mode Characteristics : Testbed Aircraft

correcting vertical and sideways position errors rather quickly, and finally correcting attitude errors most quickly. Thus, the following was considered as a basic approach for the controller design:

1. Use conventional control surfaces (δ_e, δ_r) to add damping to the fast vehicle modes, if necessary. It was found that
   - Yaw damper is required to improve dutch roll mode (ζ = 0.20, ω_n=6.92 rad/sec = 1.1 Hz)
   - The short period damping is naturally good enough (ζ = 0.63, ω_n=15.2 rad/sec = 2.4 Hz)
2. Use conventional control surfaces(δ_a) to provide the attitude hold function
   - bank attitude hold
3. Use conventional control surfaces, flaperon, and sideways control surfaces to provide translational position hold.
   - vertical position hold
   - sideways position hold
4. Finally, adjust the power setting for the engine to move slowly toward the target point
   - forward position hold

The performance of the attitude and position sensors were considered as constraints in the design of the controller, which are:

- The sampling frequency of the rate gyro is around 80 Hz.
- The sampling frequency of the framegrabber is around 10 Hz.

Thus, the corresponding crossover frequencies in the controller were limited to be no more than 1/10th of the sensor bandwidths.

The detailed procedures for the controller design for each mode are described in the following subsections, but they can be summarize, here, by the two block diagrams in Figure 3-6 and Table 3.5.

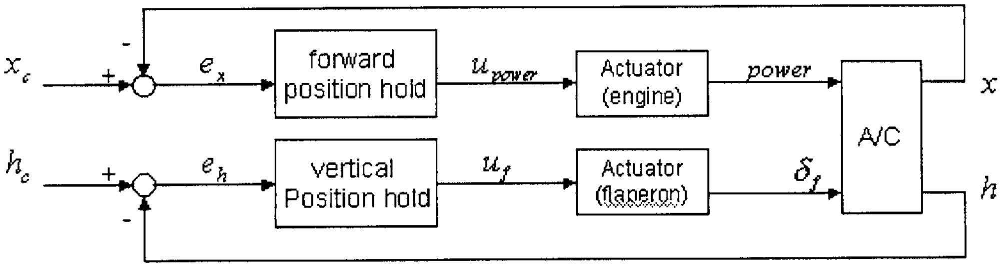

(a) Longtitudinal control

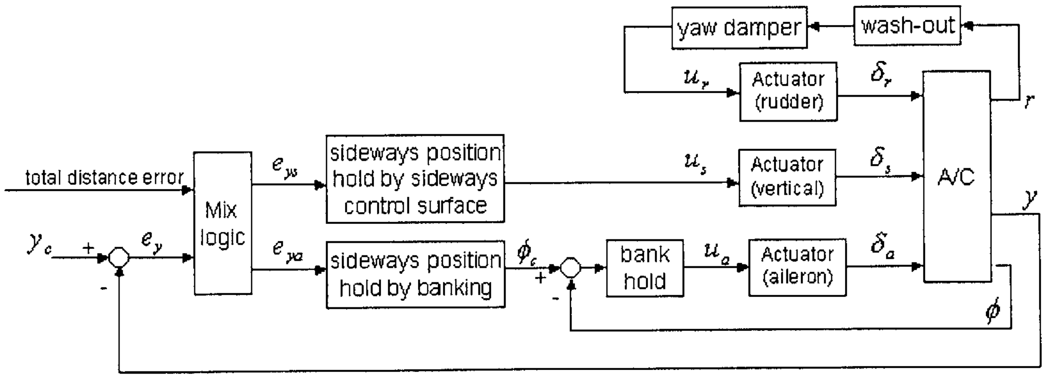

(b) Lateral control

Figure 3-6: Controller Block Diagrams : Mini

As is shown in Table 3.5, what is important in this controller architecture is to impose the bandwidths of the compensators in proper ways. For example, the cross-

	compensator	cross-over [rad/s]	phase margin
vertical position hold	lead-lag	4.0	59
forward position hold	lead-lag	1.0	64
yaw damper	proportional	dominant poles :	-5.88±10.33i
bank hold	lead-lag	15.0	69
sideways position hold(banking)	lead-lag	1.0	49
sideways position hold(δ_s)	lead-lag	2.0	54

Table 3.5: Summary of Controllers : Mini

over frequencies of the vertical and forward position holds are separated by a factor of four, since the forward speed change affects the vertical movement. Similarly, an inner loop controller, such as bank hold, is made faster than the outer loop sideways position holds by factors of 7.5 and 15.

Diagram (a) shows the longitudinal control, where the ultimate purpose is to correct the altitude and the forward distance differences. The main feature of this longitudinal control is the use of flaperon alone to correct the altitude error. This is possible because the Mini has a relatively short chord. Its aspect ratio(AR) is 9.0. However, as described in Section 3.9, the testbed aircraft, which has a lower AR of 5.4, the deflection of flaperon involves larger pitching moment. In this case, some compensating moment should be generated from elevator deflection (refer to Section 3.9). Using these features the conventional way of controlling altitude, where reference pitch angle is imposed to correct the altitude is avoided, thus negating the need for pitch angle estimation.

In the case of lateral control, which is shown in diagram (b), a combination of sideways control surface and aileron is used to correct the lateral position error. When the total distance between the mini vehicle and the target point is larger than three meters, the controller banks the vehicle to correct the sideways position error. When the distance is less than one meter, only the sideways control surface is used. In the case where the distance is between one and three meters, a combination of these two control surfaces is used.

Another feature of the controller design is that there is no pitch or yaw hold to certain fixed angles. In the early stage of the controller design, they were included in the controller. In the presence of disturbances, this attitude controller would tend to hold the pitch angle (or yaw angle) constant. This rigidity in attitude would prohibit any weathercocking tendency to nose the vehicle into the wind.[4] As a consequence, when the control power of the aircraft is not large enough to overcome the gust, it is better to release these controls.

The simulation, with constant gust speed, showed that for sideways gusts, the mini vehicle converges to the target with gust speeds up to 3.0 m/s with these two features in the controller (i.e. combination of control surfaces and removal of pitch/yaw attitude hold to fixed angle), while it converges with gust speed only up to 0.8 m/s when the weathercocking tendency is suppressed. For vertical gusts, the maximum gust speed that the mini can sustain improves from 0.4 m/s to 2.0 m/s. The following subsections describe the procedure followed in the design of each controller.

Vertical Position Hold by Flaperon

The transfer function from the flaperon deflection to the vertical position, with a first order lag actuator with cut-off at 15.0 rad/sec, is

$$\frac{h(s)}{\delta_f(s)} = \frac{494(s+7.10 \pm 8.18i)(s+0.0864)}{(s+15.0)(s+9.49 \pm 11.8i)(s+0.0728 \pm 0.748i)}$$

Bode design methods were used for the controller design. Figure 3-7 shows the open-loop (without compensator) and closed-loop (with compensator) Bode plots.

The lead-lag compensator

$$D(s) = 0.173 \left(\frac{2.5s+1}{2.5s}\right) \left(\frac{29.9 \times 0.0457s+1}{0.0457s+1}\right)$$

gives a crossover frequency at 4.02 rad/sec, and a phase margin of 59^o. It is desirable to have a phase margin as high as possible because there may be significant phase delay in the implementation of the vision based positioning sensor. The lag zero was placed at 1/10th of the cross-over frequency, ω_{co}. Figure 3-8 shows time responses to ±1 meter vertical position step inputs.

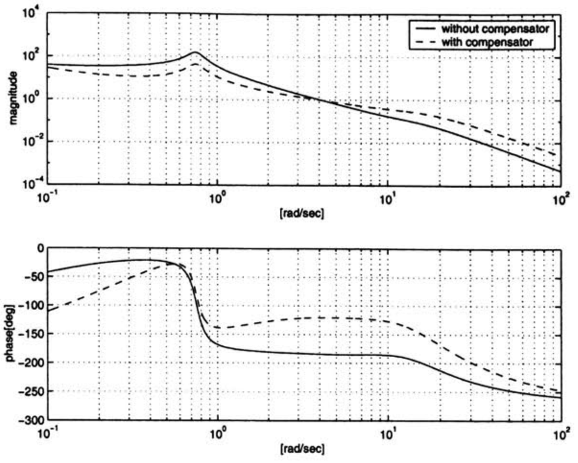

Figure 3-7: Bode plot for vertical position hold by flaperon

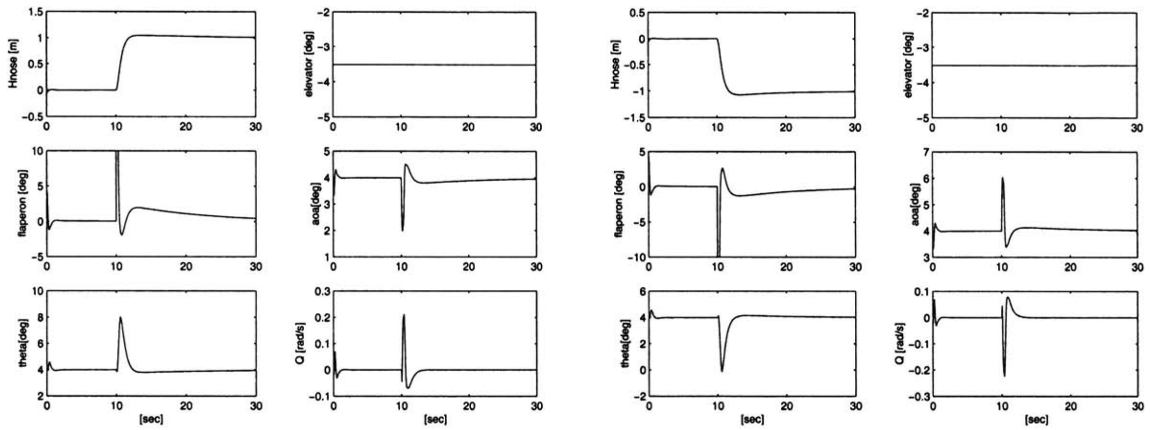

(a) + 1m reference

(b) - 1m reference

Figure 3-8: Time responses to ±1 meter step reference for vertical position

Forward position hold

For the forward position control function, thrust is the main control actuation mechanism. The design starts with the vehicle dynamics where the effect of the vertical position hold loop is included. A linear model with the vertical position hold controller was separately constructed in Matlab Simulink. Using the Matlab function 'linmod', the transfer function from the motor power to the forward position (x) was obtained as:

$$\frac{x(s)}{power(s)} = \frac{0.031(s+1.29)(s+0.365)}{s(s+1.69)(s+0.272)(s+0.0925)}$$

With the same actuator model for the servo motor, the following lead-lag compensator:

$$D(s) = 7.48\left(\frac{10s+1}{10s}\right)\left(\frac{23.4 \times 0.207s+1}{0.207s+1}\right)$$

gives ω_{co} of 1.0 rad/sec and PM of 64^o. The crossover frequency of this controller is chosen relatively slow. The corresponding open-loop and close-loop bode plots are shown in Figure 3-9.

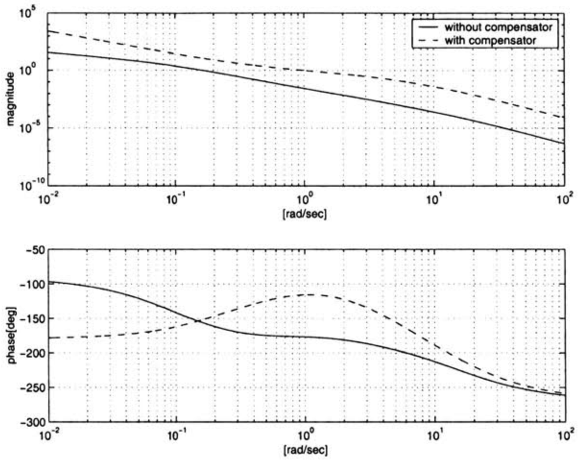

Figure 3-9: Bode plot for forward position hold

Figure 3-10 shows the simulation of this controller with 10 meters of initial position difference.

Simulation with initial velocity errors was also performed. Figure 3-11 (a) and (b) show the simulation with the relative velocity differences, where the mini vehicle speed is initially at 15 m/s while the parent vehicle is set to 16 m/s and 14 m/s respectively.

Yaw damper

The first step in creating the lateral controller is to provide yaw damping because dutch roll damping ($\zeta = 0.20$) needs to be improved. First, by looking at the transfer function from aileron(δ_a) to the roll rate(p),

$$\frac{p(s)}{\delta_a(s)} = \frac{-186(s-0.0442)(s+1.43 \pm 6.39i)}{(s+20.5)(s-0.0946)(s+1.37 \pm 6.78i)}$$

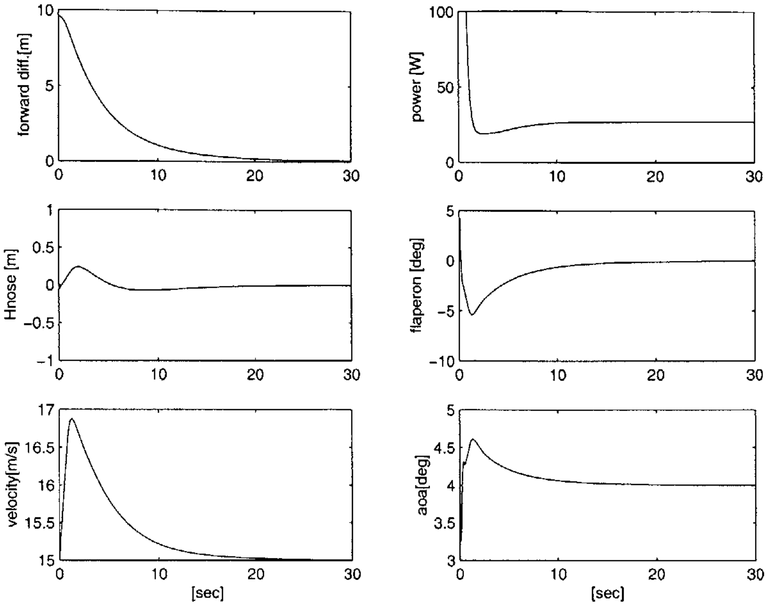

Figure 3-10: Simulation of forward position hold controller

it is noticed that the dutch roll poles nearly cancel with complex zeros, which means there is little coupling from the aileron input to the dutch roll. Thus, in order to improve dutch roll damping, only the rudder input needs to be considered. The transfer function from rudder deflection(δ_r) to yaw rate(r) is found to be

$$\frac{r(s)}{\delta_r(s)} = \frac{-29.1(s+20.7)(s+0.49\pm 1.30i)}{(s+20.5)(s-0.0946)(s+1.37\pm 6.78i)}$$

Cascading this transfer function with the same servo-motor actuator model, the root locus is plotted in Figure 3-12. The gain(K_r) was chosen to give the maximum damping ratio to the dutch roll mode. With $K_r = -0.28$, the poles are:

$$-20.6, -5.88 \pm 10.3i, -5.53, -0.216$$

These values are shown as stars in Figure 3-12.

Figure 3-13 shows the time response of the yaw rate (r) to a doublet in rudder input($\pm 1^o$) during t=5~7 [sec].

Bank angle hold

Bank hold is required for following bank angle commands, ultimately to control lateral position. Thus, it serves as an inner loop for the sideways position hold autopilot. The

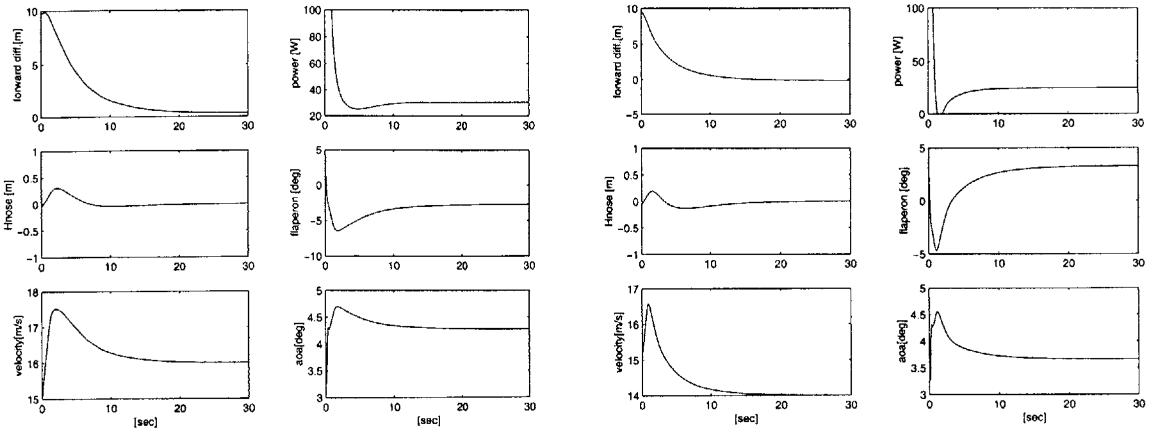

(a) with parent speed 16 m/s

(b) with parent speed 14 m/s

Figure 3-11: Simulation of forward position controller with velocity differences

transfer function from aileron deflection(δ_a) to bank angle(ϕ), including the modified dynamics due to the addition of the yaw damper and wash-out circuit with cut-off at 1.0 rad/sec, is found to be

$$\frac{\phi(s)}{\delta_a(s)} = \frac{-188(s + 6.77 \pm 10.1i)(s + 4.18)(s + 1.03)}{(s + 20.6)(s + 6.45 \pm 10.38i)(s + 4.16)(s + 1.51)(s + 0.0717)}$$

As will be shown in the simulation of this controller, wash-out of the yaw rate is required to allow intentional slow rate turns of the aircraft. Here, considering the dynamics of the yaw damper controller, the bandwidth was chosen to be 1.0 rad/sec, which is less than 1/10th of the yaw damper bandwidth.

Cascading this transfer function with the same actuator model of the servo motor, the lead-lag compensator

$$D(s) = 0.802 \left(\frac{0.667s + 1}{0.667s}\right) \left(\frac{8.05 \times 0.0235s + 1}{0.0235s + 1}\right)$$

gives a cross-over frequency of 15.1 rad/sec and a phase margin of 68^o. Figure 3-14 shows the open-loop and closed-loop bode plots.

Figure 3-15 shows the simulation result of step reference bank angle input of 10^o. The lead compensator was placed in the feedback path in the bank angle hold implementation. Lead in the feedback path usually prevents a sudden large change of actuator input. So it reduces the overshoot but slightly increases the rise time. This feature is obvious in the simulation result in Figure 3-15.

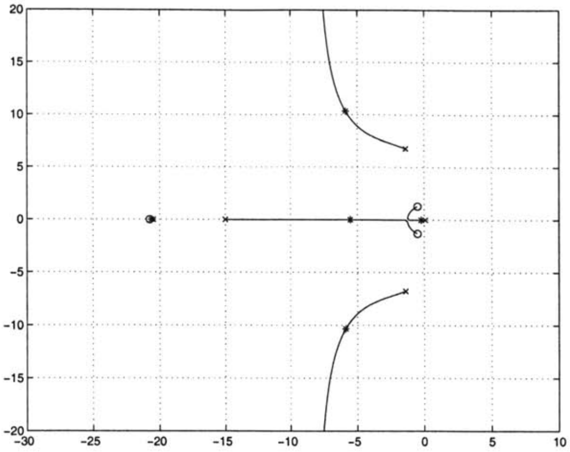

Figure 3-12: Root locus for yaw damper($*$: closed-loop pole locations for design point gain, K_r=-0.28)

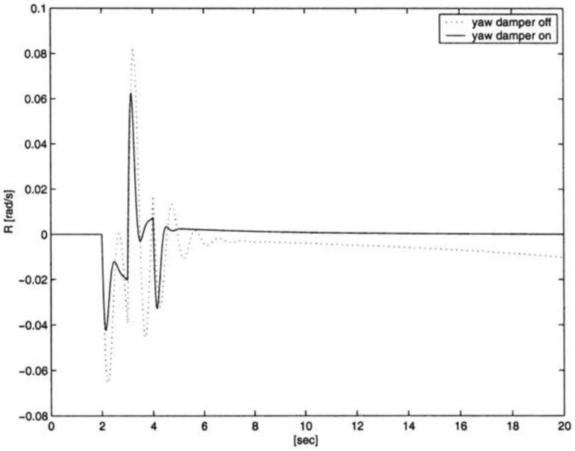

Figure 3-13: Rudder doublet response with and without yaw damper

As was mentioned in this subsection, after the transition due to the wash-out, the rudder doesn't try to resist the steady turning rate.

Lateral Position Hold using Aileron

The design of the controller for the sideways position autopilot starts with the dynamics that result from closing the yaw damper and the bank angle hold loops. The corresponding transfer function, from the bank angle as a reference input to the side-

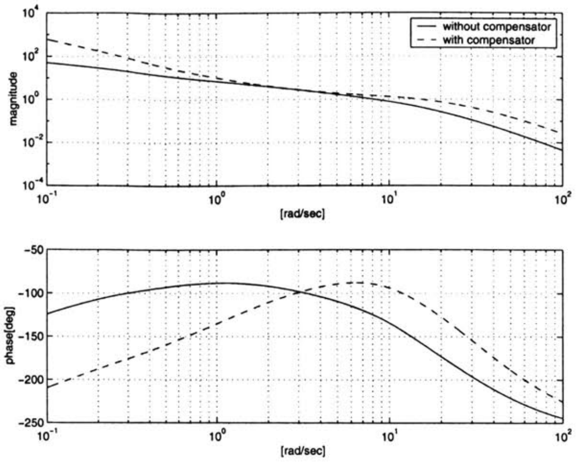

Figure 3-14: Bode plot for bank hold autopilot

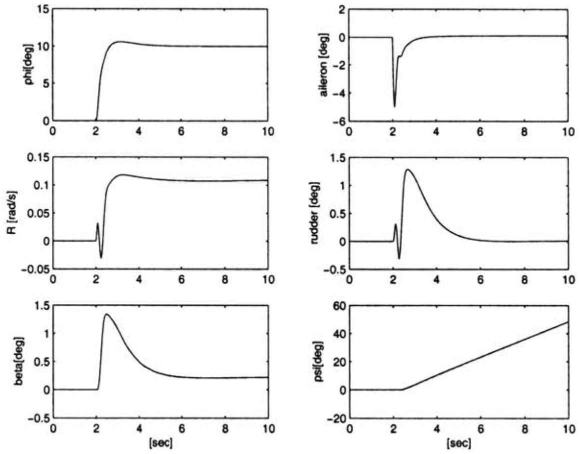

Figure 3-15: Time response to 10^o step reference input for bank hold

ways position, is found to be:

$$\frac{y(s)}{\phi_{ref}(s)} = \frac{90(s+43)(s+4.9\pm15.5i)(s+7.5\pm6.9i)(s+4.1)(s+1.5)(s+1.35)}{s^2(s+54)(s+9.1\pm18.7i)(s+7.0\pm10.3i)(s+4.2)(s+3.1)(s+1.45)(s+1.34)}$$

The controller was designed using Bode design methods and the results are shown in Figure 3-16. The lead-lag compensator:

$$D(s) = 0.0147\left(\frac{10s+1}{10s}\right)\left(\frac{58.0\times0.131s+1}{0.131s+1}\right)$$

gives a crossover at 1.0 rad/sec and a phase margin of 49^o.

Figure 3-17 shows the simulation result of a step reference input of 1 meter in sideways position.

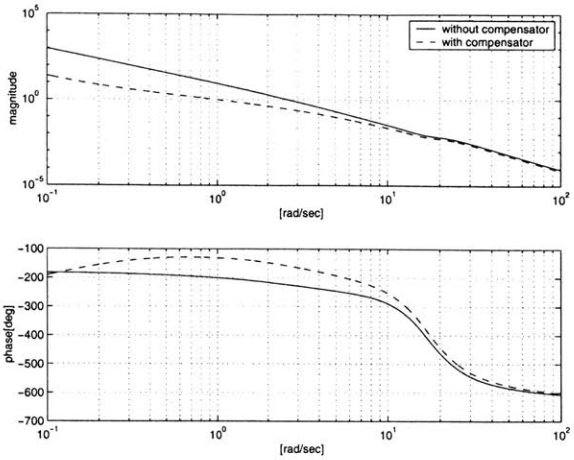

Figure 3-16: Bode plots for sideways position hold by aileron

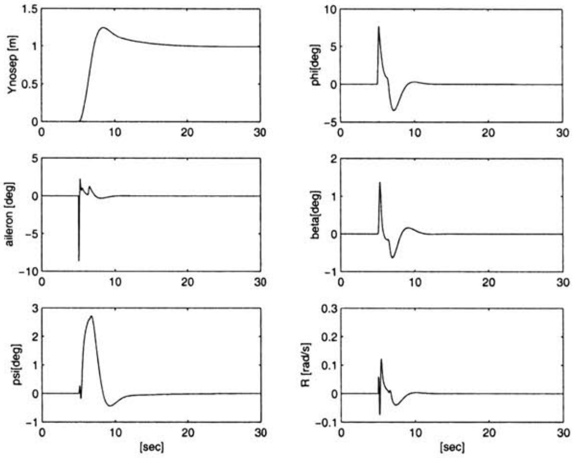

Figure 3-17: Time response to 1 meter step reference input for lateral position hold by aileron

Lateral Position Hold using the Sideways Control Surface

The transfer function from the sideways control surface deflection to the lateral position with the yaw damper and the bank hold included is found to be:

$$\frac{y(s)}{\delta_s(s)} = \frac{36(s+55)(s+9.5\pm 19.0i)(s+7.3\pm 10.2i)(s+3.9)(s+1.8\pm 1.1i)(s+1.36)}{s^2(s+54)(s+9.1\pm 18.7i)(s+7.0\pm 10.3i)(s+4.2)(s+3.1)(s+1.45)(s+1.34)}$$

Figure 3-18 shows the Bode plot for this autopilot, with the same first order lag actuator model cascaded in the plant dynamics.

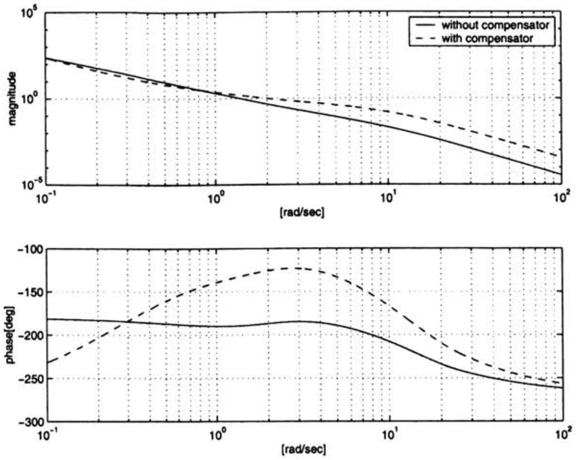

Figure 3-18: Bode plot for sideway position hold using sideway control surface

The following lead-lag compensator

$$D(s) = 0.431 \left(\frac{5s+1}{5s}\right)\left(\frac{24.0 \times 0.102s+1}{0.102s+1}\right)$$

gives a crossover frequency of 2.0 rad/sec and a phase margin of 54^o.

Figure 3-19 shows the time responses to 1.0 meter lateral step in reference, introduced at t=5 sec.

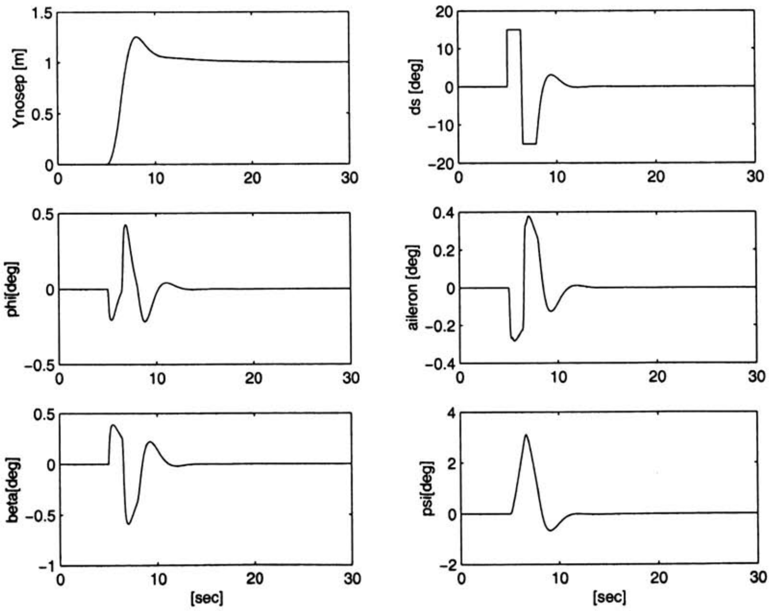

Figure 3-19: Time responses to 1.0 meter sideways step reference at t=5 sec

Some nonlinearities were added to the linear compensators described in this section. Saturation limits were imposed on the control surface deflections. Anti-windups were also imposed in the integration part of the lag compensators.

3.7 Discrete Version of Controller

In order to implement the continuous time controller described above on a digital computer, it should be converted to a discrete-time version. Since the controller has several dynamic compensators and has some nonlinear features such as anti-windup, saturation, and combinations of control surfaces, one could easily make mistakes in writing codes during the development of the corresponding discrete code. As a check for the correctness of the code it was decided to test the code in a so-called "C-MEX" file in Matlab S-function incorporated into the simulation. This technique provides an interface between C language code and the Matlab Simulink environment. So, the discrete version of the controller programmed in C code is incorporated into the Simulink model, and can be checked by simulation.

Each dynamic compensator was converted using a zero order hold (step invariance) method [1],

$$G_D(z) = \mathcal{Z}\left[\frac{1 - e^{Ts}}{s} G(s)\right]$$

where $\mathcal{Z}$: z-transform. T=0.025 is used here as sampling interval. In Matlab it is obtained by the function 'c2dm'.

For example, Figure 3-20 shows the controller block diagram for bank angle hold autopilot. It should be noticed that this controller has a lead compensator in the feedback path as described earlier.

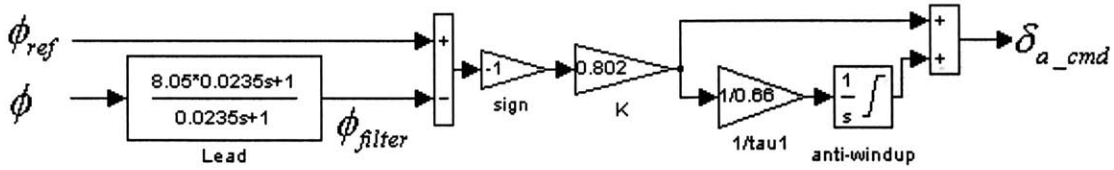

Figure 3-20: Controller block diagram for bank angle hold autopilot

The procedure to obtain a discrete version of this controller is as follows. From the controller transfer function

$$D(s) = \underbrace{0.802\left(\frac{0.667s+1}{0.667s}\right)}_{Lag(s)}\underbrace{\left(\frac{8.05\times 0.0235s+1}{0.0235s+1}\right)}_{Lead(s)}$$

First, $Lead(s)$ is converted with the zero order hold method as

$$\begin{aligned}&Lead(s) \Rightarrow Lead(z) = \frac{\phi_{filter}(z)}{\phi(z)} = \frac{8.05-7.39z^{-1}}{1-0.345z^{-1}}\\ &\Rightarrow \phi_{filter}(k) = 0.345\ \phi_{filter}(k-1) + 8.05\ \phi(k) - 7.39\ \phi(k-1)\end{aligned}$$

Then, we have

$$e_{\phi} = \phi_{ref} - \phi_{filter}$$

Next, $Lag(s)$ is divided into the proportional and the integral terms as follows:

$$Lag(s) = \underbrace{0.802}_{P(s)} + \underbrace{\frac{0.802}{0.667s}}_{I(s)}$$

Then, $I(s)$ is converted as

$$\begin{aligned}&I(s) \Rightarrow I(z) = \frac{U_{e_{int}}(z)}{e_{\phi}(z)} = \frac{0.82\times 0.0375z^{-1}}{1-z^{-1}}\\ &\Rightarrow U_{e_{int}}(k) = U_{e_{int}}(k-1) + 0.82\times 0.0375\ e_{\phi}(k-1)\end{aligned}$$

So, the input $\delta_{a_{cmd}}$ is obtained by

$$\delta_{a_{cmd}}(k) = U_{e_{pro}}(k) + U_{e_{int}}(k)$$

where

$$U_{e_{pro}}(k) = 0.802e_{\phi}(k)$$

$$U_{e_{int}}(k) = \begin{cases} U_{e_{int}}(k-1) + 0.802\times 0.0375\ e_{\phi}(k-1) & \text{if } |U_{e_{int}}(k)| < sat. \\ U_{e_{int}}(k-1) & \text{otherwise}\end{cases}$$

3.8 Simulation

A simulator was constructed in Matlab Simulink. All the controllers, the actuator models, and the gust effects were included in the model. Figures 3-21, 3-22, and 3-23 are obtained from the simulation for initial condition responses where the mini vehicle is 10 meters behind the target point of the parent with 1 meter of sideways position error. Figure 3-21 shows the relative position of the mini vehicle with respect to the parent vehicle. Here, the parent vehicle is modeled to fly at constant speed of 15 m/s. The graphs show that the vertical and lateral deviation is relatively quickly corrected compared to the forward distance deviation.

Figure 3-22 shows all the state variables. Figure 3-23 shows all the actuator variables.

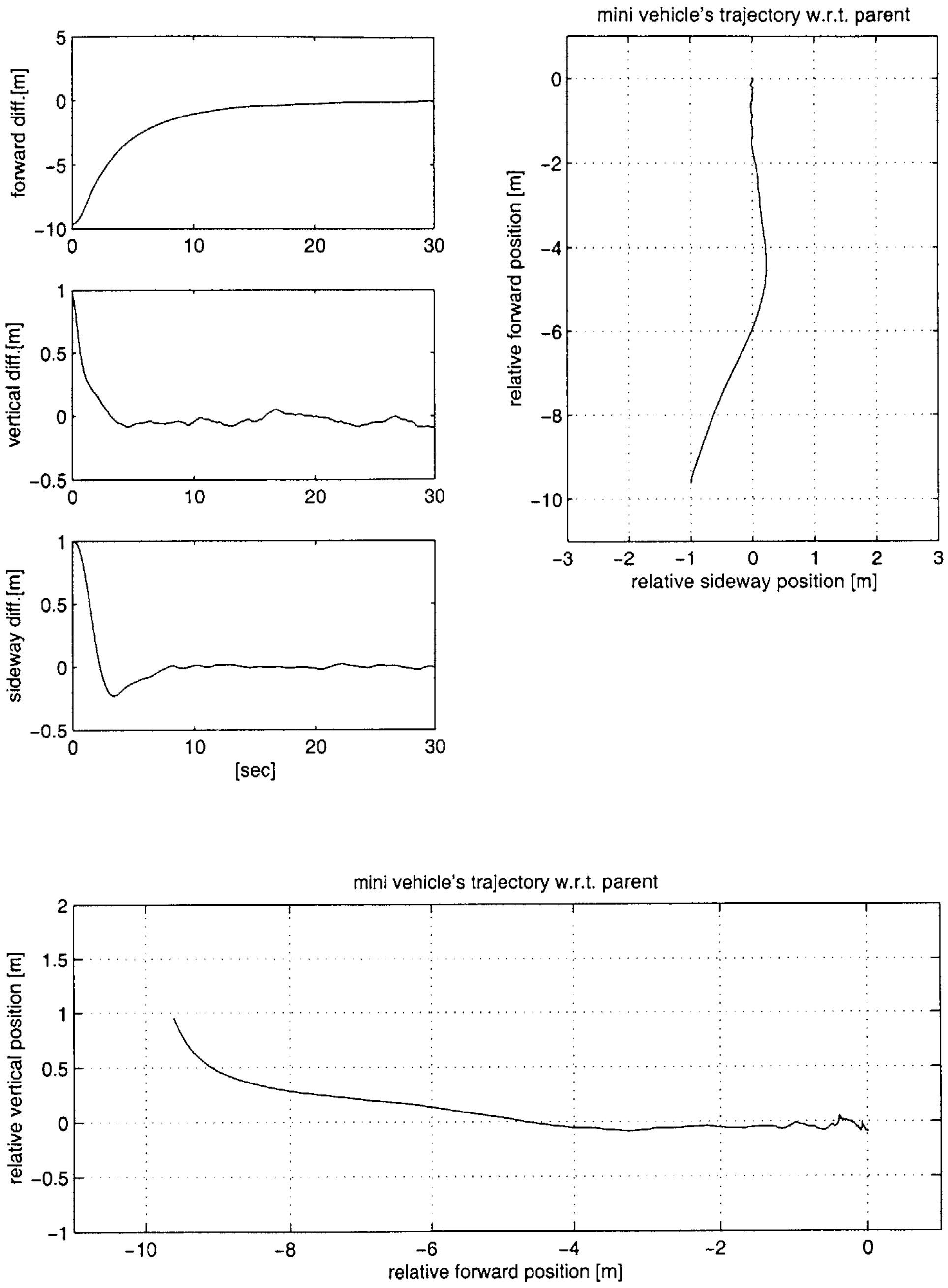

Figure 3-21: Initial condition response, -1.0 meter vertical, 1.0 meter sideway relative difference at t=0 : Relative position

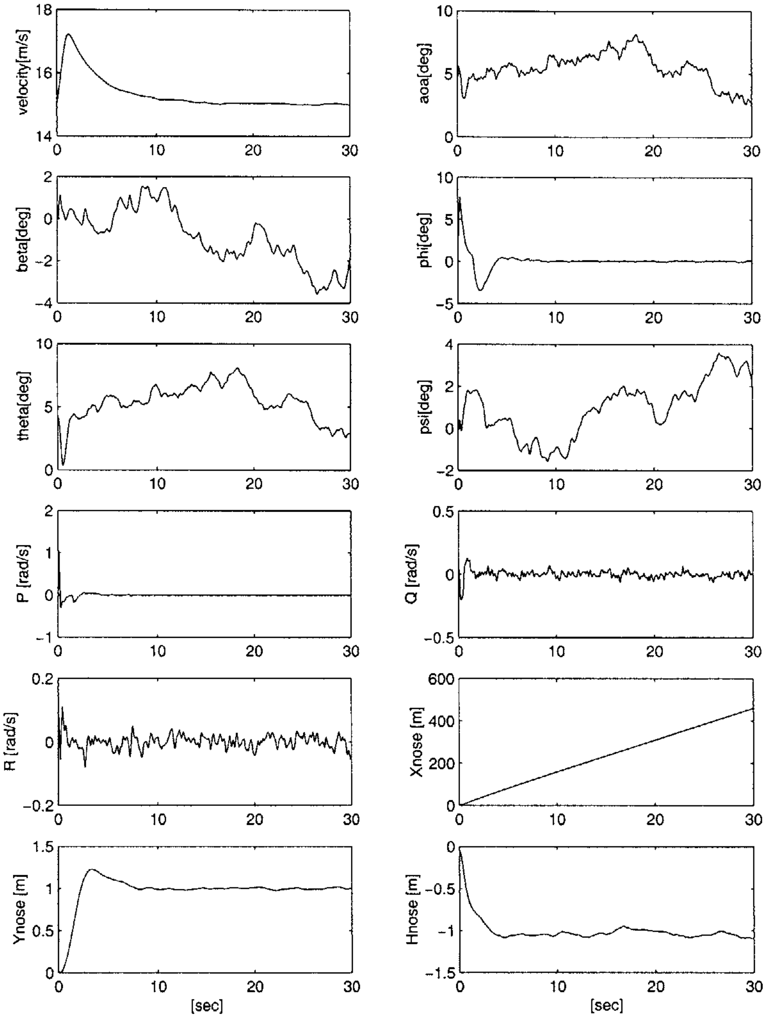

Figure 3-22: Initial condition response, -1.0 meter vertical, 1.0 meter sideway relative difference at t=0 : State variables

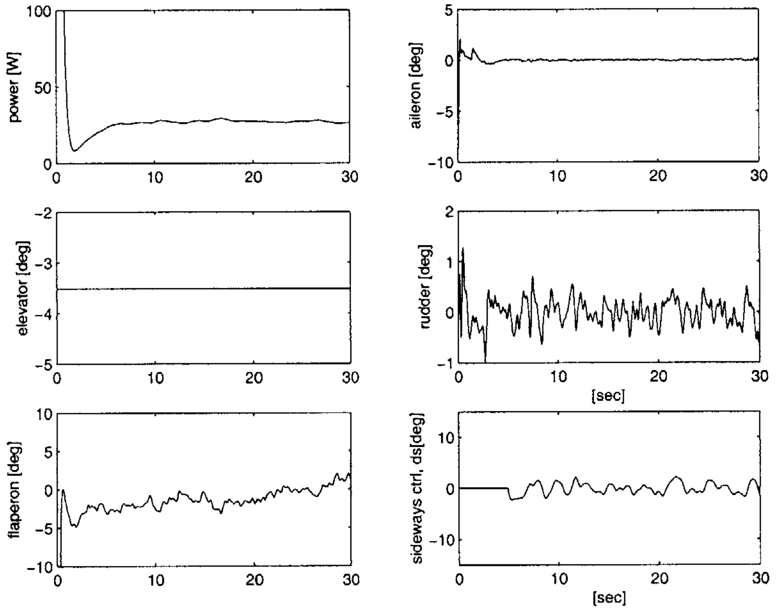

Figure 3-23: Initial condition response, -1.0 meter vertical, 1.0 meter sideway relative difference at t=0 : Actuator states

3.9 Controller Design for the Testbed Aircraft

The controller architecture of the testbed has two major features that are different from the Mini. First, since the testbed doesn't have a direct sideways control surface, it always uses the bank angle to correct lateral position. The second feature is a combined use of the flaperon and elevator to change the altitude as shown in Figure 3-24. As was mentioned in Section 3.6, to correct the altitude, any individual use of elevator or flaperon can result in a non-minimum phase response. First, the use of elevator alone to gain altitude has negative lift during the transition period, because the tail is initially pushed down. Second, the flaperon alone to gain altitude involves pitch down moment. This moment is more significant for an aircraft that has low AR, which leads the nose position of the aircraft moving down, resulting in a non-minimum phase zero (between flaperon input and nose position output) in the linearized model. This can be summarized by comparing the Mini and testbed in terms of the effect of flaperon on lift and pitch-down moment as shown below:

$$\begin{array}{lll} \text{Testbed :} & \text{AR=5.4} \rightarrow & C_{L_{\delta_f}}/C_{M_{\delta_f}} = \text{-4.9} \\ \text{Mini:} & \text{AR=9.0} \rightarrow & C_{L_{\delta_f}}/C_{M_{\delta_f}} = \text{-11.3} \end{array}$$

To overcome this situation the combined use of the flaperon and elevator was employed. In other words, to gain altitude, down-deflection of flaperon and up-deflection of elevator are performed at the same time. It was found from the numerical model that a non-minimum phase zero no longer exists when

$$\frac{\delta_f}{\delta_e} < \frac{80\%}{20\%}$$

This proportion is about the point when the pitching moments due to the two control surfaces balance.

$$\frac{C_{M_{\delta_e}}}{C_{M_{\delta_f}}} = \frac{-1.16}{-0.300} = 3.9$$

In the controller design flaperon(50%) and elevator(50%) setting was used to be in the safe side.

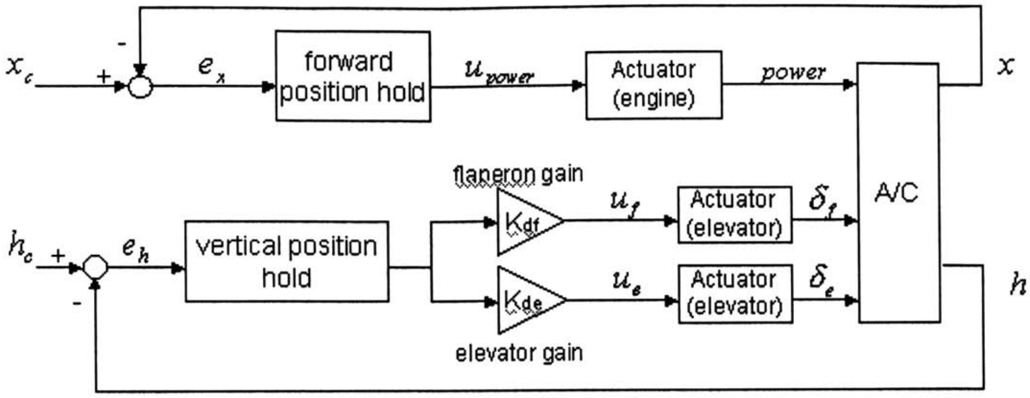

(a) Longtitudinal control

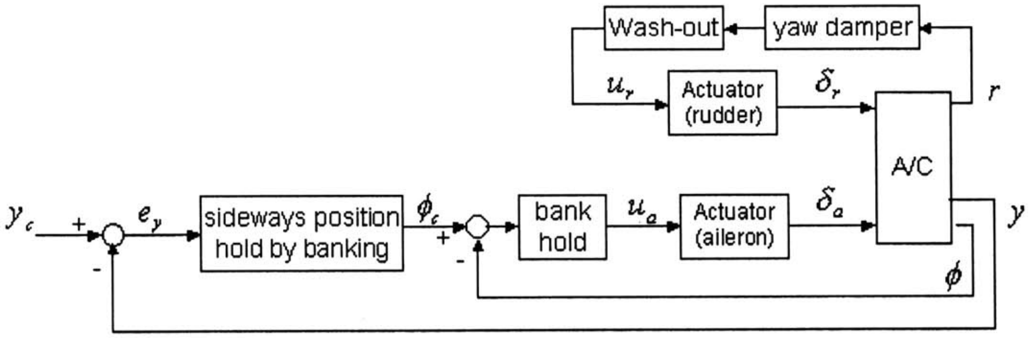

(b) Lateral control

Figure 3-24: Controller Block Diagrams : Testbed Aircraft

3.10 Avionics Subsystem and Implementation of the Control System

Figure 3-25 shows the hardware architecture for the demonstration of reintegration. The envisioned demonstration requires an R/C pilot to perform the initial phase of the reintegration task (Section 3.1), then switch to the autonomous mode. Hence the avionics has a channel for the pilot input. In the pilot control mode the two MP1000 units read the pulse width from receiver #1 and mimic the signal to activate the servo motor. When Phase 1 of the reintegration has been performed by a pilot and a steady state level flight has been achieved, the mode is switched from pilot to computer

	compensator	cross-over [rad/s]	phase margin
vertical position hold	lead-lag	3.5	54
forward position hold	lead-lag	0.6	69
yaw damper	proportional	dominant poles :	-11.9±13.2i
bank hold	lead-lag	10.1	69
sideways position hold(banking)	lead-lag	1.0	54

Table 3.6: Summary of Controllers : Testbed Aircraft

control. During this switch-over, the steady state control input is maintained by MP1000. In the computer control mode, the flight control input is transmitted from the main computer to the MP1000 via an RS232 line. The mode switch is performed by the following signal flow : co-pilot → receiver #3 → switch → computer → MP1000. Another receiver (#2) is used to allow a safety channel that by-passes the MP1000. This selection is performed using the 6 channel relay switch which is triggered by the co-pilot transmitter through one of the channels in receiver #3.

The CPU, power board, and framegrabber were chosen for compatibility with the PC/104 stack. The PC/104 is a standard format for hardware cards with physical dimension of about 10x10x2 cm. The cards can be attached to each other through connectors which provide the PC/104 bus. Onboard computing is provided by a CMW6686GX 233 MHz with 64 M bytes surface mount SDRAM. It has a video controller and PC/AT standard keyboard port. Thus, it provides a user friendly development environment. For the vision positioning sensor (refer to Chapter 4 for detailed description), two Supercircuits PC-53XS Color Microvideo cameras were used for the CCD cameras. Each weighs 1/3 ounce and has horizontal and vertical field of view angles of 72^o and 54^o respectively [3]. Output is standard NTSC video. An Ajeco ANDI-framegrabber digitizes the output of the CCD camera for digital processing. It provides a speed of 25 pictures per second in the fastest mode with a limited number of uploaded pixels.

Attitude estimation is done using a complementary filter, where the integration of rate gyro is fed through a high-pass filter and the roll angle estimated by assuming

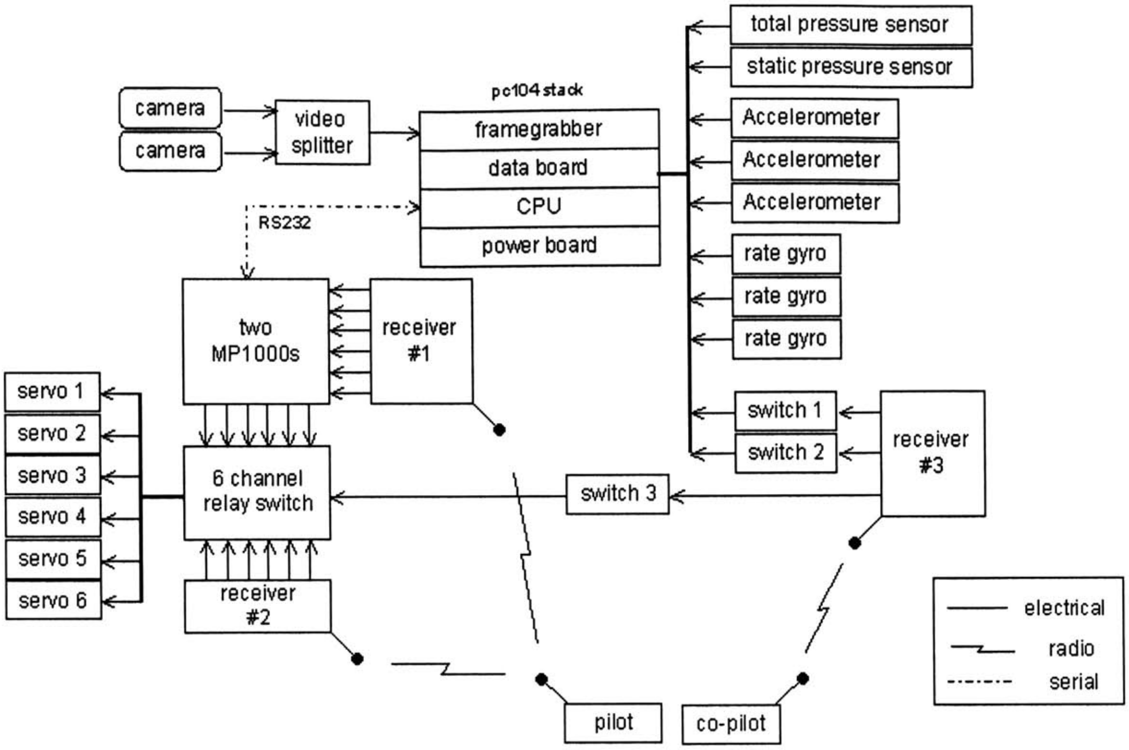

Figure 3-25: Signal flowAvionics for Reintegration Demonstration

steady-state coordinated turn using the equation

$$\phi = \frac{V\ \dot{\psi}}{g}$$

is fed through low-pass filter. Detailed description of the avionics system development and attitude estimation is described in [9].

Regarding the timing of the controller, the attitude angle controller was closed with a 40 Hz sampling rate. The timing of the vision system was programmed such that a position is estimated at every 7th sample. This corresponds to 5.71 Hz, which is about 10 times higher than the position controller dynamics.

Hardware-in-the-loop simulation was also performed. This provides a good method to check the program code in the flight computer. Figure 3-26 shows the hardware architecture for this. The flight code is executed in the flight computer and the aircraft dynamics are provided by the simulation computer. The control inputs to the servo motors are read using potentiometers mounted on the motor shaft, whose outputs are converted by an A/D board in the simulation computer. The simulation computer solves the differential equations in real time and generates the vehicle states. These values are converted by a D/A board to voltages and read by the flight computer through a data board. It served as a useful tool to check bugs in flight codes in the development stage of programming.

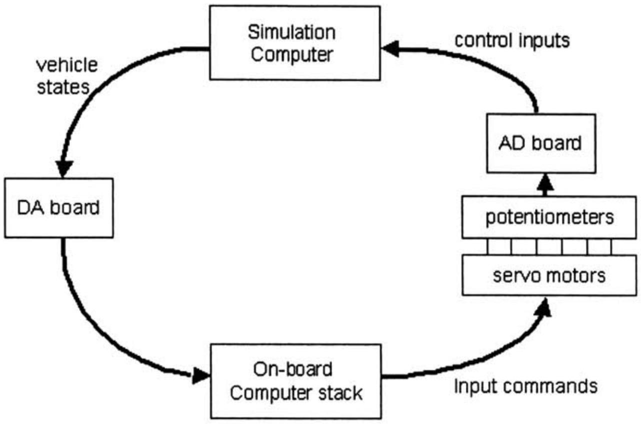

Figure 3-26: Hardware-in-the-loop Components

Chapter 4

Vision Based Positioning System

The concept of the vision based positioning system can be explained by Figure 4-1. It requires two CCD cameras and a target light source with a specific color. The images on the two cameras are discretized into an array of pixels by a framegrabber. Each pixel contains discrete R,G,B (Red, Green, Blue) values. The target can be detected using the R,G,B values of each pixel. The centroid of the target pixels is next computed. Then, by comparing the two pixel locations of the target in the left and the right camera images, the coordinates of the target position are obtained based on a geometric relation.

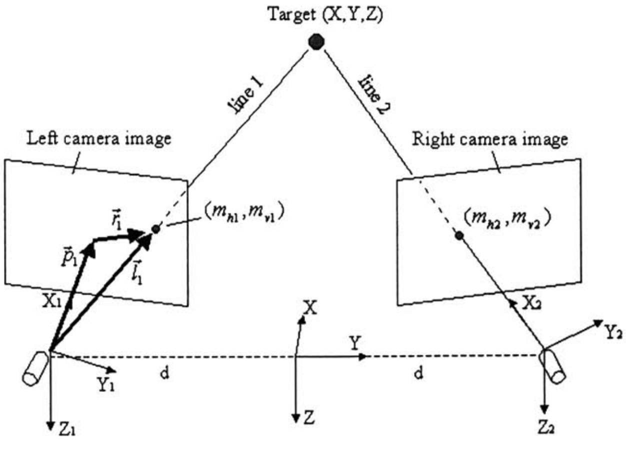

Figure 4-1: Concept of a vision based positioning system

4.1 Calculation of Target Coordinates

The geometric relation for computing the coordinates of the target can be derived by first imagining two camera images placed in front of the two cameras at right angles to their line of sight as shown in Figure 4-1. If there is no distortion in the image, the line from the object through the object's image on the plane to the camera is straight. Next, three vectors, $\vec{l}$, $\vec{p}$, $\vec{r}$ are introduced for each side as depicted in Figure 4-1, where

$\vec{l}$: a vector from the camera to the target on the imaging plane

$\vec{p}$: a vector from the camera to the center point of the imaging plane

$\vec{r}$: a vector from the center point to the target on the imaging plane

Then the following vector relations are used for each side.

$$\vec{l_1} = \vec{p_1} + \vec{r_1} = \left\{ \begin{array}{c} p_1 \\ r_{y_1} \\ r_{z_1} \end{array} \right\}_{x_1 y_1 z_1} \qquad \vec{l_2} = \vec{p_2} + \vec{r_2} = \left\{ \begin{array}{c} p_2 \\ r_{y_2} \\ r_{z_2} \end{array} \right\}_{x_2 y_2 z_2}$$

The vectors $\vec{l_1}$ and $\vec{l_2}$ coordinatized in each camera frame need to be expressed in the frame XYZ in Figure 4-1 by using the following relations

$$\left\{ \begin{array}{c} l_{x_1} \\ l_{y_1} \\ l_{z_1} \end{array} \right\}_{XYZ} = [\eta_1]^T [\zeta_1]^T [\epsilon_1]^T \left\{ \begin{array}{c} p_1 \\ r_{y_1} \\ r_{z_1} \end{array} \right\}, \quad \left\{ \begin{array}{c} l_{x_2} \\ l_{y_2} \\ l_{z_2} \end{array} \right\}_{XYZ} = [\eta_2]^T [\zeta_2]^T [\epsilon_2]^T \left\{ \begin{array}{c} p_2 \\ r_{y_2} \\ r_{z_2} \end{array} \right\}$$

where $[\eta]$, $[\zeta]$, and $[\epsilon]$ are rotational transformation matrices corresponding to the three consecutive Euler angles, inward(η), downward(ζ), and rotational(ϵ), to describe the camera attachment angle as defined in Figure 4-2. Next, the intersection between $line_1$ and $line_2$ in the Figure 4-1 is found from

$$line_1 \text{ passes through points } (0, -d, 0), \text{ and } (l_{x_1}, l_{y_1} - d, l_{z_1}) \ : \ \frac{x}{l_{x_1}} = \frac{y+d}{l_{y_1}} = \frac{z}{l_{z_1}}$$

$$line_2 \text{ passes through points } (0, +d, 0) \text{ and } (l_{x_2}, l_{y_2} + d, l_{z_2}) \ : \ \frac{x}{l_{x_2}} = \frac{y-d}{l_{y_2}} = \frac{z}{l_{z_2}}$$

Then, by setting $|\vec{p}| = 1$(arbitrary) and getting relations for r_y and r_z from target pixel locations on the screen, the X,Y,Z coordinates with respect to the coordinate

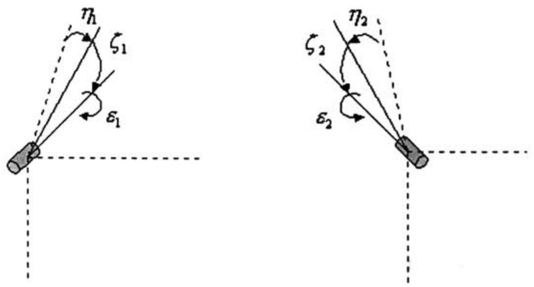

Figure 4-2: Definition of the camera attachment angles

frame shown in the figure can be obtained. The following equations summarize the procedure to obtain the coordinates.

$$
\begin{aligned}
Y &= d \cdot \frac{l_{x_1} l_{y_2} + l_{x_2} l_{y_1}}{l_{x_2} l_{y_1} + l_{x_1} l_{y_2}} \\
X &= (Y + d) \cdot \frac{l_{x_1}}{l_{y_1}} \\
Z &= X \cdot \frac{l_{z_1}}{l_{x_1}},
\end{aligned}
$$

where

$$
\begin{Bmatrix} l_{x_1} \\ l_{y_1} \\ l_{z_1} \end{Bmatrix} = [\eta_1]^T [\zeta_1]^T [\epsilon_1]^T \begin{Bmatrix} 1 \\ r_{y_1} \\ r_{z_1} \end{Bmatrix}, \quad \begin{Bmatrix} l_{x_2} \\ l_{y_2} \\ l_{z_2} \end{Bmatrix} = [\eta_2]^T [\zeta_2]^T [\epsilon_2]^T \begin{Bmatrix} 1 \\ r_{y_2} \\ r_{z_2} \end{Bmatrix},
$$

and

$$
[\eta_1] = \begin{bmatrix} \cos\eta_1 & \sin\eta_1 & 0 \\ -\sin\eta_1 & \cos\eta_1 & 0 \\ 0 & 0 & 1 \end{bmatrix}, \quad [\eta_2] = \begin{bmatrix} \cos\eta_2 & -\sin\eta_2 & 0 \\ \sin\eta_2 & \cos\eta_2 & 0 \\ 0 & 0 & 1 \end{bmatrix},
$$

$$
[\zeta_1] = \begin{bmatrix} \cos\zeta_1 & 0 & \sin\zeta_1 \\ 0 & 1 & 0 \\ -\sin\zeta_1 & 0 & \cos\zeta_1 \end{bmatrix}, \quad [\zeta_2] = \begin{bmatrix} \cos\zeta_2 & 0 & \sin\zeta_2 \\ 0 & 1 & 0 \\ -\sin\zeta_2 & 0 & \cos\zeta_2 \end{bmatrix},
$$

$$
[\epsilon_1] = \begin{bmatrix} 1 & 0 & 0 \\ 0 & \cos\epsilon_1 & \sin\epsilon_1 \\ 0 & -\sin\epsilon_1 & \cos\epsilon_1 \end{bmatrix}, \quad [\epsilon_2] = \begin{bmatrix} 1 & 0 & 0 \\ 0 & \cos\epsilon_2 & -\sin\epsilon_2 \\ 0 & \sin\epsilon_2 & \cos\epsilon_2 \end{bmatrix},
$$

and

$$\begin{aligned} r_{y_1} &= \tfrac{2m_{h_1}-N_h}{N_h}\tan\alpha & \qquad r_{y_2} &= \tfrac{2m_{h_2}-N_h}{N_h}\tan\alpha \\ r_{z_1} &= \tfrac{2m_{v_1}-N_v}{N_v}\tan\beta & \qquad r_{z_2} &= \tfrac{2m_{v_2}-N_v}{N_v}\tan\beta \end{aligned}$$

where

X, Y, Z : target coordinates from the mid-point between two cameras
$2\alpha = 72^o, 2\beta = 57^o$: horizontal/vertical field of view angles
η_1, η_2 : inward camera attachment angles
ζ_1, ζ_2 : downward camera attachment angles
ϵ_1, ϵ_2 : rotational camera attachment angels
$N_h = 320, N_v = 240$: total number of horizontal/vertical pixels
m_{h_1}, m_{h_2} : horizontal pixel number of target point from left/right camera
m_{v_1}, m_{v_2} : vertical pixel number of target point from left/right camera
$2d$: distance between two cameras

The position signals that are used in the feedback control are the ones coordinatized in the inertial frame. So the coordinates (X,Y,Z) obtained from the vision system should be transformed by the relation

$$\left\{\begin{array}{c} X \\ Y \\ Z \end{array}\right\}_{for\ feedback} = [\psi]^T[\theta]^T[\phi]^T \left\{\begin{array}{c} X - x_{nose} \\ Y \\ Z - z_{nose} \end{array}\right\}$$

where x_{nose} and z_{nose} are distances in x and z directions from the midpoint of the two cameras to the nose location.

4.2 Detection

The detection of the target is accomplished by scanning through the pixels and using their RGB (Red, Green, Blue) values. A red light was selected as a target, because it is considered to be the most "unnatural" color. The size of the target was chosen based on the relation between the distance from the cameras to the target and the number of pixels that the target occupies in the pixel array. For example, the relation in the case of the 14cm by 14cm target is

distance	2m	4m	6m	8m	10m
Ideal no. of pixels	289	64	25	16	9

A target was carefully devised in such as way that it emits a uniform light intensity throughout the 14cm×14cm target surface area. Four small light bulbs are used with a red semitransparent material. Another semitransparent material is inserted right in front of the light bulb to improve the uniformity of light of the target surface. A schematic of the target used during the development is shown in Figure 4-3.

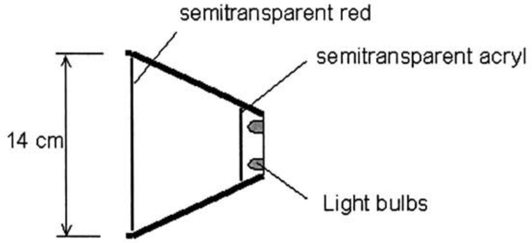

Figure 4-3: Target schematics

Two detection methods were used. The first method is to specify proper thresholds of the RGB values for the target detection. In this case, the pixels whose RGB values fall within the specified boundaries are declared as the target pixels. The typical RGB values for the chosen target with a red light source, when the distance from the camera is about one meter, are 240,170, and 170 out of $256 (= 2^8)$ with standard deviation of 10∼20. Because of the quality of the image from this kind of small CCD camera, the color leakage from green and blue is significant. That is why the red light target has significant amounts of G and B values.

A problem was found in using only this first method for the target detection. In addition to the leakage phenomenon, the RGB values of the target change depending on the distance from the camera as shown in Figure 4-4 and on the background of the target. In general, the RGB values drop with longer distance (about 30 percent

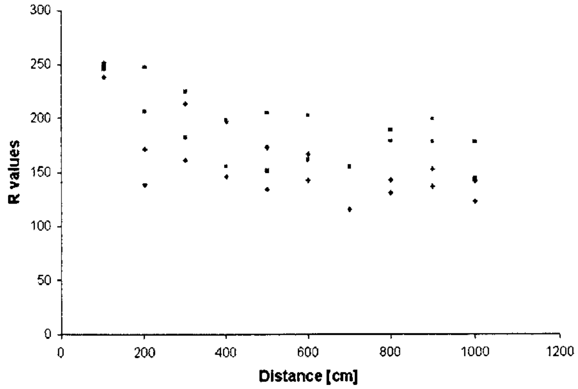

Figure 4-4: RGB value trends vs. distance (exampe: R)

decrease at 10 meters) and with brighter background. So to deal with this gradual change of the RGB values, the threshold for the detection at each time step are programmed to change based on the RGB values of the target previously obtained in the earlier steps. In short, this first detection method is suitable for short range target detection, but it is not good for long distance target. It is also not appropriate for the initial detection because a proper selection of the RGB ranges for the target detection is difficult.

To solve this problem a second method for detection was devised. This method chooses a pixel which has the maximum value of R/(G+B) as the target pixel. The second method was used for the longer range detection and the initial detection of the target. But it was not used for the short distance because two different points in the target surface can be chosen as target pixels from the left and right cameras, which could lead to significant errors in the position calculation when the distance is short. So, the transition from one method to the other was done during the implementation based on the distance calculation. The distance chosen for this transition was 2.5 meters considering the number of pixels that can be chosen as target and the resolution setting which is described in Section 4.4.

Initial detection

During each step in the implementation, only a small portion ("window") of the pixels are scanned by the algorithm because of the speed limitations which will be described later in Section 4.4. The location of the windows will be chosen based on the previous locations of the target pixels. But for the initial detection, since the location of the target pixel is initially unknown, the whole pixel array should be scanned. Once the target is detected in the initial detection phase, only a small portion of the pixels are uploaded in the following time steps. For this reason, the success of the initial detection is critical. In order to improve the reliability of the initial detection, the following algorithm was used. It is envisioned that before the controller is activated for the second phase of reintegration, several pictures of full size will be taken, and the second detection method applied. The target locations from these pictures are averaged, weighting more recent pictures more heavily. This reduces the chance of false detection from any possible background spot, since the background will keep changing in the reintegration situation while the target position stays relatively in the same position with respect to the cameras if the initial distance between the two vehicles is around 10 meters.

4.3 Accuracy

In order to investigate the accuracy properties, a number of static tests were performed. A set of pictures of a target were taken using the two cameras and the framegrabber. Then, the actual locations of the target and the computed locations based on the geometric relations were compared.

A simple pre-calibration was applied to improve the estimates of the position. The following linear relations were used.

$$\begin{aligned} X_{est} &= K_1 \times X_{raw} + B_1 \\ Y_{est} &= K_2 \times Y_{raw} + B_2 \end{aligned}$$

$$Z_{est} = K_3 \times Z_{raw} + B_3$$

where X_{raw}, Y_{raw}, and Z_{raw} are obtained in the geometric relation described in Section 4.1.

This calibration was done by taking one picture from each camera with 640 × 480 resolution, where the image taken contains several objects whose actual coordinates are known. More than six points close to (~1 m) and far away (~10 m) from the camera were selected for the calibration setting. Their pixel locations on the two images were processed to get $(X_{raw}, Y_{raw}, Z_{raw})$. Then, using the matlab function, 'fminsearch', K_i's and B_i's that minimize

$$\sum \left(\frac{error}{distance} \right)^2$$

were found. The term, $(1/distance)$ is introduced above as a weighting factor to improve accuracy at close range.

The K_i's and B_i's obtained by this method were then applied to the other data points in the static test. The results are summarized in the Figure 4-5. The graphs show the errors in the x,y, and z directions as functions of the distance in the x-direction, from 10 meters to 10 centimeters. As the target gets closer to the cameras, the errors become smaller. The errors in the y and z directions are quite small relative to the x direction errors. The errors in the x direction are large when the distance is more than about 3 meters. But this is considered not to be a problem because in the forward position hold controller, the forward distance error input is limited to be less than one meter to prevent large power transients.

A first order low pass filter was applied to the position estimates to reduce the effect of the detection of any red spot from the background or other sources of disturbance. Using the Euler approximation for the discrete implementation, the filter was added on each axis of the position calculation. The bandwidths were chosen to be about five times higher than the crossover frequencies of the position controllers.

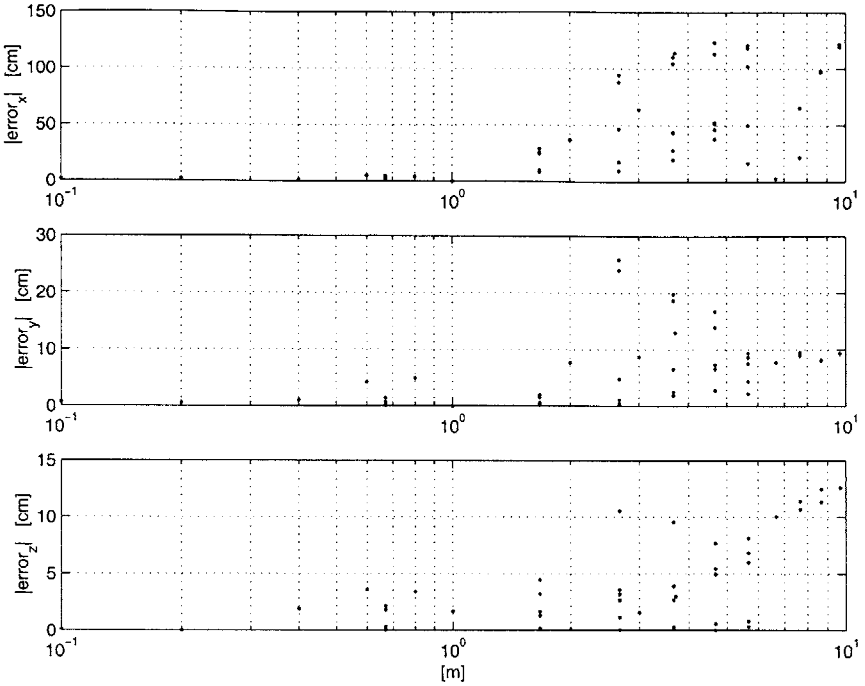

Figure 4-5: Position error characteristics. Note scales: errors are much larger in the x-direction.

4.4 Speed

A mistake was made in the selection of the PC/104 framegrabber. One of the main constraints that the team considered for the selection of the framegrabber was the number of the camera inputs that the framegrabber provides. There were not many choices in this respect. The team selected the Ajeco ANDI-FG framegrabber, which provides two camera inputs with a speed of 25 frames per second. This framegrabber was considered to be suitable for an application of this kind because it was expected that a speed of about 12 Hz would be achieved with the two camera images. But it was later found that the expected speed couldn't be achieved, because it takes about 2-300 ms to switch from one camera input to the other due to synchronization delay. The use of a video splitter was suggested to deal with this problem. Instead of feeding the two camera inputs directly to the framegrabber, the video splitter takes the two camera inputs first. Then it produces an image divided into a few screens, each of which takes one camera image. A quad splitter(QS-14 Digital Real Time Color Quad

Processor, Supercircuits) was chosen. This device maintains the same field of view, but the resolution had to be reduced by a factor of four.

The main constraint of the speed of the vision system was the data upload rate from the framegrabber to the main CPU. The data transfer rate through the PC/104 bus for the ANDI-FG framegrabber is 800 kbytes/sec. Two sections in the quad splitter contain a total of 153,600 ($2 \times 320 \times 240$) pixels. One pixel contains 3 bytes of information for R,G,B, each of which is 8 bits. So if two entire images are processed at each time step during implementation, a total of 460.8 kbytes of data should be uploaded, which would result in about 2 Hz upload rate. Thus, it was decided to program the system so that only a small part of the pixel data is uploaded for processing. In other words, a small window was specified for the data upload at every time step during the implementation, based on the target pixel location detected in the previous step.

The window size was programmed to change, depending on the distance between the target and the camera, because the target can take up a significant portion of the whole image when it is close to the camera, while it takes up only several pixels when it is far away. In order to maintain a proper number of target pixels to upload, it is necessary to change the resolution of the pixels in the window. In other words, when the target is far away from the cameras, a small window with the maximum resolution setting was used, while for the short range a larger widow with a low resolution setting was used. By trial and error, the settings shown in Figure 4-6 were implemented.

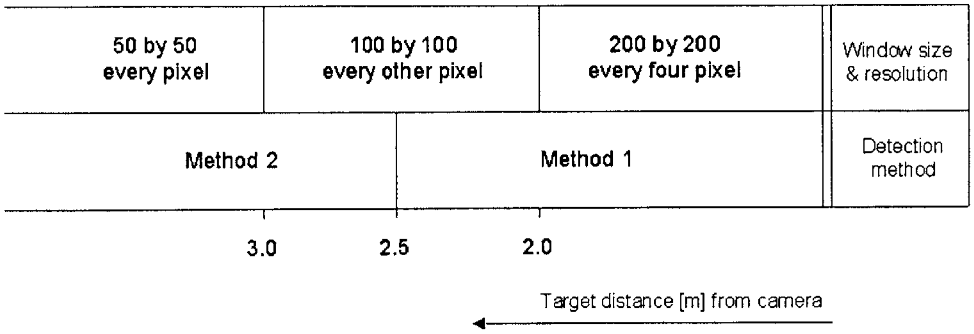

Figure 4-6: Window size, resolution, and detection methods settings vs. distance

It can be noticed that only 2500(50×50) pixels from each side of the camera are uploaded and processed due to speed limitations. The implementation rate with this setting is 7.7 Hz.

4.5 Implementation and Test

A simple C language program code for snapping an image and uploading the RGB data to the buffer was provided from the framegrabber manufacturer. A loop algorithm was added for successive uploading of the images. Then, the other features such as the variation of window size, resolution, and detection methods were added. Figure 4-7 shows the basic program algorithm implemented with these features.

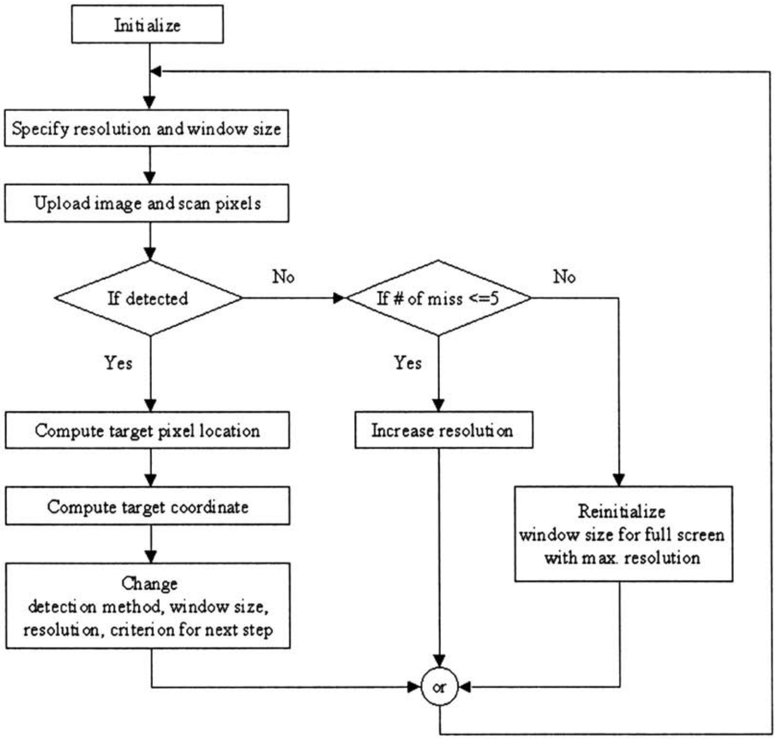

Figure 4-7: Program Algorithm

An algorithm to deal with loss of the target is also described in Figure 4-7. If the target is not detected, the resolution is increased for the next step, which would decrease the speed, while estimating the position based on some previous target locations. If the target is not detected more than 5 times in a row, the program reverts to the full window size, maximum resolution with detection method 1, which is the setting for the initial detection of the target.

A test was done to determine the performance of the target tracking system. Figure 4-8 shows a schematic diagram for the test setup. Two cameras were fixed on a tripod on the ground and the red light target was made to move along a straight line attached to a string which is linked to a pulley. A gear box was devised to provide an adequate number of turns from the pulley to a potentiometer. The output of the potentiometer was fed into the PC/104 computer through a data board. Then the time history of the actual location was recorded from the potentiometer and it was compared with the trajectory computed from the vision system. Figure 4-9 and 4-10 show the results of the test. The target was moved by hand randomly in various ways along the straight line between the two pulleys. The trajectories of the actual location are plotted with dotted lines, and the computed trajectories using the vision system are plotted with solid lines on the graphs.

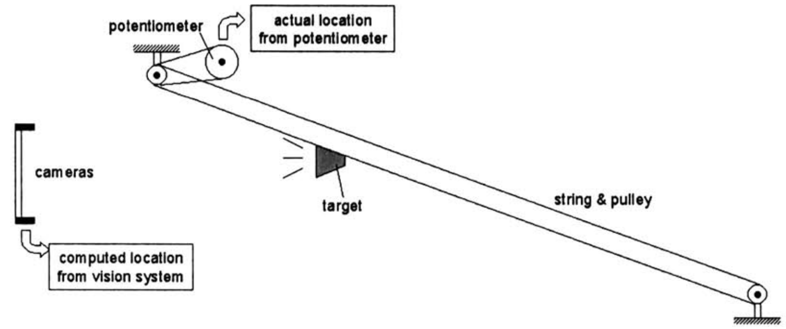

Figure 4-8: target tracking experiment setup

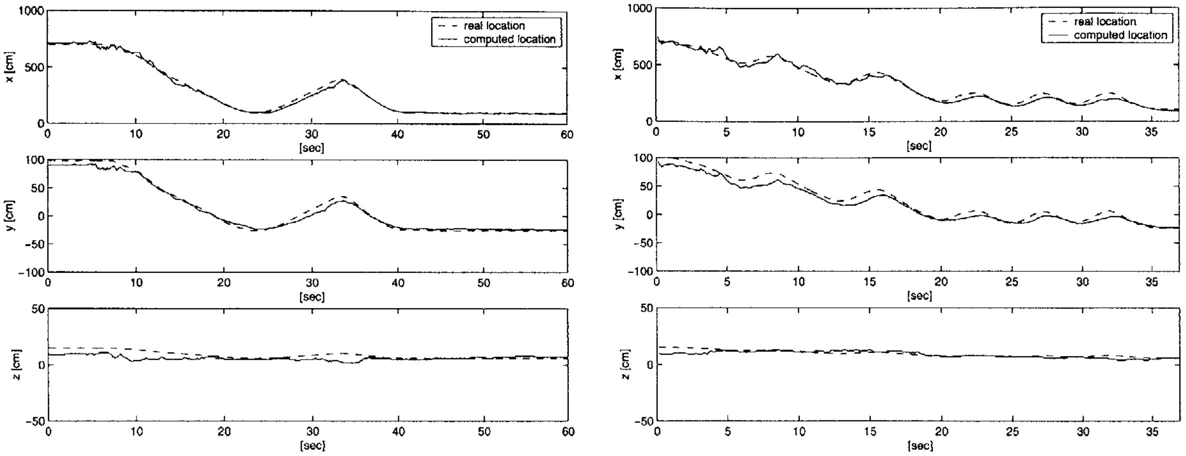

(a) test 1

(b) test 2

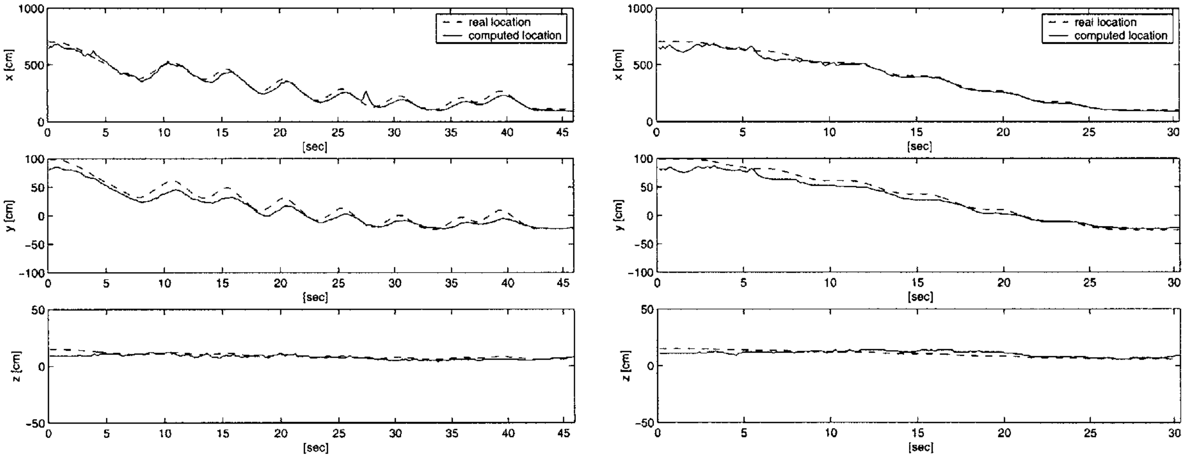

(c) test 3

(d) test 4

Figure 4-9: Target tracking tests. Note scale differences

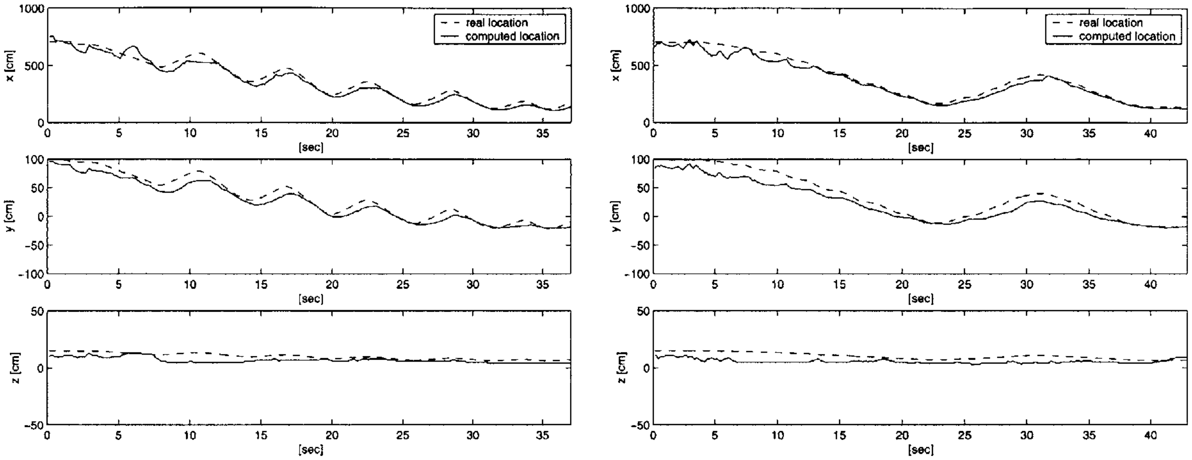

(e) test 5 (f) test 6

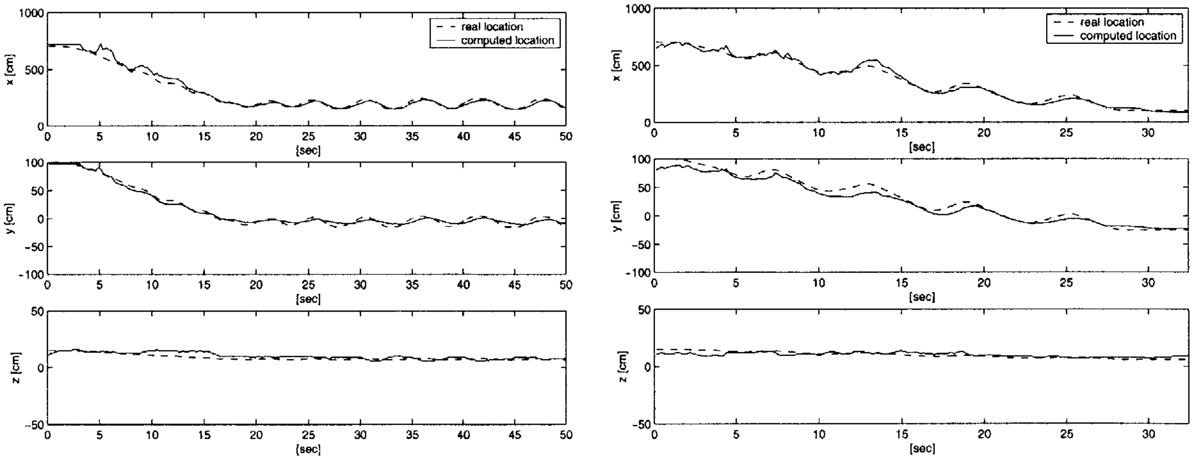

(g) test 7 (h) test 8

Figure 4-10: Target tracking tests. Note scale differences

4.6 Sensor Modeling

Based on the performance of the position sensor observed in the test, the sensor was modeled for the flight simulation discussed in Chapter 3. As was described, the time history of the real location of the target was recorded through the potentiometer, and it was compared with the one computed from the vision system. Hence, it was suggested that a signal with similar noise characteristics and phase delays be generated and used for the feedback in the simulation.

Figure 4-11 shows the Matlab Simulink block for the implementation of the sensor model in estimating the position in the y-direction. Noise is modeled to be composed of a bias part and a high frequency noise. Both are functions of the position in the x-direction. A simple discretizing algorithm is used to represent the discrete output due to the finite number of pixels. The actual width per pixel depending on distance in the x-direction was considered in this block. The first order filter and the delay of 1/8 [sec] from the sensor position update rate are also added. Figure 4-12 shows the simulated signal generated from the block diagram. The experiment data are also shown in this figure.

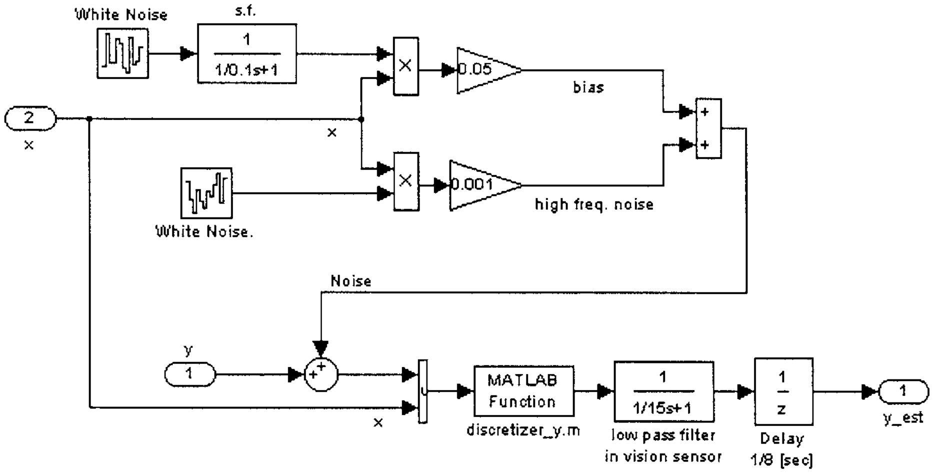

Figure 4-11: Position sensor modeling

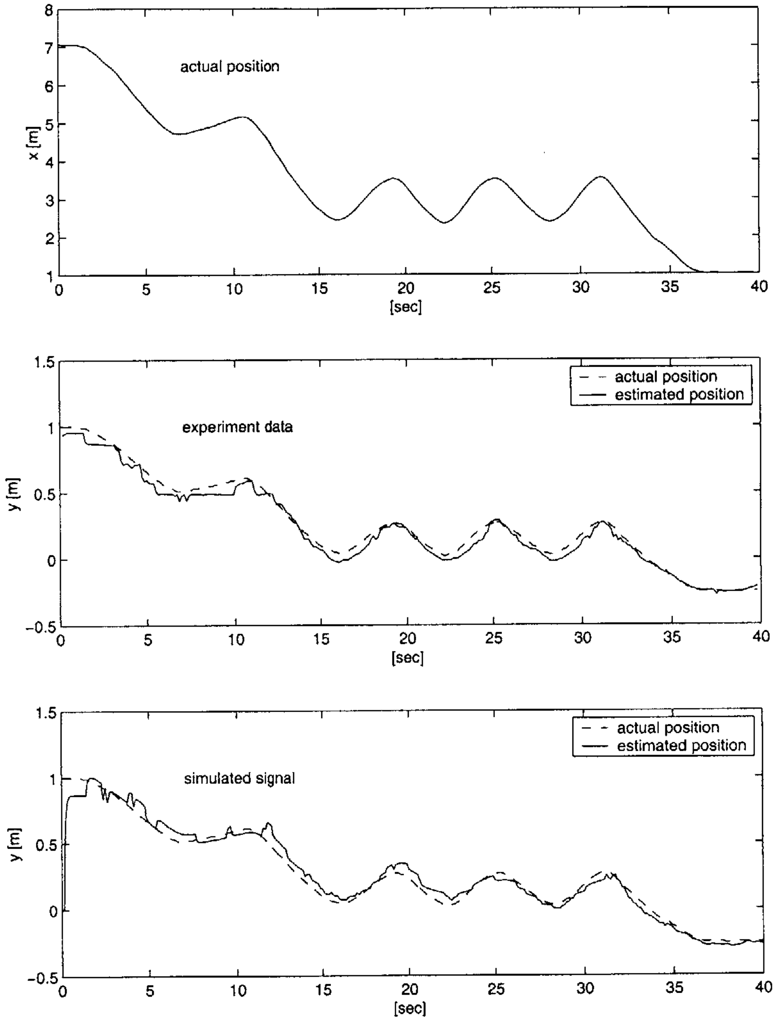

Figure 4-12: simulated signal

Chapter 5

Conclusion

During the two years of the PCUAV (Parent Child Unmanned Air Vehicle) project, many areas have been explored by the team. The author participated in three aspects.

The design of the parent and the mini UAVs and the configuration of the vehicle integration between these vehicles were first explored. Devising appropriate configurations for the parent and the mini vehicles and finding the right relative positions for the integration between the two different sized UAVs were difficult tasks. The team's approach was to seek an integration concept that increased the advantages and reduced the disadvantages associated with the presence of the smaller mini vehicle with the larger parent vehicle. A number of integration concepts were considered. These were analyzed and compared first in terms of performance. The aerodynamic properties for each integration concept were estimated. Then the performance properties, such as range and endurance for each concept, were predicted. The stability and the controllability of the parent vehicle during deployment of the mini vehicle were also investigated.

Air rendezvous between the parent and the mini vehicle was identified as an important capability of the PCUAV system. The three-phase scenario for the mid-air integration was devised. The team worked mainly on the second phase, which involves control of the mini vehicle as it follows the parent and makes physical contact. The use of the non-conventional control surfaces was suggested as direct translational force generators. A model of the mini vehicle was constructed and the controller was designed. The combination of the direct force generator with the conventional control surfaces were tried and verified through the simulation.

A vision based positioning system was developed as a three-axis position sensor for the mid-air reintegration. Various features were employed in the implementation to improve the performance in terms of detection, accuracy, and speed. The performance of this subsystem is verified by experiment, from which a sensor model was created for the flight simulation.

Currently (Oct. 2000) the PCUAV project is implementing controllers on the testbed aircraft. Also, a resized Mini vehicle has been built. It is expected that the control system described here will be implemented on this vehicle in the near future.

Appendix A

Vehicle Integration Concept B

Appendix A summarizes the performance and stability data for the parent-mini vehicle integration concepts B1 and B2. The configuration of these concepts are already introduced in Figure 2-15, which shows the plane views of these concepts with some dimensions and the inboard layout. These configurations were considered by the team with two more other options during the second year of the project for the final downselection for the PCUAV vehicle integration concept.

Though the data in this section are confined to the integration concept B, the figures presented here reveal a little bit more detailed procedures to get the performance characteristics and the stability properties, which were omitted in Chapter 2 where the analysis on the other integration concepts was described.

Figure A-1 and A-2 show the aerodynamic characteristics. These were maily predicted using the Athena Vortex Lattice program. The aerodynamic properties then lead to Figure A-3, which shows the procedure to obtain the speed vs. power relations. The performance features are obtained based on this plot. Figure A-4 and A-5 show the forward and the backward c.g. limits respectively. Then, Figure A-6 shows the proper c.g. ranges related with the deployment of the mini vehicles. Figure A-7 summarizes all the data related with the concept B. It shows the data on the performance and the stability as well as some geometric properties.

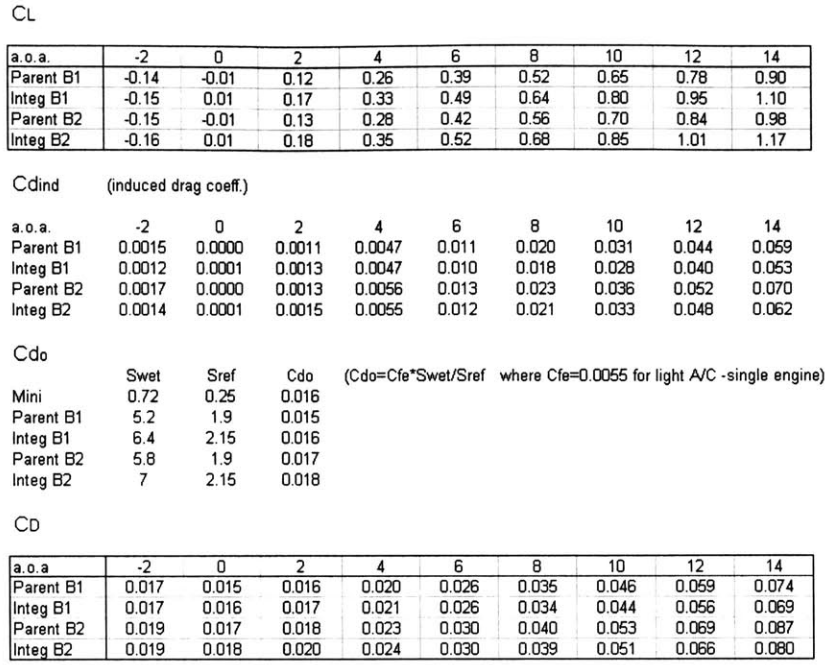

CL

a.o.a.	-2	0	2	4	6	8	10	12	14
Parent B1	-0.14	-0.01	0.12	0.26	0.39	0.52	0.65	0.78	0.90
Integ B1	-0.15	0.01	0.17	0.33	0.49	0.64	0.80	0.95	1.10
Parent B2	-0.15	-0.01	0.13	0.28	0.42	0.56	0.70	0.84	0.98
Integ B2	-0.16	0.01	0.18	0.35	0.52	0.68	0.85	1.01	1.17

Cdind (induced drag coeff.)

a.o.a.	-2	0	2	4	6	8	10	12	14
Parent B1	0.0015	0.0000	0.0011	0.0047	0.011	0.020	0.031	0.044	0.059
Integ B1	0.0012	0.0001	0.0013	0.0047	0.010	0.018	0.028	0.040	0.053
Parent B2	0.0017	0.0000	0.0013	0.0056	0.013	0.023	0.036	0.052	0.070
Integ B2	0.0014	0.0001	0.0015	0.0055	0.012	0.021	0.033	0.048	0.062

Cdo

	Swet	Sref	Cdo
Mini	0.72	0.25	0.016
Parent B1	5.2	1.9	0.015
Integ B1	6.4	2.15	0.016
Parent B2	5.8	1.9	0.017
Integ B2	7	2.15	0.018

(Cdo=Cfe*Swet/Sref where Cfe=0.0055 for light A/C -single engine)

CD

a.o.a	-2	0	2	4	6	8	10	12	14
Parent B1	0.017	0.015	0.016	0.020	0.026	0.035	0.046	0.059	0.074
Integ B1	0.017	0.016	0.017	0.021	0.026	0.034	0.044	0.056	0.069
Parent B2	0.019	0.017	0.018	0.023	0.030	0.040	0.053	0.069	0.087
Integ B2	0.019	0.018	0.020	0.024	0.030	0.039	0.051	0.066	0.080

Figure A-1: Estimation of lift and drag coefficients for concepts B1 and B2

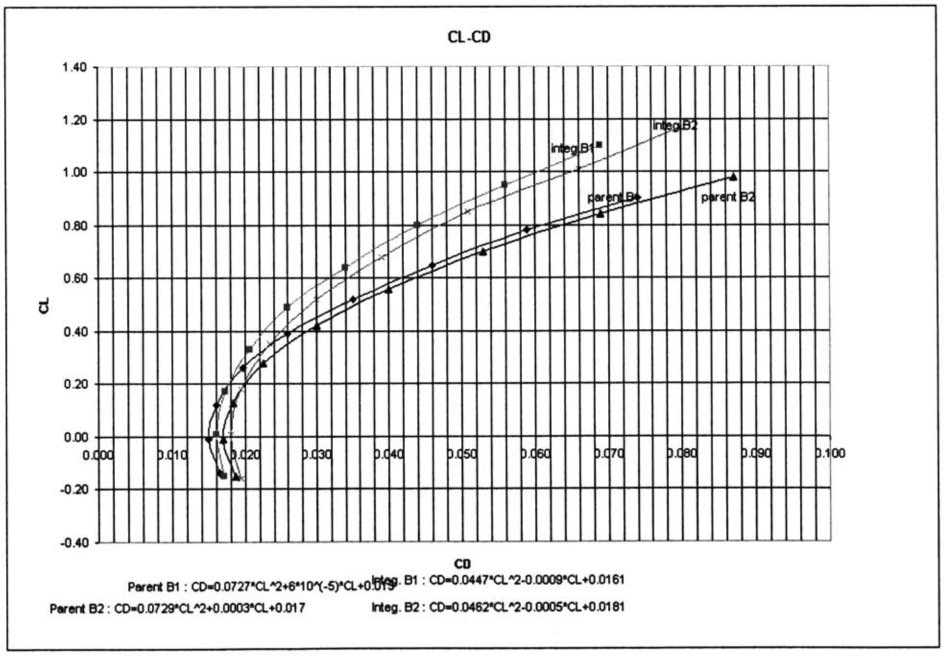

Figure A-2: $C_L - C_D$ of concepts B

Speed and Power required for level unaccelerated flight

Minteg	17.7	Sinteg	2.15	density	1	kg/m^3
Mparent	14.7	Sparent	1.90	propeller efficiency	0.7	

Parent B1

	V[m/s]	CL	CD	CL/CD	T[N]	HPrequired
	6	4.22	1.3078	3.2	44.7	0.51
	8	2.37	0.4241	5.6	25.8	0.40
	10	1.52	0.1826	8.3	17.3	0.33
	12	1.05	0.0958	11.0	13.1	0.30
	14	0.77	0.0587	13.2	10.9	0.29
	16	0.59	0.0406	14.6	9.9	0.30
	18	0.47	0.0310	15.1	9.5	0.33
	20	0.38	0.0255	14.9	9.7	0.37
	22	0.31	0.0222	14.1	10.2	0.43
	24	0.26	0.0201	13.1	11.0	0.50
	26	0.22	0.0187	12.0	12.0	0.60
	28	0.19	0.0177	10.9	13.2	0.71
	30	0.17	0.0171	9.9	14.6	0.84
	32	0.15	0.0166	8.9	16.2	0.99
	34	0.13	0.0163	8.1	17.9	1.16
opt. loiter	14.0	0.77	0.0587	13.2	10.9	**0.293**
opt. cruise	18.0	0.47	0.0310	15.12	9.5	0.33

Parent B2

	V[m/s]	CL	CD	CL/CD	T[N]	HPrequired
	6	4.22	1.3144	3.2	45.0	0.52
	8	2.37	0.4278	5.5	26.0	0.40
	10	1.52	0.1854	8.2	17.6	0.34
	12	1.05	0.0983	10.7	13.5	0.31
	14	0.77	0.0610	12.7	11.4	0.30
	16	0.59	0.0428	13.9	10.4	0.32
	18	0.47	0.0331	14.1	10.2	0.35
	20	0.38	0.0276	13.7	10.5	0.40
	22	0.31	0.0243	12.9	11.2	0.47
	24	0.26	0.0221	11.9	12.1	0.56
	26	0.22	0.0207	10.8	13.3	0.66
	28	0.19	0.0198	9.8	14.7	0.79
	30	0.17	0.0191	8.8	16.4	0.94
	32	0.15	0.0186	7.9	18.1	1.11
	34	0.13	0.0183	7.2	20.1	1.31
opt. loiter	13.5	0.83	0.0678	12.3	11.7	**0.304**
opt. cruise	18.0	0.47	0.0331	14.14	10.2	0.35

Integration B1

	V[m/s]	CL	CD	CL/CD	T[N]	HPrequired
	6	4.49	0.9119	4.9	35.3	0.41
	8	2.52	0.2985	8.5	20.5	0.31
	10	1.62	0.1313	12.3	14.1	0.27
	12	1.12	0.0713	15.7	11.0	0.25
	14	0.82	0.0457	18.0	9.6	0.26
	16	0.63	0.0333	18.9	9.2	0.28
	18	0.50	0.0268	18.6	9.3	0.32
	20	0.40	0.0230	17.5	9.9	0.38
	22	0.33	0.0208	16.1	10.8	0.46
	24	0.28	0.0194	14.5	12.0	0.55
	26	0.24	0.0184	13.0	13.4	0.67
	28	0.21	0.0178	11.6	15.0	0.80
	30	0.18	0.0174	10.3	16.8	0.97
	32	0.16	0.0171	9.2	18.8	1.15
	34	0.14	0.0168	8.3	20.9	1.36
opt. loiter	12.5	1.03	0.0629	16.4	10.6	0.2531
opt. cruise	16.5	0.59	0.0313	**18.95**	9.2	0.29

Integration B2

	V[m/s]	CL	CD	CL/CD	T[N]	HPrequired
	6	4.49	0.9459	4.7	36.6	0.42
	8	2.52	0.3111	8.1	21.4	0.33
	10	1.62	0.1378	11.7	14.8	0.28
	12	1.12	0.0757	14.8	11.7	0.27
	14	0.82	0.0491	16.8	10.3	0.28
	16	0.63	0.0362	17.4	10.0	0.31
	18	0.50	0.0293	17.0	10.2	0.35
	20	0.40	0.0254	15.9	10.9	0.42
	22	0.33	0.0231	14.5	12.0	0.51
	24	0.28	0.0216	13.0	13.4	0.61
	26	0.24	0.0206	11.6	15.0	0.75
	28	0.21	0.0200	10.3	16.8	0.90
	30	0.18	0.0195	9.2	18.9	1.08
	32	0.16	0.0192	8.2	21.1	1.29
	34	0.14	0.0189	7.4	23.5	1.53
opt. loiter	12.5	1.03	0.0670	15.4	11.2	0.2692
opt.cruise	16.0	0.63	0.0362	**17.44**	10.0	0.31

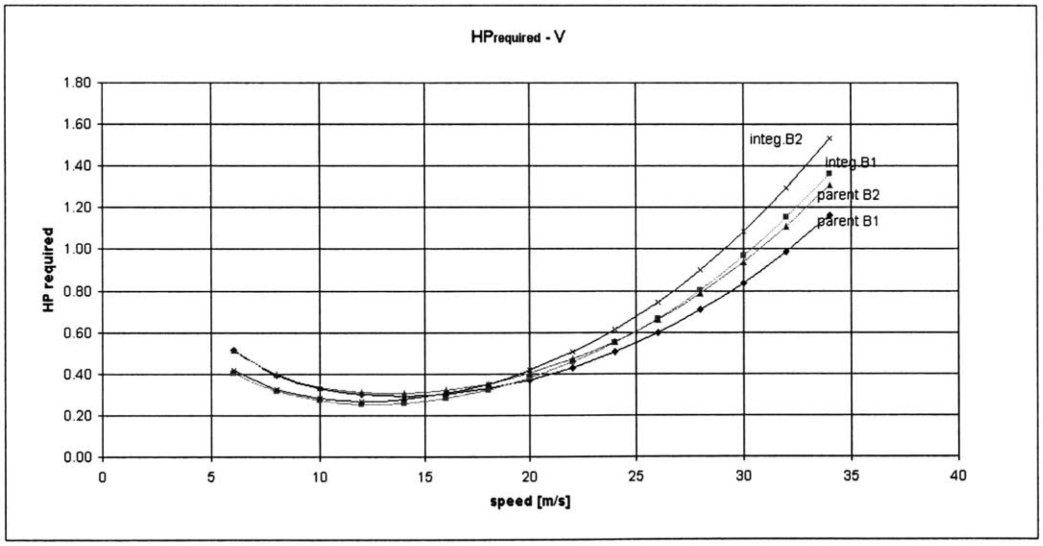

Figure A-3: speed - power relations

Forward Limit

requirements
1) elevator deflection should be less than 5 degree up to trim the aircraft
2) CL should be more than a certain value for the trimmed flight conditions

CLtrim

Parent B1 (NP=0.46)

		cg at			
		0.43	0.40	0.35	0.30
elevator deflection	0	0.36	0.20	0.11	0.08
	-5	0.64	0.36	0.21	0.14

Forward limit

CL>0.5	CL>0.3
0.42	0.385

Integration B1 (NP=0.54)

		cg at				
		0.53	0.52	0.51	0.50	0.49
elevator deflection	0	0.036	0.017	0.010	0.008	0.006
	-5	0.61	0.36	0.26	0.19	0.16

Forward limit

CL>0.5	CL>0.3
0.53	0.51

Parent B2 (NP=0.53)

		cg at				
		0.50	0.45	0.40	0.35	0.30
elevator deflection	0	0.31	0.13	0.08	0.06	0.05
	-5	1.10	0.53	0.34	0.25	0.20

Forward limit

CL>0.5	CL>0.3
0.45	0.38

Integration B2 (NP=0.59)

		cg at			
		0.55	0.50	0.45	0.40
elevator deflection	0	0.030	0.014	0.010	0.007
	-5	0.69	0.34	0.22	0.16

Forward limit

CL>0.5	CL>0.3
0.53	0.49

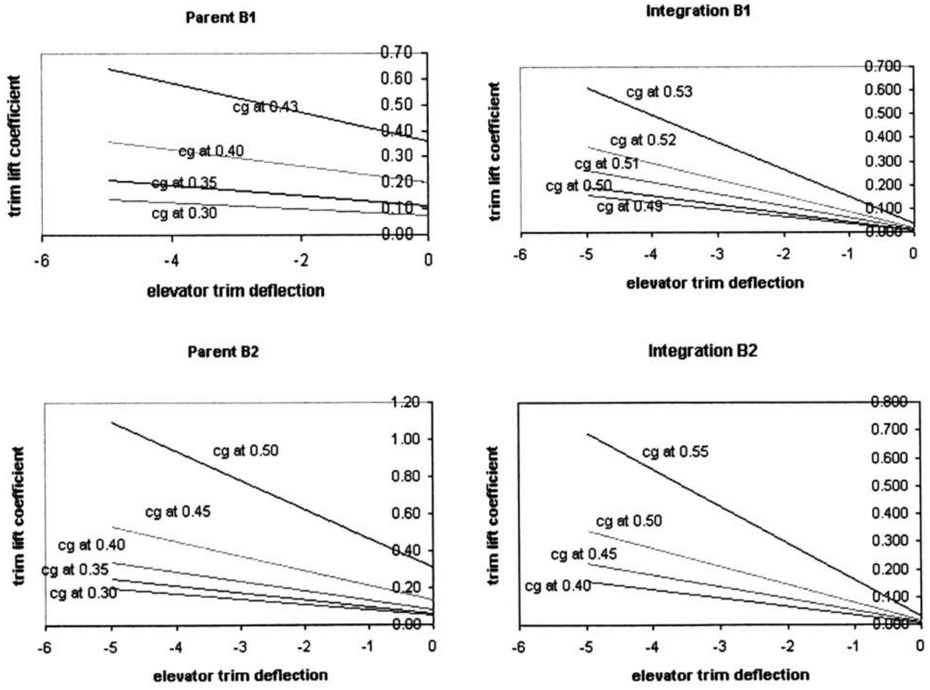

Figure A-4: Forward limit of c.g.

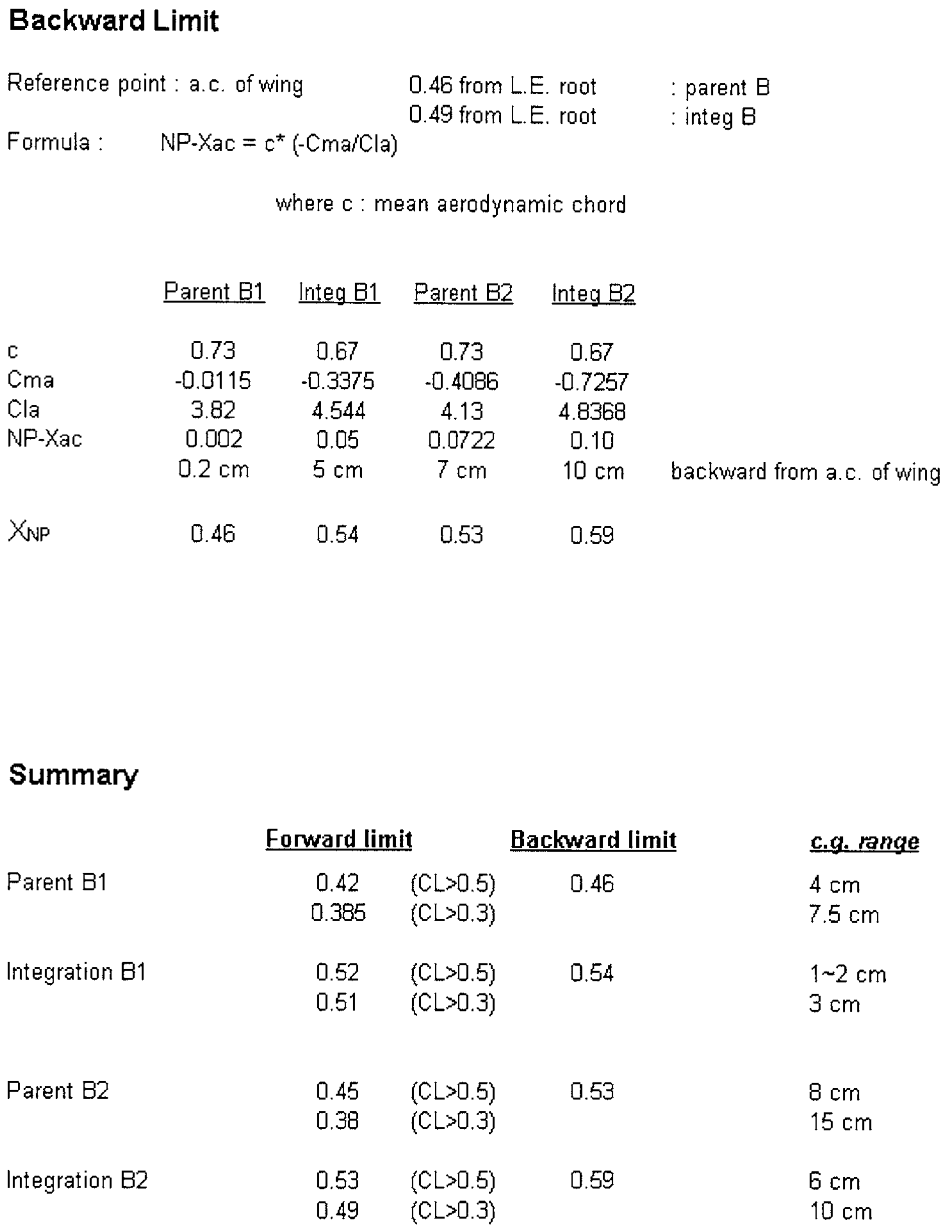

Backward Limit

Reference point : a.c. of wing 0.46 from L.E. root : parent B
0.49 from L.E. root : integ B

Formula : NP-Xac = c* (-Cma/Cla)

where c : mean aerodynamic chord

	Parent B1	Integ B1	Parent B2	Integ B2	
c	0.73	0.67	0.73	0.67	
Cma	-0.0115	-0.3375	-0.4086	-0.7257	
Cla	3.82	4.544	4.13	4.8368	
NP-Xac	0.002	0.05	0.0722	0.10	
	0.2 cm	5 cm	7 cm	10 cm	backward from a.c. of wing
X_{NP}	0.46	0.54	0.53	0.59	

Summary

	Forward limit		Backward limit	*c.g. range*
Parent B1	0.42	(CL>0.5)	0.46	4 cm
	0.385	(CL>0.3)		7.5 cm
Integration B1	0.52	(CL>0.5)	0.54	1~2 cm
	0.51	(CL>0.3)		3 cm
Parent B2	0.45	(CL>0.5)	0.53	8 cm
	0.38	(CL>0.3)		15 cm
Integration B2	0.53	(CL>0.5)	0.59	6 cm
	0.49	(CL>0.3)		10 cm

Figure A-5: Backward limit of c.g.

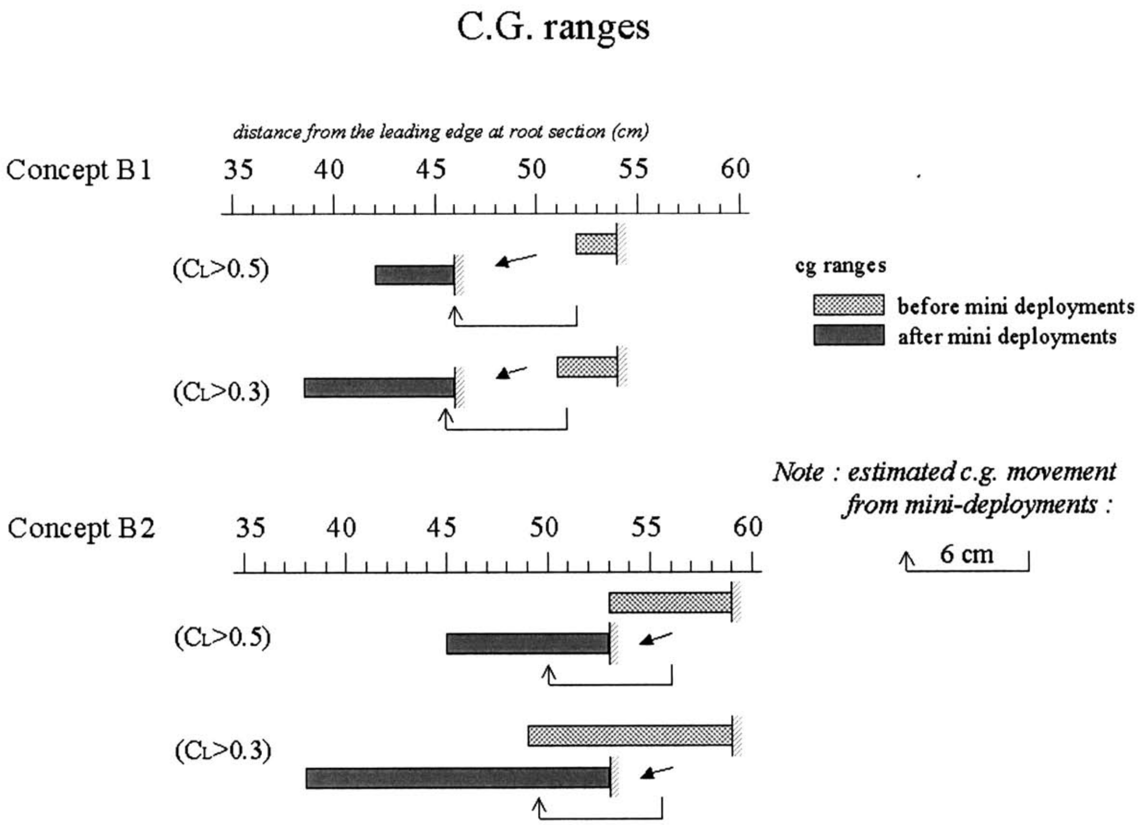

Figure A-6: c.g. ranges for concepts B1 and B2

Concept B1, B2

Weight

parent	14.7	[kg]
mini	1.5 (*2)	
integ.	17.7	

S

parent	1.9	[m^2]
mini	0.253	
integ.	2.15	

W/S

parent	7.63	[kg/m^2]	25 [oz/ft^2]
mini	5.93		19.4
integ.	8.14		26.7

AR

parent	4.1
mini	4.8
integ	7.1

b

parent	2.8	[m]
mini	1.1	
integ	3.9	

mean aerodynamic chord

parent	0.73	[m]
mini	0.25	
integ	0.67	

aerodynamic center of wing

parent	0.46
integ	0.49 from L.E. at root section

Optimal Loiter Condition

	V[m/s]	CL	CD	CL/CD	T[N]	HP required
parent B1	14.0	0.77	0.0587	13.2	10.9	0.293
parent B2	13.5	0.83	0.0678	12.3	11.7	0.304
integ. B1	12.5	1.03	0.0629	16.4	10.6	0.2531
integ. B2	12.5	1.03	0.0670	15.4	11.2	0.2692

Optimal Cruise Condition

	V[m/s]	CL	CD	CL/CD	T[N]	HP required
parent B1	18.0	0.47	0.0310	15.12	9.5	0.33
parent B2	18.0	0.47	0.0331	14.14	10.2	0.35
integ. B1	16.5	0.59	0.0313	18.95	9.2	0.29
integ. B2	16.0	0.63	0.0362	17.44	10.0	0.31

c.g. range

parent B1	4	[cm]	(CL>0.5)
	7.5		(CL>0.3)
parent B2	8		(CL>0.5)
	15		(CL>0.3)
integ. B1	1~2		(CL>0.5)
	3		(CL>0.3)
integ. B2	6		(CL>0.5)
	10		(CL>0.3)

Figure A-7: Summary of performance and stability properties for the integration concepts B1 and B2

Appendix B

Simulink Model

As was mentioned in Chapter 3, a nonlinear model of the mini vehicle for the reintegration phase 2 was constructed in Matlab simulink. This section includes some of the simulink blocks developed for the simulation. Figure B-1 shows the top level block diagram in the simulink model. The block 'mini' represents the dynamics of the mini vehicle from the inputs of the control surface deflections, power setting, and

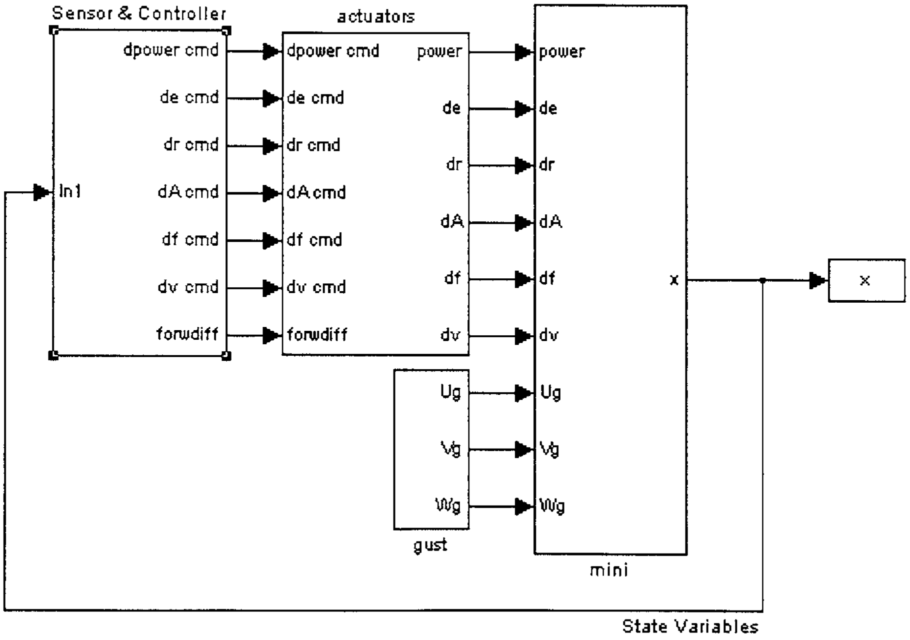

Figure B-1: Simulink model : top level

the gust velocity to the outputs of state variables. The block 'actuator' contains the actuator dynamics, where the servo motors are modeled based on the experiment in Section 3.4.4. Dryden gust model is produced from the block 'gust' which contains the shaping filters to generate the stochastic random gust. The 'sensor & controller' block includes the sensor model representing the vision based positioning sensor and the controllers described in Section 3.6. This block also contains some subblocks for subtracting reference or steady state values from the absolute values in order to apply the linear controllers.

The block diagram in Figure B-2 represent the subsystem block 'mini' in Figure B-1. In this subsystem, the blocks 'thrust' and 'aero' represent the Matlab m-funcions

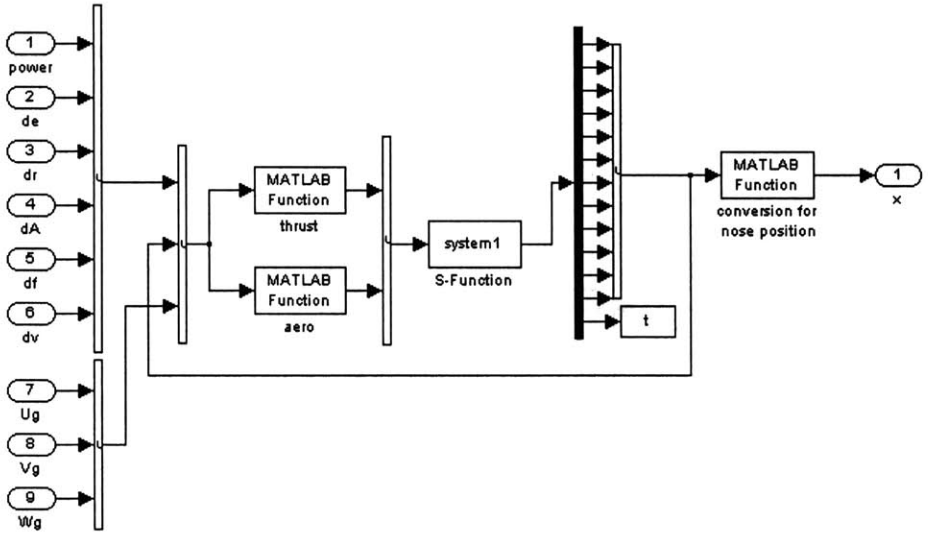

Figure B-2: Simulink model : vehicle dynamics

which generate thrust and aerodynamic forces and moments from the controller inputs and gust. These forces feed to the S-function block 'system1', which contains all the dynamic equations of motions described in Section 3.4.2. The outputs of this block are the state variables. The nose position is computed in the block 'conversion for nose position'.

Figure B-3 are the collection of the controllers which is a part of the 'sensor & controller' block in Figure B-1. It shows all the controllers as well as the combination

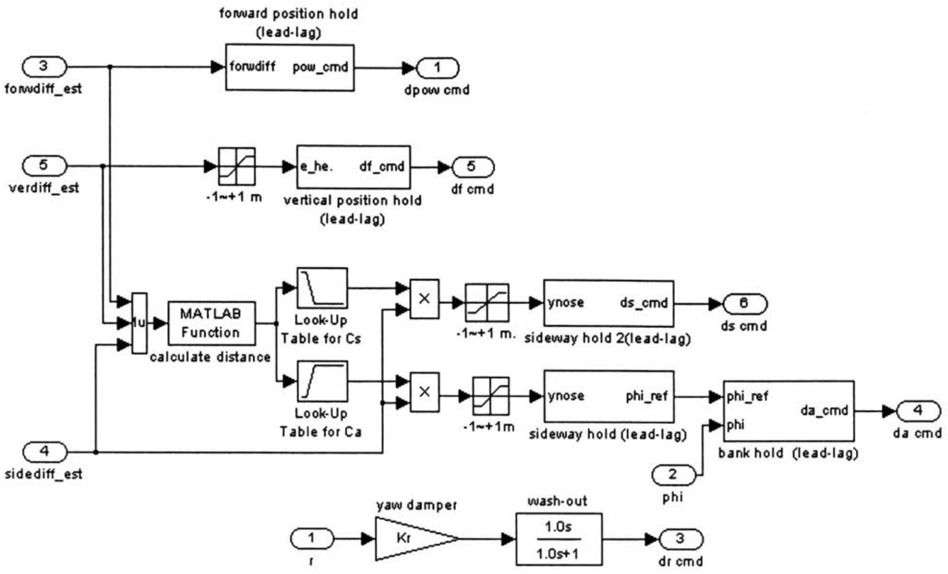

Figure B-3: Simulink model : controller

rule for the control surfaces described in Section 3.6. This whole block was converted to the discrete form and verified through the simulation using the C-MEX file provided as a part of Matlab S-function. This was mentioned in Section 3.7.

Bibliography

[1] Astrom and Wittenmark. *Computer Controlled Systems - Theroy and Design.* Prentice Hall.

[2] Frank L. Lewis Brian L. Stevens. *Aircraft Control and Simulation.* A Wiley-Interscience Publication.

[3] Video security. Leander, Texas.

[4] Dunstan Graham Duane McRuer, Irving Ashkenas. *Aircraft Dynamics and Automatic Control.* Princeton University Press, Princeton, New Jersey.

[5] Jr. John D. Anderson. *Fundamentals of Aerodynamics, 2nd ed.* McGraw-Hill, Maryland.

[6] Daniel P. Raymer. *Aircraft Design: A Conceptual Approach.* AIAA Education Series, Washington, D.C, 1989.

[7] Jan Roskam. *Airplane Flight Dynamics and Automatic Flight Controls.* Roskam Aviation and Engineering Corporation, Kansas, 1979.

[8] Uiuc applied aerodynamics group, webpage, /amber.aae.uiuc.edu/ m-selig/ads.html.

[9] Francois Urbain. Vehicle design, flight control avionics design, and flight test for the parent child unmanned aerial vehicle, June 2001.